Electronic State Excitations in the Water Molecule by Collisions with Low Energy Electrons

A Thesis
Presented for the Degree of
Doctor of Philosophy

by

Penny Anne Thorn BSc. (Hons.)

at

Flinders University of South Australia
Faculty of Science and Engineering
School of Chemistry Physics and Earth Sciences

14th July 2008

Contents

Summary

This thesis reports on a series of electron scattering experiments with H_2O, made with a high resolution crossed beam spectrometer. From the results of those experiments absolute cross sections for the electronic state excitations were ultimately determined. In many cases the present work represents the first time such cross sections have been measured.

What motivated us to measure these cross sections is outlined in Chapter 1. This chapter also contains a discussion of relevant theoretical works, as well as some previous experimental investigations which were important precursors to the present study.

Chapter 2 presents a detailed description of the many previous studies on the spectroscopy of H_2O. This was a crucial part of this thesis, as the spectroscopy of H_2O underpins the interpretation of the complicated electronic structure found in the measured energy loss spectra.

In Chapter 3 we discuss the experimental apparatus and our measurement techniques and calibration procedures, including some alterations that were made during the course of the present experiments. The spectral deconvolution procedure for determining the differential cross sections and the molecular phase shift analysis technique for deriving the integral cross sections, are also described in this chapter.

Our experimentally determined cross sections are presented and discussed in Chapter 4 for the first six excited electronic states, with this discussion largely being framed in terms of a comparison to the currently available theoretical data. The cross sections for the remaining states, which could not be compared to theory, are presented in the appendices A and B.

Chapter 5 discusses the use of the present cross sections in order to calculate some parameters useful in atmospheric modelling. Finally the major findings of the present study are highlighted in Chapter 6, where recommendations are also made for future work.

Declaration

I certify that this thesis does not incorporate without acknowledgment any material previously submitted for a degree or diploma in any university; and that to the best of my knowledge and belief it does not contain any material previously published or written by another person except where due reference is made in the text.

.....

Penny A. Thorn

Acknowledgements

Firstly I would like to thank my parents, because they were the first to offer me their support and have never ceased providing it. I would also like to thank my parents, sister and grandparents for being a source of encouragement and inspiration for longer than I can remember.

The guidance of my supervisor Associate Professor Michael Brunger, throughout this project, has been invaluable. I would like to thank him for his support and encouragement and for sharing his expertise. Dr Laurence Campbell's advice and expertise were also important to the success of this project, and along with the wise counsel of Emeritus Professor Peter Teubner were greatly appreciated.

I would like to acknowledge the research group of Professor Hiroshi Tanaka at Sophia University in Japan, for the measurements they made to cross check with ours. I would also like to acknowledge Dr. Tom Rescigno and Dr. Yong-Ki Kim (deceased) for their helpful comments in regard to the theoretical calculations.

The assistance of the talented staff of the Electronics and Engineering Workshops was much appreciated. I am grateful to them for all their help maintaining the apparatus and with a variety of technical problems that I encountered along the way.

Thank you to my fellow postgraduate students for helping to make the working environment at Flinders happy and productive. For helping me to remember the other important thing in life, like how to have fun, I also have to thank all my friends.

Finally I would like to thank the Ferry Trust and the ARC Centre of Excellence for Antimatter and Matter Studies, who provided me with a scholarship. Thanks also to Flinders University for the award of a Research Student Conference Travel Grant.

Chapter 1

Introduction

The Infrared Space Observatory (ISO) of the European Space Agency (ESA) has confirmed the existence of water vapour in several galaxies including our own, and water-ice in several more. The ISO has also confirmed water-ice and vapour exists in comets [1]. Due to measurements from the ISO, the precipitable water on Mars has been determined to be 15μm, while water was also discovered in the atmospheres of the giant planets; Jupiter, Saturn, Uranus and Neptune, as well as on Titan (Saturn's largest moon) [1]. Indeed water is the 3rd most plentiful molecule in the universe [2,3], and is even present in the atmosphere of our Sun [2]. The discovery of water in so many different places is of great scientific and human interest, at least in part because water is fundamental to life on Earth.

Without water, life on Earth as we know it would not be possible. Water is an important component of the biological cell, and hence an essential part of plant and animal tissue, making up about 70% of the total mass of mammals [3]. In the Earth's atmosphere water is a very important greenhouse gas owing to it's strong absorption in the infrared (IR) spectral region, so that it absorbs significant radiation emanating from the planet's surface thereby reducing heat loss to space. As such H_2O contributes $\approx$65% to the total 33K of natural warming [4], without which Earth would be uninhabitable. The surface of the Earth is made up of more than 70% water, with its oceans being responsible for a large amount of the

latitudinal distribution of heat around the Earth. This effect thus helps to create a larger inhabitable area on our planet.

Accurate cross sections for the different possible outcomes of an electron - water molecule collision, are important in improving our understanding of processes that occur wherever free electrons and water coexist. Since water is so common these scenarios of coexistence are numerous, occurring in the fields of space science, plasma physics, biophysics and in atmospheric science. For example, cross sections for electron scattering from both liquid and vaporous water are fundamental to an understanding and hence further development of plasma electrosurgical devices [3]. In addition calculations in the field of industrial plasma physics, by Tas *et al* [5], for the removal of NO_x species from a flue gas by plasma processes, required cross sections for all components of the flue gas including water vapour. The importance of accurate cross sections for electron-water collisions in modelling the effects of radiation on biological tissue (by the calculation of electron tracks) is also well known, having been summarized by Uehara *et al* [6] and Muñoz *et al* [7].

The current state of scattering theory is such that the level of agreement between calculated and measured cross sections, is quite good for many electron-atom scattering processes. As discussed by Bray *et al* [8] the convergent close-coupling (CCC) method gives very good results, when compared with available experiments, for electron scattering from both atomic hydrogen and helium atoms, as well as the alkali atoms and alkaline-earth atoms. In a more recent review Buckman and Sullivan [9] considered the general accord between theory and experiment in cross sections for electron (and also positron) scattering from atoms and molecules. They also noted that results for calculations of electron-atom scattering for many processes are quite good. Furthermore they concluded this was also the case for some light molecular species e.g. N_2. However they also highlighted the significant discrepancies that exist between theory and experiment for many polyatomic systems.

The water molecule is one target for which reliable cross sections have yet to be determined for many scattering processes. In fact as we shall see later, for some processes there is a total lack of experimental data with which to compare to the calculated values. This lack of data and an inconsistency between theory and experiment where the data does exist, is not entirely surprising since water does present some significant challenges to both theorists and experimentalists. Water's strong dipole moment of 1.8546±0.0004 D, as measured by Dyke and Muenter [10], can create major difficulties for theorists. Water can also be a problematic substance in a vacuum system and can be potentially harmful to components of an apparatus inside a vacuum chamber, due to its tendency to stick to and condense on surfaces.

The state of our knowledge on cross sections for electron collisions with H_2O was reviewed by Karwasz *et al* [11] in 2001, and more recently by Itikawa and Mason [12] in 2005. One of the objectives of Itikawa and Mason was to try and determine a set of recommended values for the cross sections, for every major electron collision process in H_2O. In attempting this, the shortcomings in the present state of knowledge for electron impact cross sections in the water molecule were clearly highlighted. Nonetheless Itikawa and Mason did produce a recommended set of cross sections for total scattering, elastic scattering, momentum transfer, rotational excitation, vibrational excitation, attachment, ionisation, some neutral dissociation channels and some radiative emission cross sections. There was, however, no data set recommended for electronic state excitations in H_2O, essentially because there were no experimentally determined absolute cross sections available for those excitations. In addition, there was little consistency in the electronic-state results from the few theoretical studies so that no data could be assembled from that work.

The present study was therefore largely concerned with measuring accurate absolute values for the electronic state excitation cross sections in H_2O, in the incident electron energy range 15eV to 50eV. It is hoped that these data will eventually help to improve the current state of electron - molecule scattering theory,

as well as being useful in the fields of modelling discussed earlier where these cross sections are important input parameters. Further, as an illustration of this latter point, the cross sections determined here were used to calculate some quantities of importance in atmospheric modelling, with the eventual aim being to include these parameters in a statistical equilibrium model of Earth's ionosphere. Note that the statistical equilibrium approach was initially developed by Cartwright *et al* [13], and was implemented previously to predict the absolute population density of vibrationally excited N_2 (Campbell *et al* [14]), O_2 (Jones *et al* [15]) and NO (Cartwright *et al* [13]) over a range of altitudes. H_2O will also ultimately be included in our ionospheric model in order to calculate population densities for its dissociative excited states. The aim of that work is to improve our understanding for the role of electron-driven processes in the production of vibrationally excited OH in our atmosphere. It is known that vibrationally excited OH molecules produce the Meinel bands upon de-excitation, (Meinel [16], [17]), but the source of this vibrationally excited OH could be chemical, or electron driven, or a mixture of both. As an initial step in achieving this aim, the present thesis reports electron energy transfer rates and electron impact excitation rates calculated with the integral cross sections determined in this study. This is detailed in Chapter 5.

There have been several previous studies into electron collision induced electronic excitations in H_2O. No previous experimental study, however, has published absolute cross sections for these processes, although many experimental and theoretical studies have managed to elucidate the excited state spectroscopy of H_2O. Some of the foremost spectroscopic studies include Trajmar *et al* [18], Goddard and Hunt [19], Chutjian *et al* [20], Jureta [21] and Mota *et al* [22]. These spectroscopic studies, along with the multitude of other electron impact, photoabsorption and theoretical works, were a necessary precursor to the present study; enabling the accurate and reliable interpretation of the measured energy loss spectra. Full details and evaluations of all that work are provided in Chapter 2.

Another essential precursor to the present work was the availability of accurate elastic differential cross sections (DCSs), as they are used to put the DCSs

measured in the present study on an absolute scale. This procedure is detailed in Chapter 3. Fortunately there have been quite a few studies into elastic scattering cross sections at the energies of interest to us, with the most recent experimental study being that by Cho *et al* [23] in 2004. Cho *et al* used a crossed beam spectrometer with a magnetic angle changing (MAC) device, to measure elastic DCSs for scattering angles from 10° to 180° and incident electron energies from 4eV to 50eV, with an uncertainty of typically ≈10%. One of the most recent calculations was that from Faure *et al* [24], also in 2004, who used the R-matrix method to calculate corresponding DCSs for incident electron energies up to 7eV. While this was not the energy range of interest to us, the comparison of the DCSs from Faure *et al* with those from Cho *et al* at 4eV is very good. This is particularly encouraging as previous theory at 4eV incident electron energy, being that from Varella *et al* [25], did not have a good shape agreement with any of the experimental data (including Cho *et al*). In fact the elastic DCSs calculated by Varella *et al* seemed to give some spurious structure in the angular distribution for incident electron energies of 10eV and below, while those from Okamoto *et al* [26] deviated somewhat from the experimental results at incident electron energies below about 6eV. In the energy and angular range of interest to this study the elastic cross sections of Cho *et al* [23], Shyn and Cho [27], Johnstone and Newell [28], Danjo and Nishimura [29], Okamoto *et al* [26] and Varella *et al* [25] are generally in good agreement. The results from Cho *et al*, Johnstone and Newell and Okamoto *et al* are in particularly good accord, although it still can not be said that all their results are within each others experimental uncertainty. The cross sections of Cho *et al* were chosen to normalise our data, largely because of their low uncertainty and because in many cases they represent an approximate mean of the other elastic DCS data sets. We note that this choice is largely in accord with some recent reviews of cross section data bases [30].

Several theoretical calculations for differential and integral cross sections exist in the literature for some of the lower lying electronic excitations. In particular the $\tilde{b}^3\mathrm{A}_1$ state, with an excitation energy ≈9.46eV, has received the most attention.

Here we note the integral cross section (ICS) calculations by Pritchard *et al* [31], Gil *et al* [32], Lee *et al* [33], Morgan [34] and Gorfinkiel *et al* [35]. A comparison of the results from these studies shows considerable disparity, in both magnitude and shape, between the various theories. This observation can also be generalised to the other common electronic states they considered. The extent of this disparity is somewhat surprising, as there are some significant similarities between some of these different theoretical approaches. For example four of these calculations, namely Pritchard *et al*, Gil *et al*, Lee *et al* and Morgan, were carried out in the fixed nuclei (FN) approximation at the equilibrium geometry, while Gorfinkiel *et al* used the adiabatic nuclei (AN) approximation. Pritchard *et al* and Lee *et al* also both carried out two state calculations, with Pritchard *et al* using the Schwinger multichannel method and Lee *et al* the distorted-wave approximation. Gil *et al* employed five target states within the complex Kohn variational method and like Pritchard *et al* and Lee *et al* calculated both ICS and DCS values. Finally, we note that both Morgan and Gorfinkiel *et al* made seven state R-matrix calculations of the ICSs for the $\tilde{b}^3\mathrm{A}_1$ state. All these computations are discussed in detail in Chapter 4.

Gil *et al* [32], Morgan [34] and Gorfinkiel *et al* [35] also calculated cross sections for the $\tilde{a}^3\mathrm{B}_1$, $\tilde{A}^1\mathrm{B}_1$ and $\tilde{B}^1\mathrm{A}_1$ states. In addition, Lee *et al* [33] computed cross sections for a second state with $^3\mathrm{A}_1$ symmetry, but with a higher excitation energy. Gil *et al* found their DCSs for the singlet transitions ($\tilde{A}^1\mathrm{B}_1$ and $\tilde{B}^1\mathrm{A}_1$) to be strongly forward peaked, but the triplet states were not so. Both Morgan and Gil *et al* found resonances in all their integral cross sections, while Gorfinkiel *et al* [35] calculated structureless cross sections with their AN method. These apparently conflicting results suggest that either the FN resonances are simply an artefact of the calculation and therefore not physical, or that the AN approach does not effectively treat for resonances.

The most recent calculation was performed by Kim [36], who computed ICSs for the $\tilde{A}^1\mathrm{B}_1$ state, with a scaled Born method, at incident electron energies from its threshold to 1000eV. This method involves applying a scaling factor (an accu-

rate value for the optical oscillator strength) to the plane wave Born cross section in order to improve the accuracy of the Born cross section. This is particularly important at lower incident electron energies and this approach has been successful in other systems, but it is unfortunately only applicable to the calculation of cross sections for dipole - allowed transitions. We note that the calculation for H_2O represents the first time this technique has been used for a triatomic molecule. The $\tilde{A}^1B_1$ state ICSs from this theory were considerably smaller than most of the previously discussed theories. Indeed it is approximately 50% smaller than the unscaled Born cross section, which is of a similar magnitude to that from Gorfinkiel *et al* [35]. The scaled Born cross section from Kim is relatively featureless, with a maximum at approximately 30eV incident electron energy. Full details can again be found in Chapter 4.

Despite the paucity of data pertaining to cross sections for electronic state excitation in H_2O by electron collisions, cross sections for many other electron collision processes in H_2O have been somewhat more thoroughly studied. Some of the cross sections for these other processes can be indirectly compared to our measured cross sections, and thus provide a useful self - consistency test for our work. For example grand total cross sections (GTSs) for electron-water scattering should be equal to the sum of the integral cross sections for all the possible electron collision processes. These grand total scattering cross sections have been measured by several experimentalists, including Szmytkowski [37] and a recommended data set was compiled for them by Itikawa and Mason [12]. We were hence able to compare to these GTSs, a summation of the ICSs for all the electron collision processes for which we have values including the present measured electronic excitation integral cross sections. We can also compare the cross sections from Harb *et al* [38], who measured absolute cross sections for the production of ground state OH by electron impact on H_2O for incident electron energies from threshold to 300eV, to a subset of the present cross sections for water's dissociatively excited states. A further self-consistency check for the present ICSs is provided by the cross sections calculated by Muñoz *et al* [7]. These cross sections [7] are for in-

elastic processes (ionisation plus electronic state excitation) for incident electron energies from 7.5eV to 10keV. The results from all these self - consistency checks are also presented in Chapter 4.

Chapter 2

Spectroscopy of Water

Water is a molecule of the C_{2v} point group, having 2 planes of symmetry and one rotational axis of symmetry [39]. The ground electronic state has $^1A_1$ symmetry and an electronic configuration [19]:

$$(1a_1)^2(2a_1)^2(1b_2)^2(3a_1)^2(1b_1)^2$$

The first ionisation energy of H_2O is 12.61eV [40]. This thesis pertains to excitations below this ionisation energy, actually the limit of our energy loss spectra was ≈12eV. Excited states in this region of the energy loss spectrum occur from excitations out of only the $3a_1$ and $1b_1$ orbitals.

The electronic state spectroscopy of H_2O is very complicated. Nonetheless for our spectral deconvolution procedure, detailed later in Section 3.2, it is necessary to know both the position and width of each feature. As a consequence, we studied in minute detail the previous spectroscopic work in order to try and determine these values. We have considered calculations and experiments where both photons and electrons have been employed as target probes. A summary of these previous spectroscopic studies as well as where we have needed to make our own assignments to features in our spectra, can be found in Tables 2.1 and 2.2. Table 2.1 specifically lists the results from the theoretical studies, with a column of our assignments and energies provided for comparison. Table 2.2 lists corresponding results from both photoabsorption and electron impact experiments,

State			Excitation Energy (eV)										
			Claydon[41]	Goddard[19]	Winter[42]		Kaldor[43]	Warken[44]	Christiansen[45] and Larsen[46]		Cai[47]	Trofimov[48]	Present
					CI	Best			FCI	CC3			
$1b_1 \rightarrow 3sa_1(4a_1)$	$\tilde{a}$	$^3B_1$	6.20	6.68	7.26	7.14	7.16		7.06	7.04	7.23	7.15	7.14
	$\tilde{A}$	$^1B_1$	7.43	7.30	7.61	7.49	7.54	7.34	7.44	7.42	7.61		7.49
$1b_1 \rightarrow 3pb_2(2b_2)$		$^3A_2$	7.49	8.68	9.34	9.10	9.28		9.04	9.02	9.15	9.18	8.90
		$^1A_2$	8.03	9.04	9.46	9.20	9.46	9.28	9.20	9.18	9.36	9.38	9.20
$3a_1 \rightarrow 3sa_1(4a_1)$	$\tilde{b}$	$^3A_1$	8.67	9.02	9.44	9.35	9.48		9.44	9.43	9.30	9.54	9.45
	$\tilde{B}$	$^1A_1$	10.85	9.92	9.82	9.73	9.80	9.81	9.87	9.85	9.76	10.01	9.73
$1b_1 \rightarrow 3pb_1$	$\tilde{d}$	$^3A_1$		9.70	9.74	9.81	9.86		10.83	10.82	9.76	10.84	9.79
$1b_1 \rightarrow 3pa_1$	$\tilde{c}$	$^3B_1$		9.96	9.99	9.93	10.12				9.89		9.93
	$\tilde{C}$	$^1B_1$		10.04	10.06	10.00	10.17	10.02			10.00		9.98
$1b_1 \rightarrow 3pb_1$	$\tilde{D}$	$^1A_1$		10.16	10.16	10.17	10.33	10.10			10.23		10.14
$1b_1 \rightarrow 3pa_1$		$^1B_1(100)$											10.35
$1b_1 \rightarrow 4sa_1$		$^3B_1$		10.51								11.16	10.35
		$^1B_1$		10.64							10.65		10.55
$1b_1 \rightarrow 3pb_1$		$^1A_1(100)$											10.55
$1b_1 \rightarrow 3db_2$		$^3A_2$		10.79									10.70
$1b_1 \rightarrow 3pb_1$		$^1A_1(110)$											10.77
$1b_1 \rightarrow 3pa_1$		$^1B_1(200)$											10.77
$1b_1 \rightarrow 3db_2$		$^1A_2$		10.87							10.85		10.84
$1b_1 \rightarrow 3pb_1$		$^1A_1(200)$											10.97
$1b_1 \rightarrow 3da_1$	$\tilde{e}$	$^3B_1$		11.05									10.97
	$\tilde{E}$	$^1B_1$		11.07									10.97
$3a_1 \rightarrow 3pb_2(2b_2)$		$^3B_2$	9.43	10.81	11.11	11.10			11.05	11.04	11.29	11.45	11.10
$1b_1 \rightarrow 3da_2$		$^3B_2$											11.10
		$^1B_2$											11.10

Table 2.1: Summary of the available results from the theoretical spectroscopic studies. The spectral assignments from the present study are included in the final column for the purpose of comparison.

State		Excitation Energy (eV)										
		Claydon[41]	Goddard[19]	Winter[42]		Kaldor[43]	Warken[44]	Christiansen[45] and Larsen[46]		Cai[47]	Trofimov[48]	Present
				CI	Best			FCI	CC3			
$1b_1 \rightarrow 3db_1$	$^3A_1$		11.16									11.23
	$^1A_1$		11.17									11.23
$1b_1 \rightarrow 3da_1$	$^3B_1$		11.16									11.23
	$^1B_1$		11.17									11.23
$1b_1 \rightarrow 4pb_2$	$^3A_2$		11.18									11.23
	$^1A_2$		11.21									11.23
$1b_1 \rightarrow 3sa_1$	$^3B_2$											11.50
	$^1B_2$											11.50
$1b_1 \rightarrow 4pa_1$	$^3B_1$		11.40									11.35
	$^1B_1$		11.42									11.35
$1b_1 \rightarrow 4pb_1$	$^3A_1$		11.32									11.35
	$^1A_1$		11.48									11.35
$3a_1 \rightarrow 3pb_2(2b_2)$	$^1B_2$	11.06	11.46	11.47	11.50		11.56	11.60	11.58	11.54	11.79	11.50
$1b_1 \rightarrow 5sa_1$	$^3B_1$		11.62									11.50
	$^1B_1$		11.66									11.50
$1b_1 \rightarrow 4db_2$	$^3A_2$		11.64									11.645
	$^1A_2$		11.67									11.645
$1b_1 \rightarrow 4da_1$	$^3B_1$											11.68
	$^1B_1$											11.75
$1b_1 \rightarrow 4db_1$	$^1A_1$											11.80
$3a_1 \rightarrow 3pa_1$	$^3A_1$			11.77	11.80							11.80
$3a_1 \rightarrow 3pb_1$	$^3B_1$			11.87	11.86			11.32	11.30			11.87
$1b_1 \rightarrow 5pa_1$	$^1B_1$											11.90
$3a_1 \rightarrow 3pb_1$	$^1B_1$			11.92	11.91							11.90
$1b_1 \rightarrow 5pb_1$	$^1A_1$											11.90
$3a_1 \rightarrow 3pa_1$	$^1A_1$			12.08	12.10							12.06

Table 2.1 continued

State			Excitation Energy (eV)									
			Skerbele[49]	Knoop[50]	Trajmar[18]	Chutjian[20]	Chan[51]	Herzberg[39]	Mota[22]	Gurtler[52]	Jureta[21]	Present
$1b_1 \rightarrow 3sa_1(4a_1)$	$\tilde{a}$	$^3B_1$		7.20		7.00					9.20	7.14
	$\tilde{A}$	$^1B_1$	7.42		7.40	7.40	7.4	6.67 - 8.55	7.464	7.44		7.49
$1b_1 \rightarrow 3pb_2(2b_2)$		$^3A_2$		9.1 (triplet		8.90					9.02	8.90
		$^1A_2$		or singlet)		9.10						9.20
$3a_1 \rightarrow 3sa_1(4a_1)$	$\tilde{b}$	$^3A_1$		9.70 (triplet		9.30						9.45
	$\tilde{B}$	$^1A_1$	9.67	or singlet)	9.70	9.70	9.7	8.79 - 9.87	9.991	9.85		9.73
$1b_1 \rightarrow 3pb_1$	$\tilde{d}$	$^3A_1$			9.81[e]	9.81					9.82	9.79
$1b_1 \rightarrow 3pa_1$	$\tilde{c}$	$^3B_1$		10.0 (triplet		9.98	9.994				10.00	9.93
	$\tilde{C}$	$^1B_1$	10.00	or singlet)	10.00	10.01		9.99 - 10.38	10.011	9.998		9.98
$1b_1 \rightarrow 3pb_1$	$\tilde{D}$	$^1A_1$	10.17		10.17	10.16	10.171	10.17 - 10.58	10.163	10.171		10.14
$1b_1 \rightarrow 3pa_1$		$^1B_1(100)$	10.38		10.38	10.39	10.388		10.401			10.35
$1b_1 \rightarrow 4sa_1$		$^3B_1$				10.39						10.35
		$^1B_1$			11.01	10.52		10.99	10.624	10.64		10.55
$1b_1 \rightarrow 3pb_1$		$^1A_1(100)$	10.57		10.57	10.55	10.575		10.574			10.55
$1b_1 \rightarrow 3db_2$		$^3A_2$				10.68						10.70
$1b_1 \rightarrow 3pb_1$		$^1A_1(110)$			10.76	10.77	10.780		10.777			10.77
$1b_1 \rightarrow 3pa_1$		$^1B_1(200)$	10.76		10.76	10.77	10.765					10.77
$1b_1 \rightarrow 3db_2$		$^1A_2$				10.84						10.84
$1b_1 \rightarrow 3pb_1$		$^1A_1(200)$				10.97						10.97
$1b_1 \rightarrow 3da_1$	$\tilde{e}$	$^3B_1$				[t]11.01					11.05	10.97
	$\tilde{E}$	$^1B_1$	11.01			11.01	10.990			10.990		10.97
$3a_1 \rightarrow 3pb_2(2b_2)$		$^3B_2$			11.11[e]	[t]11.11						11.10
$1b_1 \rightarrow 3da_2$		$^3B_2$				[t]11.10						11.10
		$^1B_2$				[t]11.10	11.041					11.10

Table 2.2: Summary of the available results from the experimental spectroscopic studies. The spectral assignments from the present study are again included in the final column for the purpose of comparison. [e] indicates that Trajmar *et al* [18] found a feature at this energy but did not assign a transition to it. That was done in either a later publication or in the present investigation. [t] indicates that in Chutjian *et al*'s spectra this feature was significantly overlapped, or that the quoted value is a repetition of a calculated value [20].

State		Excitation Energy (eV)									
		Skerbele[49]	Knoop[50]	Trajmar[18]	Chutjian[20]	Chan[51]	Herzberg[39]	Mota[22]	Gurtler[52]	Jureta[21]	Present
$1b_1 \rightarrow 3db_1$	$^3A_1$				^{t}11.13					11.15	11.23
	$^1A_1$	11.11			11.13	11.057		11.057			11.23
$1b_1 \rightarrow 3da_1$	$^3B_1$				^{t}11.16						11.23
	$^1B_1$				^{t}11.17	11.122	11.12				11.23
$1b_1 \rightarrow 4pb_2$	$^3A_2$				^{t}11.18						11.23
	$^1A_2$	11.37			^{t}11.21						11.23
$1b_1 \rightarrow 3sa_1$	$^3B_2$				^{t}11.30						11.50
	$^1B_2$	11.49			^{t}11.33						11.50
$1b_1 \rightarrow 4pa_1$	$^3B_1$				^{t}11.33					11.32	11.35
	$^1B_1$				11.35				11.374		11.35
$1b_1 \rightarrow 4pb_1$	$^3A_1$				^{t}11.19						11.35
	$^1A_1$				11.40				11.432		11.35
$3a_1 \rightarrow 3pb_2(2b_2)$	$^1B_2$				^{t}11.46						11.50
$1b_1 \rightarrow 5sa_1$	$^3B_1$				^{t}11.45						11.50
	$^1B_1$				11.53						11.50
$1b_1 \rightarrow 4db_2$	$^3A_2$				^{t}11.64					11.32	11.645
	$^1A_2$				^{t}11.67						11.645
$1b_1 \rightarrow 4da_1$	$^3B_1$				^{t}11.68						11.68
	$^1B_1$	11.75			11.74					11.729	11.75
$1b_1 \rightarrow 4db_1$	$^1A_1$				11.78				11.770		11.80
$3a_1 \rightarrow 3pa_1$	$^3A_1$				^{t}11.77						11.80
$3a_1 \rightarrow 3pb_1$	$^3B_1$										11.87
$1b_1 \rightarrow 5pa_1$	$^1B_1$				11.89				11.890		11.90
$3a_1 \rightarrow 3pb_1$	$^1B_1$				^{t}11.92						11.90
$1b_1 \rightarrow 5pb_1$	$^1A_1$				11.91						11.90
$3a_1 \rightarrow 3pa_1$	$^1A_1$	12.07			^{t}12.08						12.06

Table 2.2 continued.

and again includes a column of our assignments and energies for comparison. In the text that follows we discuss these previous spectroscopic studies and also why we chose the spectral assignments and energies we did. In general, however, our assignments were largely derived from the previous electron and photon scattering experiments in preference over the calculations.

There has been a relatively modest number of electron impact studies into the spectroscopy of water. A selection of the results from these studies, including those from Skerbele *et al* [49], Knoop *et al* [50], Trajmar *et al* [18], Chutjian *et al* [20], and Jureta [21], are given in table 2.2. Skerbele, Lassettre and colleagues actually published many papers on the electron impact spectroscopy of water between 1964 and 1968 including references [53], [54], [49], [55] and [56]. These studies used several different apparatus with different energy and angular ranges and resolution. They all, however, like those of Knoop *et al* [50] and Trajmar*et al* [18], involved passing the electron beam through a collision chamber filled with the target H_2O vapour. This configuration is different to the crossed beam work reported in this thesis. We have chosen to include only results from their reference [49] in table 2.2, and in our discussion that follows. This is because the work in reference [49] was the most recent in their series of papers to cover the energy range of interest to us, and it was conducted with a higher energy resolution than some of their other studies. Note that the post scattering electron energy analysis system used by Skerbele *et al* [49] was an electrostatic parallel plate velocity selector. The study by Knoop *et al* [50] used a variation of the Trapped Electron (TE) method, called the Double Retarding Potential Difference Method (DRPD), which applies some energy analysis to the incident electrons as well as the scattered electrons. On the other hand the apparatus employed by Trajmar *et al* [18], like the present apparatus, used electrostatic hemispherical monochromators to form the incident electron beam and in the energy analysis of the scattered electrons. The apparatus of Chutjian*et al* [20] utilized a crossed electron - target beam configuration, similar to ours (see Chapter 3), but with both the incident and scattered electrons being monochromated using cylindrical electrostatic analysers. Jureta [21] measured

the threshold electron impact spectra for water using a crossed-beam electron spectrometer. This method emphasises the optically forbidden transitions and hence he has effectively reported on the triplet spectroscopy. This was a very important study to us for characterisation of the triplet features, in terms of both width and position, as there is less interference from any adjacent optically allowed singlet transitions.

Another electron based study of note is that from Compton *et al* [57], although we have not included it in table 2.2 or in our previous discussion due to its limited range and energy resolution. Compton *et al*'s method involved measuring the threshold electron impact spectrum by using a time-of-flight mass spectrometer to measure SF_6^- or SF_5^- ions, that resulted from the capture of electrons which had lost most of their energy after colliding with a water molecule.

There have been more spectroscopic investigations into water using photoabsorption. Herzberg [39] provided a summary of those results up to 1966, including work from Johns [58], Price [59], Bell [60], Watanabe and Zelikoff [61] and Wilkinson and Johnston [62]. There have subsequently been more photoabsorption studies, with the most recent by Mota *et al* [22]. Also of note at this point is the experimental study by Chan *et al* [51], who used a dipole (e,e) spectrometer to measure energy loss spectra at high impact energy and low scattering angle. They then obtained a photoabsorption spectrum by applying an approriate scaling factor, and for this reason we have included it in this part of our discussion. The photoabsorption studies were very useful to us in characterising the features arising from optically allowed transitions, as there is little interference in their spectra from any optically forbidden ones.

There have been many theoretical studies into the spectroscopy of H_2O, with a summary of these being given in table 2.1 and where appropriate in the text that follows. Some of these theoretical studies had the aim of improving a method, or validating a method, and hence did not actually provide more accurate values for the parameters of interest to us. Hence not all the theoretical studies needed to

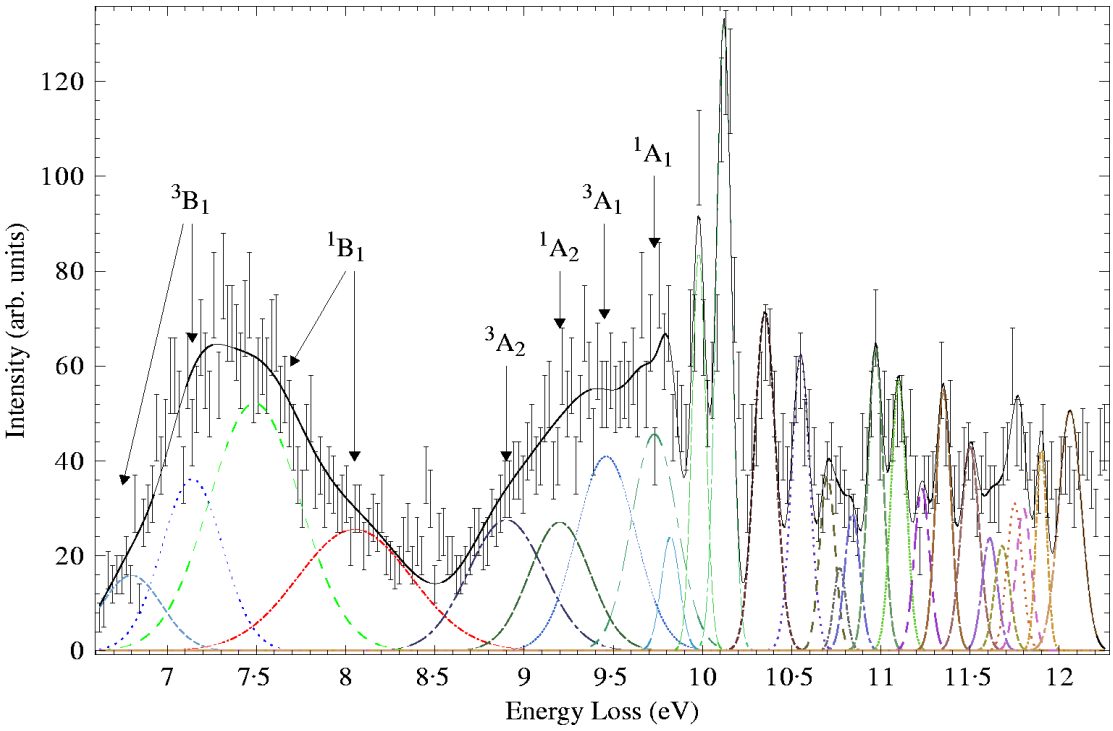

Figure 2.1: A typical energy loss spectrum from the present study, in the electronic state excitation region. Here E_0= 20eV and θ= 30°. See Chapter 3 for full detailes of the spectral deconvolution also shown on this plot.

be included in our discussion in as much detail.

The first feature in our measured energy loss spectra is a broad continuum ranging from about 6.5eV to 8.5eV energy loss. This can be seen in figure 2.1, which is a typical example of the energy loss spectra measured in the present study. We have identified this initial feature as originating from the $1b_1 \rightarrow 3sa_1$ $\tilde{a}^3B_1$ and $\tilde{A}^1B_1$ transitions at 7.14eV and 7.49eV energy loss respectively. In the past there has been some controversy over the nature of the lowest electronic-state transition in water. Some electron spectroscopy studies eg Compton *et al* [57], Knoop *et al* [50], Skerbele *et al* [56] and Trajmar *et al* [18] found a weak and broad feature at 4.5eV energy loss. The nature of this transition sparked much discussion in the literature, as the lowest calculated transition at the time was for the $\tilde{a}^3B_1$ transition which Claydon *et al* [41] found at 6.2eV. Many explanations for this lower lying feature were put forward, with a summary of them being given by Yeager *et al* [63]. This discussion was finally concluded when Yeager *et*

al proposed that this feature was not the result of a transition from the ground state, and that the $\tilde{a}^3B_1$ state was that observed by Knoop *et al* at 7.2eV energy loss. In all our measured spectra we found no evidence for any structure at 4.5eV energy loss.

The lower energy loss region of the water spectrum has been well studied by both experiments and calculations. As initial estimates for the energy loss values of the $\tilde{a}^3B_1$ and $\tilde{A}^1B_1$ states, for use in our spectral deconvolution (see Chapter 3), we chose the values recommended by Winter *et al* [42]. Winter *et al* performed a configuration interaction (CI) calculation of the electronic state energies, and they also compiled a set of recommended data. This set comprised values determined by the available electron impact work, and where they were unavailable the photoabsorption value was given. For triplet states, if there was any doubt in the electron data, the triplet - singlet energy spacing, as determined from their CI calculation, was applied to the corresponding singlet optical value. In the case of the $1b_1 \rightarrow 3sa_1$ transition the value of 7.49eV that Winter *et al* recommended for the $\tilde{A}^1B_1$ state, was in fact the widely accepted value determined by Watanabe and Zelicoff [61] in a photoabsorption study. Their value [42] of 7.14eV for the $\tilde{a}^3B_1$ state was derived by subtracting the CI calculated triplet - singlet spacing of 0.35eV from the $\tilde{A}^1B_1$ value. In both cases these initial estimated energies for transitions to the $\tilde{a}^3B_1$ and $\tilde{A}^1B_1$ states proved to give excellent fits in the spectral deconvolution of all our measured energy loss spectra. As such they were adopted by us as our preferred values for this study. Note that our value of 7.14eV for the $\tilde{a}^3B_1$ state is in quite good accord with that of Jureta [21], particularly when allowance is made for the energy resolution of both his apparatus and that employed in the present study.

In fact all of the experimental studies, as listed in table 2.2, agree with the present assignments to within 0.14eV for the $\tilde{a}^3B_1$ state and 0.09eV for the $\tilde{A}^1B_1$ state. While there have been considerably more theoretical spectroscopic studies, most of their results also agree with our assignment of the $\tilde{a}^3B_1$ transition energy to within 0.12eV. The exceptions to this are the intermediate neglect of differential

overlap (INDO) calculation of Claydon *et al* [41] and the improved virtual orbital (IVO) calculation by Goddard and Hunt [19], who both calculated values more than 0.4eV lower. For the $\tilde{A}^1B_1$ state all the calculations, including those from references [19] and [41], are within 0.19eV of our preferred value. Claydon *et al* [41] considered anything to within 1eV of their calculated values to be in good agreement, although they expected their calculations to give an overestimate of the true energies which is not what is found (see table 2.1). They utilized a rather simple basis set (compared to the more recent calculations) and in this study they also employed their calculated potential energy curves in conjunction with measured spectroscopic data, in forming their results. We disagree with their assignment of the $\tilde{a}^3B_1$ state. Despite calculating a value of 6.2eV for this state's excitation energy, they assigned it as the feature appearing at around 4.0eV in some experimental spectra e.g. Compton *et al* [57]. As discussed earlier that feature is probably spurious, so their assignment must be incorrect. We believe that the feature they have assigned as being due to the $^1A_2$ state at 6.5eV, is in fact due to the $\tilde{a}^3B_1$ state. Despite some energy discrepancies, Goddard and Hunt [19] are in agreement with the assignment of the $\tilde{A}, \tilde{B}, \tilde{C}$ and $\tilde{D}$ transitions from previous photon-spectroscopy work ([61], [58], [59]) and the present study.

The next section of the energy loss spectra, from about 8.5eV to 10.2eV energy loss (see figure 2.1), consists of a broad peak followed by several large sharp peaks at the high energy loss end. In this region there are significantly more overlapping features than the last. Based on the summary in tables 2.1 and 2.2 and the optimum spectral fit to all our measured energy loss data, we have assigned the features in this area of the spectra to originate from the $1b_1 \rightarrow 3pb_2$ $^{3,1}A_2$ states at 8.90eV and 9.20eV respectively, the $3a_1 \rightarrow 3sa_1$ $\tilde{b}, \tilde{B}$ $^{3,1}A_1$ states at 9.45eV and 9.73eV respectively, the $1b_1 \rightarrow 3pb_1$ $\tilde{d}, \tilde{D}$ $^{3,1}A_1$ states at 9.79eV and 10.14eV respectively and the $1b_1 \rightarrow 3pa_1$ $\tilde{c}, \tilde{C}$ $^{3,1}B_1$ states at 9.93 and 9.98eV respectively. Hence the sharp peaks at the end of this region of our energy loss spectra are largely due to the $1b_1 \rightarrow 3pa_1$ $\tilde{c}^3B_1$ and $\tilde{C}^1B_1$ and $1b_1 \rightarrow 3pb_1$ $\tilde{D}^1A_1$ transitions. The $1b_1 \rightarrow 3pb_2$ $^3A_2$ and $^1A_2$ states are found to be quite broad and of relatively

low intensity. On the other hand while the $3a_1 \rightarrow 3sa_1$ $\tilde{b}^3\mathrm{A}_1$ and $\tilde{B}^1\mathrm{A}_1$ features are also quite broad, they have relatively higher intensity. The $1b_1 \rightarrow 3pb_1$ $\tilde{d}^3\mathrm{A}_1$ and $1b_1 \rightarrow 3pa_1$ $\tilde{c}^3\mathrm{B}_1$ features are quite small, and are somewhat swamped by the other features. This makes their unique spectral deconvolution from our measurements somewhat problematic, with the errors we ultimately quote on their differential cross sections reflecting this.

Our initial estimates for the energies of the $1b_1 \rightarrow 3pb_2$ $^{3,1}\mathrm{A}_2$ and $3a_1 \rightarrow 3sa_1$ $\tilde{b}, \tilde{B}$ $^{3,1}\mathrm{A}_1$ transitions were again taken from the values recommended by Winter *et al* [42]. However the $1b_1 \rightarrow 3pb_2$ $^3\mathrm{A}_2$ transition was later assigned to the position recommended by Chutjian *et al* [20] at 8.90eV, as this led to fits in better agreement with the spectra measured in the present study. Most of these energy values (see table 2.1) are in agreement with the available calculations, to within 0.28eV. The most notable exception to this statement is again from the calculations of Claydon *et al* [41], who calculated values approximately 1eV too low for the $^{3,1}\mathrm{A}_2$ and $\tilde{b}^3\mathrm{A}_1$ states and approximately 1eV too high for the $\tilde{B}^1\mathrm{A}_1$ states. Upon comparing the results of their calculation [41] with some data from electron impact spectra (in this case that of Skerbele *et al* [56]), Claydon *et al* mistakenly assigned the $1b_1 \rightarrow 3sa_1$ $\tilde{a}^3\mathrm{B}_1$ transition as being due to the $^1\mathrm{A}_2$ transition. Clearly the work of Claydon *et al* must be treated cautiously.

Energies calculated for the $1b_1 \rightarrow 3pb_1$ $\tilde{d}^3\mathrm{A}_1$ excitation are mostly within 0.11eV of the value we assigned, including that from Goddard and Hunt's calculation. Here, however, the full configuration interaction (FCI) and coupled cluster singles doubles and approximate triples (CC3) calculations of Larsen *et al* [46], give values which are considerably higher than ours. In their work Larsen *et al* calculated FCI excitation energies and compared them to the coupled cluster hierarchy of calculations in what was essentially an evaluation of the coupled cluster approach for triplet excitations. This study was complementary to that of Christiansen *et al* [45], who carried out a similar study for the singlet excitations. Larsen *et al* [46] found best agreement between their FCI calculations and those from the CC3 approach. The CC3 calculation is an approximation to the

CCSDT (coupled cluster singles, doubles and triples) methodology, which significantly improves computation time. Indeed in their study on triplet excitations in H_2O, Larsen *et al* generally found the CC3 calculations gave good agreement with the FCI results. For most of the states in the energy loss region we are now considering, these calculations [46] and [45] are also in good agreement with our energies and assignments and with the results from most other calculations. The exception is the $1b_1 \rightarrow 3pb_1$ $\tilde{d}^3A_1$ transition for which they have calculated, in both their FCI and CC3 methods, a value that is about 1eV too high. We note here that the singlet calculations of Christiansen *et al* [45] do not consider the corresponding $\tilde{D}^1A_1$ transition.

The two final transitions in this 8.5-10.2eV energy loss region have been identified as being due to the $1b_1 \rightarrow 3pa_1$ $\tilde{C}^1B_1$ and $1b_1 \rightarrow 3pb_1$ $\tilde{D}^1A_1$ transitions. Most of the calculated values for these transitions are within 0.07eV of our preferred energies, with the exception of the CCSD+T (coupled cluster singles doubles and approximations at the triples level (i.e. different to CC3)) calculation of Kaldor [43] which finds values that are more than 0.15eV higher. Kaldor [43] employed the open-shell coupled cluster method at both the CCSD (coupled cluster singles and doubles) and the CCSD+T level, to compute the relevant excitation energies. The CCSD+T approach is an approximation to the coupled cluster singles, doubles and triples calculation and is similar to the CC3 method of Larsen*et al* [46] and Christiansen *et al* [45]. Kaldor [43] compared the results of his calculations using different basis sets, to corresponding results from configuration interaction studies (with the same basis sets) and to the values recommended by Winter *et al* [42]. His best agreement (when compared to the CI results) was obtained from the CCSD+T calculations, the highest level of his calculations [43]. Based on the observation that theory is consistently overestimating the excitation energy for the $1b_1 \rightarrow 3pb_2$ $^{3,1}A_2$ transitions, when compared to experimental results, Kaldor [43] suggests that these transitions may be inappropriately assigned by experimentalists to energies that are too low. We believe the balance of evidence suggests otherwise.

In summary, in the 8.5eV to 10.2eV energy loss range we have assigned 8 electronic state excitations. This is similar to what other previous experimental and theoretical works have done, and in general we are in reasonable agreement with both their assignments and energies. Two glaring exceptions to this assertion are discussed in the next paragraph.

The CI calculation of Winter *et al* [42] and the IVO calculation of Goddard and Hunt [19], both find the $3a_1 \rightarrow 3sa_1$ $\tilde{b}^3\mathrm{A}_1$ state to lie at lower energy than that for the $1b_1 \rightarrow 3pb_2$ $^1\mathrm{A}_2$ state. Similarly they also both find that the $1b_1 \rightarrow 3pb_1$ $\tilde{d}^3\mathrm{A}_1$ state lies at a lower energy than the $3a_1 \rightarrow 3sa_1$ $\tilde{B}^1\mathrm{A}_1$ state. These are the only calculations to find this ordering (see table 2.1). In fact Winter *et al*, in their recommended data set, repudiate their own results and suggest the energy ordering that we are using. The recommended value given by Winter *et al* [42], for the energy of the $1b_1 \rightarrow 3pb_1$ $\tilde{d}^3\mathrm{A}_1$ transition, was obtained from the electron scattering work of Trajmar *et al* [18], which is in good agreement with that of Chutjian *et al* [20]. Note also that the energy value recommended by Winter *et al* [42] for the $3a_1 \rightarrow 3sa_1$ $\tilde{B}^1\mathrm{A}_1$ transition, was taken from the optical measurements of Johns [58]. In respect to the $3a_1 \rightarrow 3sa_1$ $\tilde{b}^3\mathrm{A}_1$ case, the energy Winter *et al* recommend for this transition was derived using the value from Johns [58] for the $3a_1 \rightarrow 3sa_1$ $\tilde{B}^1\mathrm{A}_1$ transition and subtracting the triplet-singlet spacing calculated using the CI model. Finally the recommended energy value for the $1b_1 \rightarrow 3pb_2$ $^1\mathrm{A}_2$ transition in Winter *et al*, was obtained from the electron scattering work of Chutjian *et al* [20].

The rest of the energy loss spectrum has many more overlapping features and unfortunately there are less theoretical studies covering this area. In particular the area from 10.1eV to 11eV energy loss has been rather sparsely studied. With respect to the available theories, we highlight the work of Goddard and Hunt [19], Cai *et al* [47] and Trofimov *et al* [48]. The calculation of Cai *et al* [47] uses a density functional theory (DFT) method and was undertaken in order to improve upon the existing DFT models. This it achieved, but its accuracy is still considerably less than the more computationally expensive *ab initio* methods. As such we have

not used their results in making our spectral assignments. The 3rd order algebraic diagrammatic construction (ADC(3)) study by Trofimov *et al* [48], was similarly a study made in order to improve the method rather than to determine more accurate values for the electronic-state energies. As such it was also ignored in making our spectral assignments.

Chutjian *et al* [20] made a comprehensive experimental study of the spectroscopy of H_2O (and D_2O) from 4.2 to 12eV energy loss. They compared spectra resulting from varying the kinematical conditions in order to enhance either the optically allowed transitions (large incident energy, small scattering angle) or the spin/symmetry forbidden transitions (low residual energy and high scattering angle). In that work they made use of the calculations of Goddard and Hunt [19], the previous experiments of Trajmar [18], as well as some earlier optical studies, in assigning their spectra. Hence the generally good agreement (to within 0.12eV) between most of the available works in this energy loss region is not really that surprising.

The transition which generates the most controversy, in this region of 10.01eV to 11eV energy loss, is the $1b_1 \rightarrow 4sa_1$ $\tilde{E}$ $^1B_1$ excitation. In this case Trajmar [18] assign it to the feature at 11.01eV, in line with optical values of Herzberg [39]. Chutjian *et al* [20] and Goddard and Hunt [19] also find the first transition of the $\tilde{E}$ Rydberg series to be at 11.01eV, but have assigned its origin as being due to the $1b_1 \rightarrow 3da_1$ $^1B_1$ excitation. For this transition, as with the rest of the electronic-state excitations in this region of energy loss, we have adopted the assignment of Chutjian *et al.*

There are few electron based studies to cover the spectral region from 11eV to about 11.75eV energy loss. The most comprehensive studies of these spectral regions were those of Goddard and Hunt [19] and Chutjian *et al* [20]. This region of the spectrum has a very large number of overlapping features and little clear structure, making it particularly challenging to deconvolute. Indeed to quote Chutjian *el al* [20] "A clear assignment of the electronic transitions above $\approx$11.12eV

is not possible because of the multitude of electronic transitions (and their possible vibrational excitations!)". The exceptions to this rather global statement are the $3a_1 \rightarrow 3pb_2$ $\tilde{f}, \tilde{F}$ $^{3,1}B_2$ transitions, which Chutjian *et al* found at energy loss values of 11.11eV and 11.46eV respectively. For their assignment [20] of the rest of the spectrum they used a method similar to that of Winter *et al* [42], which we described earlier in this section. In fact Chutjian *et al* [20] used the optical Rydberg series data from Price [59] to determine the energy of the singlets, and then they applied to those energies the calculated (Goddard and Hunt [19] and Winter *et al* [42]) triplet-singlet spacing in order to determine the energies of the corresponding triplet transitions. For the $^3A_2$ and $^1A_2$ states, and others for which there are no optical values, Chutjian *et al* [20] used the values calculated by Winter *et al* [42] or Goddard and Hunt [19]. For our initial estimates of the excitation energies for this section of the energy loss spectrum we again used the values from Chutjian *et al* [20].

Above 11.75eV energy loss there is still a paucity in the number of electron based studies. In this region of the spectra no results are presented by Goddard and Hunt [19], however Winter *et al* [42] have given both the results from calculations and a recommended set of data. Chutjian *et al* [20] have also given results for this region of the spectra, and where these two sets of data overlap, Chutjian *et al* have employed the CI calculated values from Winter *et al* to assign their spectra. As initial estimates in our deconvolution process for this region of the spectra, we have used the energies and assignments from Winter *et al* [42] and Chutjian *et al* [20]. Larsen *et al* [46] calculated energies, using their two approaches (FCI and CC3), for the $3a_1 \rightarrow 3pb_1$ $^3B_1$ state at 11.32eV and 11.30eV, which are more than 0.5eV lower than the value recommended by Winter *et al*. In this instance the energy cited by Winter *et al* was obtained by applying the value they calculated for the triplet-singlet splitting, to the singlet value found by Watanabe and Jursa [64]. Here we chose to use the values presented by Winter *et al* [42] for our deconvolution.

The most recent paper to review the spectroscopy of water was from Itikawa

and Mason [12]. In their review they did not attempt to give a recommended set of values for the excitation energies, but they did summarise the most recent/influential electron, optical and theoretical studies as being those from Winter *et al* [42], Chutjian *et al* [20], van Harrevelt and van Hemert [65], Gorfinkiel *et al* [35] and Chan [51]. Gorfinkiel *et al* [35] calculated potential energy surfaces and vertical excitation energies for the $1b_1 \rightarrow 3sa_1$ $\tilde{a}, \tilde{A}$ $^{3,1}\mathrm{B}_1$ and $3a_1 \rightarrow 3sa_1$ $\tilde{b}, \tilde{B}$ $^{3,1}\mathrm{A}_1$ transitions, as a part of their determination of the integral cross sections for excitation of these same states by electron impact. We have not included the results of their computations in table 2.1 due to the limited number of states their calculation covered. The calculation by van Harrevelt and van Hemert [65] is also not included in our table, as they reported only singlet excitation energies for their study on the photodissociation of water.

Chapter 3

Experimental Procedures

In this study we have determined differential cross sections (DCSs) and integral cross sections (ICSs) over the incident electron energy range 15 to 50eV. The DCS data were derived from electron energy loss spectra (EELS), which were measured on a crossed beam spectrometer described next in section 3.1. These EELS were measured over the angular range 10° to 90°, at 10° intervals, and the energy loss range ≈-0.5eV to 12eV. The ICS were derived from the DCS data as described in section 3.4.

In order to determine the DCS from the EELS a measure of the intensity for each electronic excited state feature is required. As was expected on the basis of our discussion on water's spectroscopy in Chapter 2, the measured EELS contain many overlapping features. Accordingly, considerable care was taken in deconvoluting the spectra, with full details of this deconvolution procedure given in section 3.2. Once the intensity for each feature, at each measured angle and incident electron energy, was determined the corresponding DCSs were derived using the method outlined by Nickel *et al* [66]. Details of this latter procedure are given in section 3.3.

The DCS data were then interpolated and extrapolated to 0° and 180° using a molecular phase shift analysis (MPSA) technique [67]. The ICS at each incident electron energy were then determined by integrating these DCSs across this

angular range. This procedure is described in full later in section 3.4.

3.1 Apparatus

The crossed beam apparatus has been discussed in detail previously by Brunger and Teubner [68] and in numerous PhD theses since then, most recently by Green [69]. Several changes have, however, been made since these original descriptions, including the replacement of the initial turbomolecular pump, some changes to the gas handling system which were detailed in my honours thesis [70], and some alterations to the channel electron multiplier (channeltron) mounting system.

The spectrometer is housed in a high vacuum chamber which achieves a base pressure of typically 3.7×10^{-7}torr, as measured by a Granville-Phillips ion-gauge with a Leybold-Heraeus IONIVAC IM 210D monitor. An automatic failsafe feature is incorporated into the ion-gauge monitor, so that the power will be shut down to the pumps, filament power supply and channeltron back high voltage power supply if the chamber pressure leaves the preset range 2×10^{-4}torr to 5×10^{-9}torr. The vacuum system originally consisted of a Pfeiffer-Balzers TPH510 turbomolecular pump, backed by an Edwards E2M-18 rotary pump. The backing pressure is monitored by a Granville Phillips 275 monitor, and is typically between 3 and 100mtorr depending on whether the system is under load or not. The original turbomolecular pump was designed for use with corrosive materials, it employed Fomblin F3 oil and had a special pumping injection system for the oil. Towards the end of my experiments this pump failed, the suggested fault being a malfunction in the oil injection system. As that pump could not be repaired it was replaced by another turbomolecular pump: Pfeiffer Balzers TPU510. This replacement pump was not designed for use with corrosive materials, and so required regular pump oil changes. This is in stark contrast to the original pump which had one oil change at the beginning of my experimental work, and did not need another before it was replaced. The crossed beam apparatus is powered by

mains power, with a Powerware 9^{120} uninterruptible power supply (UPS) connected to ensure continued operation in the event of a mains power failure. This facility was tested during the course of this project and the UPS was found to last for more than 3 hours under near full load. The ambient magnetic field at the interaction region is cancelled by three sets of mutually orthogonal Helmholtz coils, and a layer of CO-NETIC AA magnetic shielding which surrounds the chamber. These precautions ensure that the residual field in the chamber, as measured by a magnetometer, is less than 1mGauss.

A schematic diagram of the spectrometer, with its general design being based on that of Read *et al* [71] and Brunt *et al* [72], is shown in figure 3.1. The electron source is a thoriated tungsten filament on a black glass base (Energy Beam Sciences #VS-AE-N), through which between 1.6A and 2.3A of current is passed to bring about thermionic emission. The emitted electrons are then transported with a Pierce extraction system [68], onto the first collimating aperture (GA1), which is 1mm in diameter. The function of this and all the collimating apertures is to reduce the spatial spread of the electron beam. Electrons transmitted through this aperture are transported and focused onto the entrance plane of the monochromator by the three element aperture-type lenses GL1 and GL2. The collimating apertures GA2 and GA3 (each 1mm in diameter) are incorporated into the design to ensure a narrow on-axis beam at the monochromator entrance, while deflectors D1 and D2 allow us to maximise the flux of electrons (current) through these apertures by 'deflecting' the beam in the X- and Y- directions.

The potentials applied to all the lenses, deflectors and apertures inside the chamber were controlled by external rack-mounted power supplies. These potentials were fed into the chamber through several AMPHENOL plugs positioned on the top flange of the vacuum chamber. This is in fact the case for all the spectrometer lenses, deflectors and apertures, as well as the hemispheres and their fringe-field correcting hoops (on both the selector and analyser side of the apparatus). Details of the typical operating potentials for all these electrostatic elements can be found in Brunger [74] and are not listed again here.

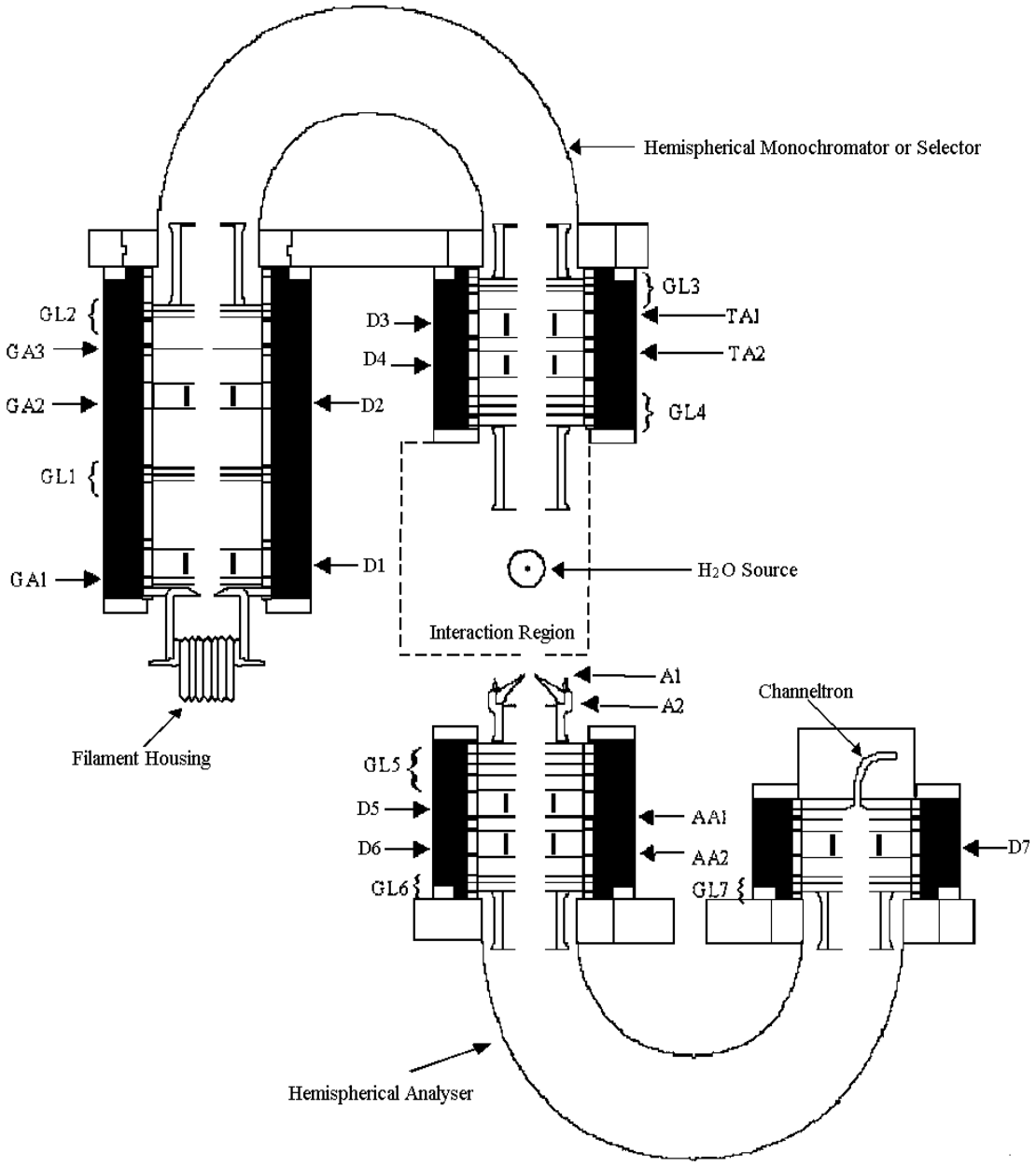

Figure 3.1: Schematic diagram of the crossed beam apparatus. Figure copied from B. Mojarrabi [73]. The H_2O vapour flows out of the page, with the lenses (GL), deflectors (D) and apertures (GA, TA, A and AA) being described in the text.

While the lenses, deflectors and apertures will ensure that the electron beam has a small spatial spread of good flux, the energy width of the beam produced in this manner is still quite large. Typically, electrons produced by thermionic emission with a thoriated tungsten filament have an energy width of approximately 0.6eV (FWHM). For the experiments we are attempting, however, we require a much better energy resolution, a point which can be seen by considering the various electronic-state excitation energies in the tables of Chapter 2. This improved energy resolution is achieved in our apparatus by using a hemispherical monochromator or selector. The monochromator itself consists of two parallel hemispherical charged surfaces, the outer with a radius of 52.5mm and the inner with a radius of 27.5mm. Fringe field correcting hoops are also incorporated into this monochromator, and are necessary to maintain the performance of the monochromator for the reasons outlined by Brunt *et al* [72]. The voltages applied on the hoops and hemispheres were determined according to the equations of Brunt *et al* [72].

The mean analysing energy of the monochromator, V_0, is crucial to the energy width (ΔE) of the electron beam transmitted through it. This can be seen from the following equation [72]:

$$\Delta E = V_0 \left(\frac{1.62 r_{beam}}{2 r_0} + 0.23 \theta_{beam}^2 \right). \tag{3.1}$$

In equation (3.1) r_{beam} is the radius of the electron beam at the monochromator entrance, r_0 is the mean radius of the monochromator (=40mm) and θ_{beam} is the pencil-angle at its entrance. Clearly the smaller is the value of V_0 the better is the energy resolution (narrower ΔE). In practice, however, more heavily monochromating the beam reduces the number of electrons that are actually transmitted. Hence a balance must be struck between achieving high resolution and having enough electron flux to perform the experiment. For the experiments reported in this thesis, the mean analysing energy of the selector was usually 2.0eV.

After the electrons have passed through the selector they are transported to the interaction region by the aperture-type lenses GL3 and GL4. Again the apertures TA1 and TA2 serve to collimate the beam while the deflectors D3 and D4 help to

keep more of the beam on-axis and also they help increase the electron flux. The last deflector, D4, additionally acts to maximise the overlap of the electron and target molecular beams, and has quite a large influence on the direction of the electron beam as it enters the interaction region. For this reason it was standard practice not to adjust it once the true zero scattering angle location had been confirmed. The last lens in this stack, GL4 (see figure 3.1), sets the energy of the incident electron beam which can be from ≈0 to 50eV. GL4 is a zoom lens and has four lens elements (instead of three like GL1-3), although only three have independent potentials at any given time. In normal operation (for our measurements that is in the so-called "high energy mode") its second element, GL4B, is set at the same potential as its first element, GL4A. The final element of GL3 (GL3C) is also set at this same potential, thereby setting up a field-free region between these GL3C and GL4A/B elements. The third element, GL4B', is independently set on its voltage supply while it is the final element of this lens, GL4C, that ultimately defines the beam energy E_0.

The spectrometer can be operated in either of two modes. In the first the beam energy (E_0) is held constant and the scattered signal as a function of energy loss recorded at a given scattering angle. Typically the scattering angle would then be changed and the whole process repeated. In the second mode excitation functions, for a given scattering process, could be measured. Here the scattered signal is recorded as a function of the incident electron beam energy, again at a fixed and well-defined scattering angle. In practice, if an excitation function is to be measured, the voltage on GL4C is ramped across a range of values set on the relevant external rack-mounted power supply. Another linear voltage ramp can also be set up on GL4B', if necessary, to help maintain the beam characteristics (focus and size etc) as the voltage of the final lens element is ramped. This second ramp function was not utilized by us, as only relatively few excitation functions were measured (mainly for the beam energy calibration, as described below) during this project. As those measurements were taken over such a small energy range, it was not necessary to apply this additional ramp to maintain the

beam character. Note that the excitation function option would have become more important, had this project involved studying possible near-threshold resonance effects.

The interaction region is defined by the intersection of the electron beam with the molecular beam. This region is surrounded by a shield which is shaped like a half-cylinder. The interaction region shield has its open edge facing the incident electron beam with a slit cut into it, at the height of the nozzel through which the molecular beam effuses, to enable the scattered electrons to exit. This shield is made of stainless steel and has the same voltage applied to it as all the other surfaces near the interaction region - that being the voltage on GL4C. The purpose of this shield is to prevent, or significantly reduce, the likelihood of stray electric fields penetrating into the interaction region.

The molecular beam effuses into the interaction region through a molybdenum tube of ≈0.7mm internal diameter, after passing through the gas handling system. The present gas handling system is actually more complicated than is strictly necessary for the current experiments, as it was originally designed to be used for the application of the relative flow technique [66]. Nonetheless it was still suitable, after a relatively minor modification, for our purposes here. During the course of this study a glass sample vessel, capable of holding a liquid sample, was fitted to the gas line. Full details of this modification can be found in Thorn [70]. The pressure of the H_2O vapour in the gas line is monitored with an MKS Baratron 690A11TRC pressure gauge, as read on an MKS 270 signal conditioner. The flow of target gas into the chamber is controlled by three SMC VX2230K solenoid valves, and a variable leak valve (Granville-Phillips 203) for fine control of the flow rate.

For the duration of this study the sample vessel was charged with 'ultra pure' H_2O, that had been filtered by a Barnstead E-Pure filtration system. That system employed filtration cylinders using both charcoal and ion exchange resin, to remove all organic and inorganic impurities. This sample vessel sits in an insulated

container, to enable its immersion in liquid N_2 as part of a freeze-pump-thaw cycle, which is repeated several times, to remove any other impurities from the water sample. Provision has also been made in the gas handling line for the sample to be pumped on by a rotary pump (Edwards EDM-12) during the freeze-pump-thaw cycle. The laboratory is reverse cycle airconditioned year round, to a temperature of about 25°C, to ensure that the H_2O sample has a high enough vapour pressure for steady flow into the scattering chamber.

The electron current into the interaction region can be measured using a Faraday Cup assembely. Due to space constraints, this cup can be moved into the interaction region only when the analyser hemisphere is at a scattering angle of 60° or greater, as otherwise they will collide. The Faraday Cup is an essential tool for tuning the electron spectrometer, in that the appropriate voltages for the spectrometer lenses and deflectors are determined, in the first instance, by simply adjusting them to maximise the current measured on the Faraday Cup. If no current is initially detected at the Faraday Cup, the current measured at successive apertures GA1, GA2, GA3, TA1 and TA2 can be used to tune the monochromator until there is a readable signal at the Faraday Cup. Tuning the instrument in this way continues until a stable current, of reasonable magnitude, is measured on the Faraday Cup. Incident electron beam currents in these experiments are typically between 2.0 and 6.0nA.

Electrons scattered from the interaction region are detected by the analyser, which is rotatable in a plane about the interaction region. Electrons scattered towards the analyser pass through the defining apertures A1 and A2, before the lenses GL5 and GL6 focus them onto the analyser hemispheres entrance plane. Note that collimation of the scattered electron beam is provided by the apertures AA1 and AA2 (see figure 3.1). GL5 is another zoom lens, with a similar function and purpose to GL4. In particular, here it is used to help compensate for the difference in efficiency of the analyser in transmitting scattered electrons of different energies. For example in the present experiments variations in the analyser transmission function start to become significant at 20eV incident energy, where

an electron which loses 12eV of energy to the H_2O molecule ends up with only 8eV residual energy. Hence this scattered electron has lost more than half of its incident energy, so that the difference in the efficiency of the analyser in transmitting electrons with 20eV of energy and those with 8eV of energy possibly starts to become significant. Our steps to try and circumvent this important experimental difficulty are described later, although here we note that our original procedure following Pichou *et al* [75] was replaced with the more recent philosophy of Allan [76] during the course of this study. In practice, we utilized an additional negative voltage ramp, applied to the second element of GL5, to try and maintain the focal properties of this lens irrespective of the scattered electron energies. After this zoom lens there are two sets of deflectors D5 and D6 incorporated into the design, in order to maximise the scattered electron flux through the apertures AA1 and AA2. Thereafter a second lens, GL6, focuses the beam onto the entrance plane of the analyser hemisphere. Details of the typical potentials that are applied to these various electrostatic elements can also be found in Brunger [74].

The analyser hemispheres are the same design and have the same function as the selector hemispheres, and so we will not repeat its details here. Rather at this time we highlight that all the analyser potential supplies are referenced to a voltage rail known as the analyser earth. This rail is ramped during the course of an electron energy loss experiment, in order for the analyser to preferentially transmit electrons of the desired energy loss. The ramp is commonly referred to as the energy loss ramp (again a linear voltage ramp), and it is controlled by a multichannel analyser (MCA) as described later.

Energy analysed electrons are now focused onto the detector, a channeltron (initially Philips B310BL), by lens GL7. In addition they are passed through a final deflector D7, in order to maximise the current onto the channeltron. The channeltron front was originally spot welded into place, on the front of its housing, and spot welded at the rear to a cable that ultimately leads to its high voltage power supply. This mounting system was changed early in the present study to allow the channeltron to be connected without the weld onto the entrance aperture,

and hence allow for easier installation. In this revised configuration the channeltron is now essentially held in place by two pieces of teflon. We note that the initial channeltron (Phillips B310BL) was later replaced with a Photonis X810BL, because of the latters superior operational performance. Scattered electrons are accelerated into the channeltron, with the channeltron front having a potential of about 100V (with respect to analyser earth) while the back of the channeltron sat at about 1700V. The actual values for these potentials were determined by the gain required to produce pulses of appropriate height for detection.

Before the signal from the channeltron is collected in our MCA, it is first passed through an RC pick-off circuit and then into a preamplifier (ORTEC 113). After preamplification the resulting signal is amplified further by an ORTEC 460 amplifier, before being passed through an ORTEC 551 timing single channel analyser (SCA) (this eliminated noise signals lower than ≈0.5V and higher than 10.0V). From here the signal is collected in a Tracor Northern (TN-7200) multichannel analyser. Simultaneously, this signal can also be monitored on a CANBERRA 1775 nuclear counter, a cathode ray oscilloscope (CRO) and an ORTEC 541 ratemeter. The MCA also controls the preset linear voltage ramp that is applied to the analyser earth, in such a way that it stores the number of counts detected as a function of the energy loss value. The MCA stores this data in channels numbered from 0 to 511, which correspond to preset energy loss (analyser earth) voltages of typically between ≈-0.5 to 12eV. Note this applies for when we are collecting the signal plus background data or the background data alone.

The selector electron optics and hemispheres are fixed in space while the analyser optics and hemispheres can be rotated (by hand) with a rotary feedthrough that is located on the top flange of the vacuum chamber. The maximum angle that the analyser can reach is about 95°, at angles greater than this the analyser physically collides with the selector baseplate. The minimum angle at which we have made electroinc - state measurements is 10°, as below this value there is too much noise from the primary electron beam in the elastic channel.

However the analyser can in fact rotate to -30°. The true zero scattering angle is thus found as the point about which the electron elastic or inelastic scattering signal is symmetric, and we believe we can determine this to an accuracy of $\approx \pm 1°$. Note that the angular resolution of the apparatus is estimated to be 1°. The energy resolution of the apparatus is determined from the full width at half maximum (FWHM) of the elastic peak, in a given energy loss spectrum, and for our measurements this is typically between 50 to 65meV. The incident electron energy is calibrated using the Helium 2^2S resonance at 19.366eV, as determined by Brunt *et al* [77]. A typical elastic excitation function in helium, measured at 90 degrees and over the incident electron energy range from approximately 19.2eV to 20.2eV is shown in figure 3.2. Note that a linear background function has already been subtracted from this spectrum and that the position of the minimum in the resonance feature was found by fitting a Gaussian function to it. In the case of the spectrum shown, the resonance was found to lie at 19.7eV which suggests a calibration correction to the beam energy of 0.33eV. This shift is probably due to contact potential effects in the spectrometer. The beam energy calibration was checked regularly and was always found to lie within 0.35eV of the true position specified from Brunt *et al* [77]. We estimate the uncertainty in the incident electron beam energy as $\pm$ 0.050eV.

Each energy loss spectrum takes between 6 hours and about 5 days to measure, depending on the signal level which in turn depends on the actual kinematical conditions being studied. Both the electron current and the molecular beam flux will drift a little over the time taken to measure a spectrum, but great care was taken to maintain optimal tuning conditions during our measurements. The collected data is ultimately transferred from the MCA onto the laboratory computer (digital DECpc LPx^+ 433dx, with Windows 3.11 operating system), before then being further transferred to another higher-level computer (DEC ALPHA 433MHz, 320Mbytes) for analysis.

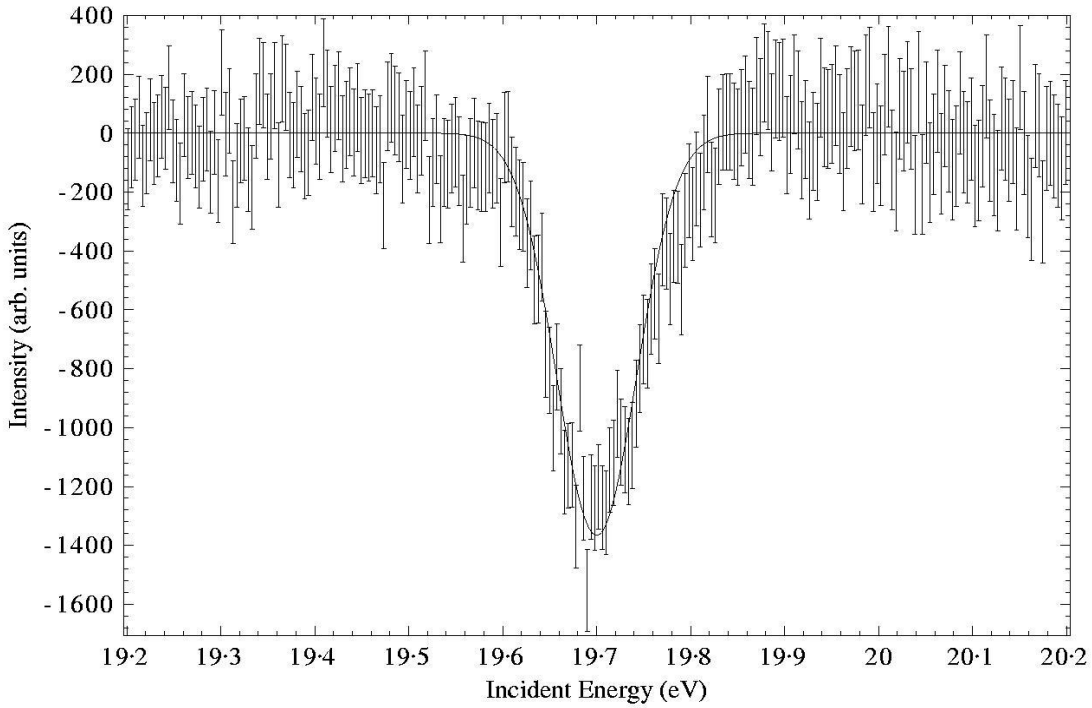

Figure 3.2: Typical elastic excitation function for electrons scattering from helium. The electron scattering angle in this case is 90° and the well known 2^2S resonance is clearly observed. Note the offset from its true energy value

3.2 Spectral Deconvolution

The first stage in deconvoluting the measured EELS is to convert the spectrum stored by the MCA from being a function of channel number to being a function of energy loss. This was achieved in the following manner. The start and end point of the energy loss ramp is preset using a potentiometer, with these values being recorded. The energy width of each of the 512 channels is now determined from channel width = (E_{max}-E_{min})/512. However the energy loss scale is still not yet fixed, this scale is further calibrated by fitting a Gaussian function to the elastic data and fixing the peak position of this Gaussian as zero energy loss.

The spectral deconvolution procedure utilized an existing Fortran program (GLBF, last modified by L.Campbell in 2000) to fit a Gaussian profile to each feature in the measured spectrum. This program uses a least squares fitting technique based on the Marquardt method, as described by Bevington [78], and

was capable of fitting many Gaussian, or Lorentzian, profiles as well as an optional polynomial background. For the present work we did not use the background or Lorentzian fitting options, and only Gaussian profiles of the form given in equation (3.2) were fitted to the data. Namely:

$$f(x) = \frac{B}{\sqrt{2\pi}\sigma} \exp^{\left(\frac{-(x-x_0)^2}{2\sigma^2}\right)}, \tag{3.2}$$

where,

$$\sigma = \frac{\Delta E^w}{2.355}.$$

Note that in equation (3.2) σ is the standard deviation and x corresponds to the energy loss. During the fitting of a given measured energy loss spectrum the amplitude of the Gaussians, $B/\sqrt{2\pi}\sigma$, was the only variable. The position, x_0, and width, ΔE^w, of each fitted Gaussian were largely held constant, at values specified in table 3.1, throughout each individual fit and varied only very minimally between spectra of different kinematical conditions. Note that these values were initially fixed using our knowledge of the molecular spectroscopy of H_2O as detailed in Chapter 2. Indeed we generally found that most changes in x_0 were to within 0.04eV, while the width changes (ΔE^w) were mostly to within 0.08eV. Note that these minor changes in x_0 and ΔE^w were only ever contemplated if a clearly better fit to the EELS spectrum in question would be obtained. This minor possible variation in x_0 and ΔE^w, between different kinematical systems, is physically acceptable, with a similar situation being seen previously in a study of O_2 by Lewis *et al* [79]. In that study Lewis *et al* found that states with strongly mixed Rydberg- and valence-character tended to be rather diffuse, and exhibited a changing peak position in their energy loss spectra as the kinematical conditions were changed. The $\tilde{a}$ and $\tilde{A}\ ^{3,1}B_1$ and the $\tilde{b}$ and $\tilde{B}\ ^{3,1}A_1$ excited states in H_2O are all of strongly mixed Rydberg- and valence-character (Rescigno [80], Chergui and Schwentner [81] and Horsley and Fink [82]), and hence we might expect a similar behaviour from them. Indeed it was in the features of these states where we found the most variability in terms of their optimal positions and widths. A summary of the values of x_0 and ΔE^w that we typically applied in our spectral deconvolutions is

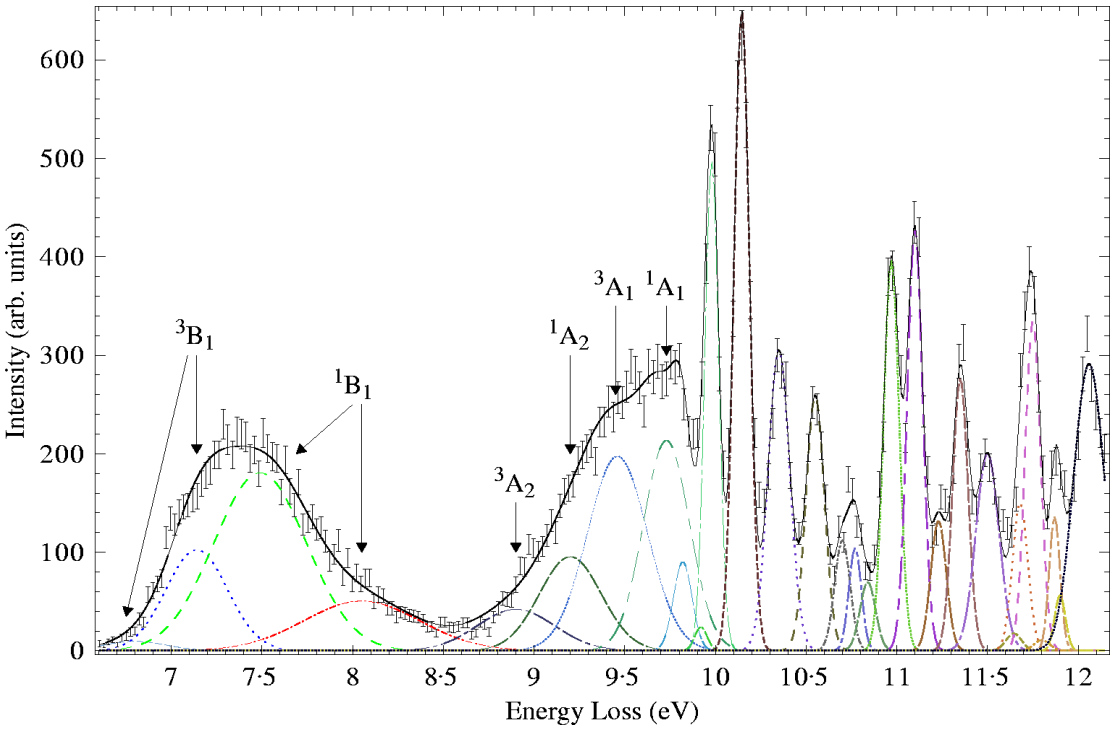

Figure 3.3: Deconvoluted energy loss spectrum, at 40eV and 20°. The more important electronic-state excitations are as indicated on this figure. The elastic peak has been suppressed for enhanced visualisation of the electronic excited states.

given in table 3.1, while an example of a deconvoluted spectrum is given in figure 3.3. It should be clear from this spectrum that the fit to the measured data is very good.

Of course the quality of the fit indicated in figure 3.3 did not happen instantaneously. In our initial attempts to deconvolute the measured spectra, the input values for the peak position and width of each feature were taken directly from previous studies as described in Chapter 2. These initial values, in some cases, did not lead to adequate fits of our spectra, and so under these circumstances some were adjusted slightly until a good fit to the data was obtained. As noted previously, a summary of the final widths and the positions of each peak, which we typically employed for our spectral deconvolution, is shown in table 3.1. Many of the transitions, particularly above 11eV where the spectra are much more detailed, are listed in the table as being degenerate in energy. This was done because given our energy resolution and the strongly overlapping nature of these transitions, a

unique spectral deconvolution for each of them would have been very problematic. Hence for these states we have included in our deconvolution only one Gaussian to represent a group of overlapping transitions. Another problem we encountered was that the profiles of the $\tilde{a}^3B_1$ and $\tilde{A}^1B_1$ features are quite asymmetric, so that using a single Gaussian profile to represent them would be unphysical. Note that their observed profiles can be explained by the mixed Rydberg and valence character of these states [79]. To adequately fit this section (6.5-8.5eV) of the spectrum, we used a single extra Gaussian for each of these transitions. Thus the use of two Gaussians for the $\tilde{a}^3B_1$ and $\tilde{A}^1B_1$ states is not due to any fundamental new physics, it is simply an artefact of our fitting procedure.

The output from the spectral deconvolution procedure was essentially an area for each feature in each spectrum. These areas represent the relative intensity of each feature, and each is a sum over the rovibrational levels of the particular electronic excited state. With respect to the elastic peak, this arises from scattering from the vibrational ground state (the rotational states were unresolved in this experiment). Higher vibrational excitations of the ground electronic-state e.g. bending and/or stretch modes, are also resolved in our experiment. These respective areas were now used in the determination of the desired DCSs, as described in section 3.3.

3.3 Differential Cross Sections

The procedure used to determine differential scattering cross sections, also referred to as the angular dependent cross sections, is essentially that described by Nickel *et al* [66] for inelastic excitation. The intensity, $\dot{N}^e(E_0,\theta)_n$, of a feature, n, in the energy loss spectrum, for incident electrons with energy E_0 and scattered through an angle θ, can be related to the differential cross section for that transition by the following equation [66]:

$$\dot{N}^e\left(E_0,\theta\right)_n = \int_{V,E} \sigma_n\left(E,\theta(r)\right)\eta\left(E_R,r\right)N(r)F^e(E,r)\Delta\Omega^e(r)\mathrm{d}E\mathrm{d}V_0 \qquad (3.3)$$

State	Position (eV)	Width (eV)
$\tilde{a}^3B_1$	7.14	0.40
	6.80	0.40
$\tilde{A}^1B_1$	7.49	0.60
	8.05	0.75
$^3A_2$	8.90	0.50
$^1A_2$	9.20	0.40
$\tilde{b}^3A_1$	9.46	0.39
$\tilde{B}^1A_1$	9.73	0.30
$\tilde{d}^3A_1[2]$	9.82	0.12
$\tilde{c}^3B_1[2]+\tilde{C}^1B_1[2]$	9.98	0.09
$\tilde{D}^1A_1[2]$	10.12	0.10
$^1B_1[2](100)+^3B_1[3]$	10.35	0.14
$^1B_1[3]+^1A_1[2](100)$	10.55	0.12
$^3A_2[2]$	10.70	0.10
$^1A_1[2](110)+^1B_1[2](200)$	10.77	0.08
$^1A_2[2]$	10.84	0.10
$\tilde{e}^3B_1[4]+\tilde{E}^1B_1[4]+^1A_1[2](200)$	10.97	0.10
$^3B_2+^1B_2+^3B_2[2]$	11.10	0.10
$^3A_1[3]+^1A_2[3]+^1A_1[3]+^3A_2[3]+^1B_1[5]+^3B_1[5]$	11.23	0.10
$^1B_1[6]+^3B_1[6]+^3A_1[4]+^1A_1[4]$	11.35	0.10
$^1B_2[2,3]+^3B_2[3]+^3B_1[7]+^1B_1[7]$	11.50	0.12
$^3A_2[4]+^1A_2[4]$	11.61	0.10
$^3B_1[8]$	11.68	0.10
$^1B_1[8]$	11.75	0.10
$^3A_1[5]+^1A_1[5]$	11.80	0.10
$^1A_1[6]+^3B_1[9]+^1B_1[9,10]$	11.90	0.07
$^1A_1[7]$	12.06	0.15

Table 3.1: Table of the positions (eV) and widths (eV) for the excited electronic states in water, as denoted, that we used in our spectral deconvolution procedure.

In equation (3.3) $\sigma_n(E, \theta(r))$ is the differential cross section for feature n at energy E and angle θ. $\eta(E_R, r)$ is the analyser transmission function, where E_R is the residual energy of the scattered electron ($E_R = E - \Delta E$ = incident energy - energy loss). $N(r)$ is the target beam density, $F^e(E, r)$ is the incident electron beam flux and $\Delta\Omega^e(r)$ is the solid angle subtended by the analyser at the interaction region.

The first simplification to equation (3.3) is to assume that $\sigma_n(E, \theta(r))$ is approximately constant over the energy and angular resolution of our apparatus. In practice this is a physically reasonable assumption so that we can replace $\int_{V,E} \sigma(E, \theta(r))_n \mathrm{d}E\mathrm{d}V$ with $DCS_n(E_0, \theta)$ and move this latter term outside of the integral.

We can further simplify equation (3.3) by dividing it through by the intensity for the elastic feature, $\dot{N}(E_0, \theta)_0$. The respective intensities for the inelastic and elastic features are essentially the areas determined from our spectral deconvolution process and will now be referred to as $A_n(E_0, \theta)$ and $A_0(E_0, \theta)$. The terms $N(r)$, $F^e(E, r)$, and $\Delta\Omega^e(r)$ are independent of the energy of the scattered electron, and hence will be largely the same for the elastic and inelastic features, remembering our caveat on the analyser transmission as a function of energy loss. Hence in the approach we have outlined $N(r)$, $F^e(E, r)$, and $\Delta\Omega^e(r)$ will cancel out of the equation. It should be noted here that the electron flux and the target beam density will vary somewhat over the time it takes to measure our completed spectrum, however the variation over the time it takes to complete a single scan is negligible and so systematic errors in the data due to this effect are expected to be minimal. Despite this it is still good experimental practice to try and operate the spectrometer at optimal tuning, e.g. for faster collection of the data, and we note that this practice was followed throughout this thesis.

The final coefficient we need to consider in equation (3.3) is the analyser transmission function, $\eta(E_R, r)$. This term is a reflection of how efficiently the analyser transmits electrons of different scattered energy, and is therefore dependent on

E_R. Hence it does not cancel out in the ratio. We had earlier referred to the analyser transmission and its importance in these experiments. Historically at Flinders University, the analyser transmission was characterised using the approach of Pichou *et al* [75]. This approach relies on the validity of the Wannier Law [83], whose applicability away from threshold has become increasingly questioned. Recently, Allan [76] proposed an alternative approach which has become our preferred calibration tool for the analyser transmission. In practice this involves applying a negative linear voltage ramp to the mid-element of GL5, where this ramp is set up by measuring the signal at different points across the energy loss spectrum with different voltages applied to the GL5 mid-element (GL5B). The ramp is then determined so that GL5B is as close as possible to its optimal value (maximising the signal) for each energy loss across the range being measured. Note that this process, following Allan [76], is repeated at various angles throughout the scattering angle range to be considered. While the description of the calibration technique may appear to be a little cumbersome, what it seeks to achieve is physically quite simple. Namely, we aim to keep the focus of GL5 at the collimating aperture AA2 irrespective of the value of the energy loss. The effect of this is to keep the analyser transmission constant irrespective of the energy loss. The uncertainty in cancelling out the transmission function when taking the ratio (ie assuming it is constant over the energy loss range) is estimated to be at $\approx$15%. The ratio, taking into account all the aforementioned simplifications, is now shown in equation (3.4) to reduce to:

$$\frac{A_n\left(E_0,\theta\right)}{A_0\left(E_0,\theta\right)} = R(E_0,\theta) = \frac{DCS_n\left(E_0,\theta\right)}{DCS_0\left(E_0,\theta\right)}$$

$$\Rightarrow R(E_0,\theta)DCS_0\left(E_0,\theta\right) = DCS_n\left(E_0,\theta\right) \tag{3.4}$$

As the areas $A_n(E_0,\theta_0)$ and $A_0(E_0,\theta_0)$ are known from our spectral deconvolution of the energy loss spectra, it is clear that $R(E_0,\theta)$ can be determined. As a consequence the DCS of interest, $DCS_n(E_0,\theta_0)$, can also be derived provided

the absolute elastic differential cross section, $DCS_0(E_0, \theta_0)$, is known. Note that in all the above discussion it has been presumed that the appropriately measured background signal has been subtracted from the signal plus background, and in this work, the usual process for measuring this [68] was followed. The elastic differential cross section, $DCS_0(E_0, \theta)$, has been studied extensively by experimentalists and theorists, with a summary of these studies being given by Itikawa and Mason [12]. We have chosen to use the experimental results of Cho *et al* [23], who have estimated the uncertainty in their absolute values at 10% or less at most of their kinematical conditions studied. Cho *et al* [23] employed a crossed beam electron spectrometer with magnetic angle changing device, to access backward angles, and the relative flow technique with helium as the standard to normalize to an absolute scale. Over the energy and angular range we are probing, their DCS were in good agreement with other available experimental work eg Johnstone and Newell [28], and theoretical work including that from Varella *et al* [25] and Okamoto *et al* [26].

3.4 Molecular Phase Shift Analysis Technique

The integral cross section, also called the energy dependent cross section, can be determined from the DCSs by integrating over the scattering angles 0° to 180°, as per the equation:

$$ICS_n(E_0) = 2\pi \int_0^{\pi} DCS_n(E_0, \theta) sin\theta \mathrm{d}\theta \tag{3.5}$$

Before we can evaluate the integral in equation (3.5) we must first interpolate and extrapolate, to 0° and 180°, the DCS data that we have measured. This interpolation and extrapolation is performed using a program called PSA, written (in Fortran 77) by L. Campbell in 1999 and made available to me for my use. This program is based on the molecular phase shift analysis (MPSA) technique of Merz and Linder [84] and it enables us to determine the relevant ICS from the corresponding DCS data, at a given incident electron energy.

Essentially the MPSA technique involves fitting an approximate function, within a least-squares platform, to the DCS data. This fitted function has the form:

$$DCS = |f(\theta)|^2 , \tag{3.6}$$

where the scattering amplitude takes the form

$$f(\theta) = \frac{1}{2ik} \sum_{l=0}^{L} (2l+1) \left(e^{2i\delta_l} - 1\right) P_l(cos\theta) + \frac{1}{2ik} C_L(\theta)$$

and

$$C_L(\theta) = \frac{2i\pi\alpha k^2}{a_0} \left[\frac{1}{3} - \frac{1}{2} \sin\frac{\theta}{2} - \sum_{l=1}^{L} \frac{P_l(\cos\theta)}{(2l+3)(2l-1)} \right].$$

In equation (3.6) δ_l are the "phase shifts" of the partial waves and are the parameters that are varied in the fit, k is the wavenumber of the free electron, P_l are the Legendre polynomials, α is the dipole polarisability of the target molecule, (for water we have used the value $9.82{a_0}^3$, [85]) and a_0 is the Bohr radius. $C_L(\theta)$ is the contribution to the scattering amplitude from the higher partial waves, l (l > L), and it represents the Born approximation contribution to the scattering amplitude.

The program PSA is implemented by first estimating initial values for the partial waves, and then allowing the code to run for a finite time period until a set of new, hopefully improved "phase shifts" are achieved. These new "phase shifts" then become the initial inputs for a new run, a process which is repeated until convergence with a good fit to the DCS is obtained. It is possible that the MPSA technique will give an unphysical fit, particularly in the backward angle range where no measured data are available. Bottema [85] introduced some additional algorithms to help constrain the fit so that unphysical solutions are avoided, but in some cases problems still persist. More details on the MPSA can be found in Campbell *et al* [67], to which the reader is referred. Note that with the present experimental data all largely being strongly peaked at forward scattering angles, even with the $\sin\theta$ weighting in equation (3.5) the major contribution to

the integrand will come from angular regions where data have been measured. As a consequence our ICS derived using the MPSA should be physical, subject to the caveat given below.

It should be noted that the effectiveness of the MPSA technique for extrapolating the DCSs to 0°, in the water molecule is believed to be further limited by its large dipole moment. This has been outlined by both Baluja *et al* [86] and Faure *et al* [24], with their argument largely based on the observation that the elastic ICS of Cho *et al* [23] is somewhat lower (≈30%) than the value calculated by Faure *et al* [24] at the energy where the two studies overlap (4eV). This is in spite of the fact that the elastic DCS measured by Cho *et al* is in very good agreement with that calculated by Faure *et al.* As the ICS of Cho *et al* were determined using the MPSA technique, Faure *et al* [24] believe that it is not able to account for the extent of this forward peaking due to the large permanent dipole moment of water. While the results of Faure *et al* [24] and Baluja *et al* [86] pertain to the elastic channel, if they were to be generalised to the ICS for electronic-state excitation then it might mean that our MPSA estimated ICS should also be increased by up to 30% in some cases. This point will be looked at again in more detail when we come to discuss out results for the excitation of the important $\tilde{A}^1\mathrm{B}_1$ electronic-state.

Chapter 4

Results and Discussion

4.1 Preamble

We present here the first ever experimentally determined absolute cross sections for electron impact excitation of the electronic states in H_2O, to 12eV excitation energy. There was little previous work for us to compare our results with, hence, as a cross check for our work, independent DCS measurements were also made at Sophia University although over a much more limited kinematic range. Only a few theoretical studies had also previously published values for some of these cross sections (Pritchard *et al* [31], Gil *et al* [32], Lee *et al* [33], Morgan [34] and Gorfinkiel *et al* [35]). These previous studies covered excitation from the two highest occupied orbitals to the lowest unoccupied orbital, and one study (Lee *et al*) included a higher energy-loss transition as well. The complicated spectroscopy of the electronic states of H_2O, as discussed in Chapter 2, as well as the problems that H_2O can create in a vacuum system, are potential reasons for the lack of previous experimental studies. H_2O also presents problems to theorists because of its relatively high dipole moment and the Rydberg-valence nature of some of its electronic excited states.

In section 4.2 we present DCSs for the excited electronic states of H_2O and in

section 4.3 we present their corresponding ICS values, in both cases comparison is made, where possible, to the available theory. However, as the present study determined cross sections for a large number of electronic states we usually restrict our specific discussion in sections 4.2 and 4.3 to those states where a comparison to other works is available. In essence, this criterion limits our discussion to the first six excited electronic states of H_2O. Cross sections for the remaining states, which are potentially very important for atmospheric modelling and the modelling of radiation damage in matter (see for example Muñoz *et al* [7]), are summarised in appendices A and B.

4.2 Differential Cross Sections

We have determined absolute DCSs for each of the 25 features fitted to our EELS, as described in Chapter 3.3. Of the six previous studies to report cross sections for electronic state excitations in H_2O, the only ones to have published DCSs were Pritchard *et al* [31], Gil *et al* [32] and Lee *et al* [33]. Pritchard *et al* [31] used a Schwinger multichannel method to determine DCSs for the $\tilde{b}^3A_1$ state of H_2O at incident electron energies of 12, 15 and 20eV, while Gil *et al* [32] used a close-coupling complex Kohn calculation to determine DCSs for the $\tilde{a}, \tilde{A}\ ^{3,1}B_1$ and $\tilde{b}, \tilde{B}\ ^{3,1}A_1$ excited states for 12, 14, 16, 18 and 20eV incident electron energies. Note that in the discussion that follows we have compared our 15eV results to their 16eV DCSs. Finally, Lee *et al* [33] used the distorted-wave Born approximation to calculate DCSs for the $\tilde{b}^3A_1$ and $3a_1 \rightarrow 3pa_1\ ^3A_1$ excitations at energies between 12 and 150eV.

As a cross check of our work, some independent cross sections were measured by the group of Professor Hiroshi Tanaka at Sophia University in Japan. Their apparatus was similar to ours, in that it was a crossed beam electron spectrometer with hemispherical monochromators. Their angular resolution was $\pm 1^\circ$ and their energy resolution was 30 - 35meV FWHM. The EELS they measured were

deconvoluted at Flinders University using the same technique that we employed on our spectra (see Chapter 3.2). Cross sections were also determined from these spectra by the same method used with our data; taking the ratio of the area for the feature of interest to the area of the elastic feature and then multiplying by the relevant absolute elastic DCS from Cho *et al* [23]. The aim of this cross check was to seek to confirm the magnitude of our excited electronic state cross sections, and hence it was necessary to normalise the data with the same elastic differential cross sections. We therefore have data from Sophia University for transitions to approximately 11eV energy loss at 50eV and 10°, and for transitions to the $\tilde{a}^3B_1$ and $\tilde{A}^1B_1$ states at 30eV, 10° and 20° and at 15eV, 20eV and 40eV, for the scattering angle of 10°. The estimated uncertainty in the Sophia University data was ≈31%, this is inclusive of the uncertainty for the spectral deconvolution.

The major and most variable contribution to the uncertainty in our data, was from the standard deviation between results from measurements made under the same kinematical conditions (at least two and often three runs were made for each E_0, θ). Other contributions were from the uncertainty in the elastic cross sections of Cho *et al* [23], which were typically 10% or less; our calibration to ensure that the transmission function of the analyser was constant across the range of the energy loss spectra, estimated as 15% at best; and the statistical error in the build up of the spectra, estimated as 2%.

The first and second excited electronic states of H_2O result from the $1b_1 \rightarrow 3sa_1$ $\tilde{a}^3B_1$ and $\tilde{A}^1B_1$ transitions, with vertical excitation energies of 7.14eV and 7.49eV, respectively. The DCSs for these states are listed in table 4.1 and plotted in figures 4.1 and 4.2, respectively, for all the energies we studied (15eV to 50eV). These figures also include the calculated cross sections from Gil *et al* [32] at incident electron energies of 16eV and 20eV, and the corresponding cross sections from Sophia University at incident electron energies of 20eV to 50eV. In the EELS the features from these transitions were quite diffuse and somewhat overlapping with each other, they were also asymmetric in profile and thus, as noted previously, required two Gaussian functions to fit them effectively.

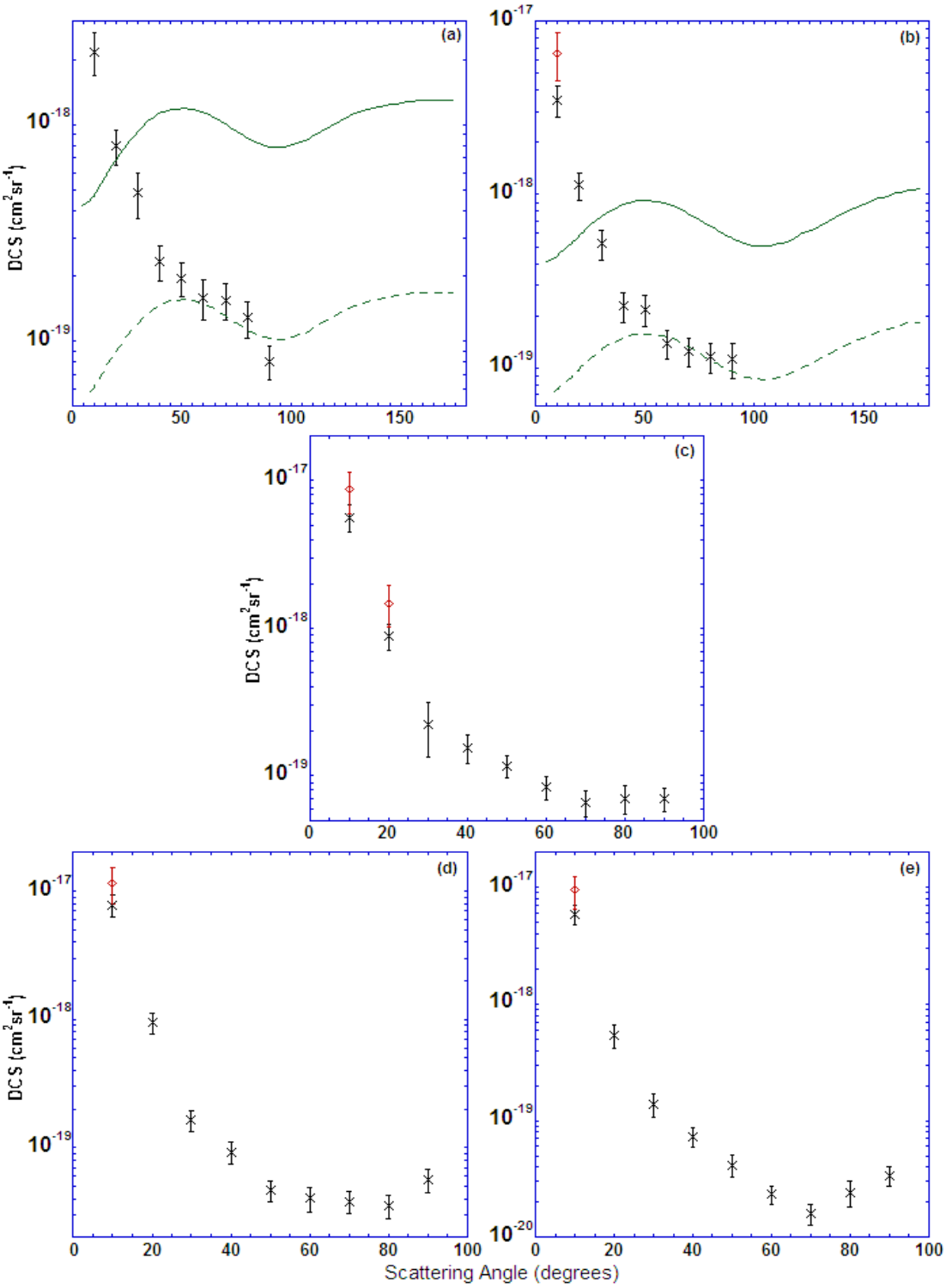

Figure 4.1: DCSs (cm^2sr^{-1}), as a function of electron scattering angle, for the $1b_1 \rightarrow 3sa_1$ $\tilde{a}^3B_1$ transition in H_2O at energies (a): E_0=15eV, (b): E_0=20eV, (c): E_0=30eV, (d): E_0=40eV and (e): E_0=50eV. (×) Present data, (◇) data from Sophia University, (—) Gil *et al* [32] 16eV calculation used in (a) and (- - -) Gil *et al* [32] calculation scaled by 0.13 and 0.17 in (a) and (b) respectively.

$\tilde{a}^3B_1$					
Angle	15eV	20eV	30eV	40eV	50eV
10°	21.7 (4.94)	35.21 (7.08)	56.54 (11.70)	77.49 (15.05)	59.31 (11.26)
20°	7.97 (1.49)	11.35 (2.04)	8.87 (1.81)	9.47 (1.72)	5.42 (1.22)
30°	4.82 (1.14)	5.22 (1.01)	2.24 (0.89)	1.63 (0.31)	1.39 (0.32)
40°	2.32 (0.43)	2.26 (0.43)	1.56 (0.35)	0.93 (0.19)	0.73 (0.14)
50°	1.96 (0.36)	2.16 (0.43)	1.17 (0.20)	0.46 (0.08)	0.42 (0.09)
60°	1.59 (0.34)	1.39 (0.26)	0.83 (0.15)	0.40 (0.08)	0.23 (0.04)
70°	1.54 (0.29)	1.25 (0.24)	0.66 (0.13)	0.38 (0.08)	0.16 (0.03)
80°	1.28 (0.24)	1.15 (0.23)	0.71 (0.15)	0.35 (0.07)	0.24 (0.06)
90°	0.81 (0.14)	1.13 (0.26)	0.70 (0.12)	0.56 (0.11)	0.34 (0.06)
$\tilde{A}^1B_1$					
10°	30.73 (6.59)	93.34 (19.56)	167.31 (34.66)	248.60 (52.68)	210.04 (40.04)
20°	12.35 (2.34)	31.59 (6.21)	27.18 (5.49)	31.35 (5.66)	15.98 (3.46)
30°	7.92 (2.35)	13.32 (2.47)	7.25 (1.43)	4.82 (0.90)	3.50 (0.69)
40°	3.41 (0.61)	5.02 (0.89)	3.51 (0.95)	2.03 (0.39)	1.83 (0.37)
50°	2.26 (0.42)	3.44 (0.63)	2.29 (0.39)	1.12 (0.20)	0.92 (0.17)
60°	1.62 (0.35)	2.04 (0.38)	1.32 (0.24)	0.85 (0.15)	0.55 (0.19)
70°	1.35 (0.25)	1.63 (0.31)	1.06 (0.20)	0.75 (0.16)	0.45 (0.11)
80°	1.07 (0.19)	1.55 (0.29)	0.96 (0.26)	0.62 (0.13)	0.37 (0.08)
90°	0.67 (0.13)	1.48 (0.31)	0.95 (0.17)	0.73 (0.15)	0.44 (0.10)

Table 4.1: DCSs ($\times 10^{-19}$cm^2/sr) as a function of electron scattering angle for the $1b_1 \rightarrow 3sa_1$ $\tilde{a}^3B_1$ and $\tilde{A}^1B_1$ transitions in H_2O. Values in brackets are the absolute error ($\times 10^{-19}$cm^2/sr).

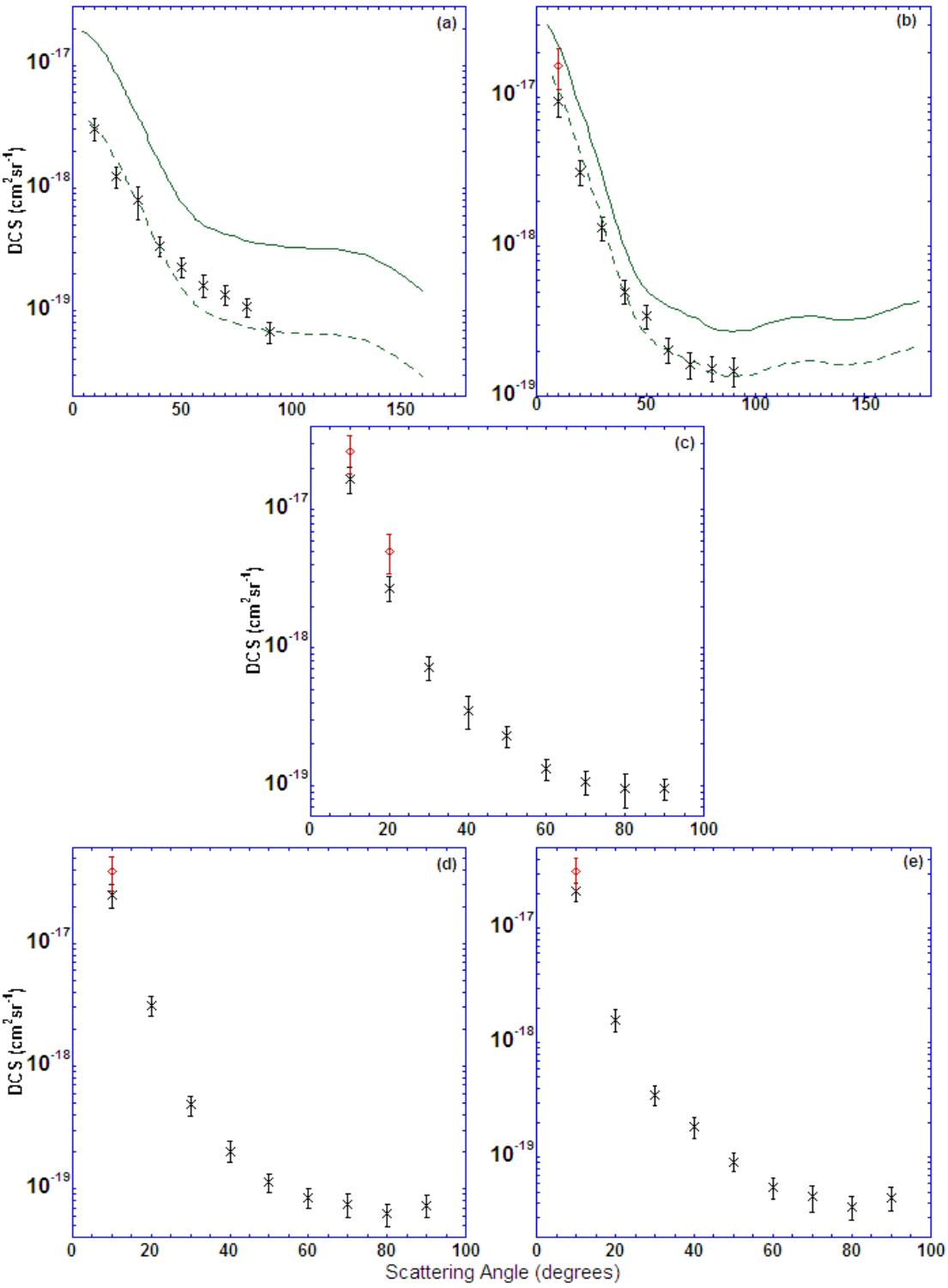

Figure 4.2: DCSs (cm^2sr^{-1}), as a function of electron scattering angle, for the $1b_1 \rightarrow 3sa_1$ $\tilde{A}^1B_1$ transition in H_2O. Labels and markers are as in figure 4.1, with Gil *et al* [32] now scaled by 0.2 and 0.5 in (a) and (b) respectively.

The spectral features resulting from the $3a_1 \rightarrow 3sa_1$ $\tilde{b}^3A_1$ and $\tilde{B}^1A_1$ transitions were found in our energy loss spectra at 9.46eV and 9.73eV respectively. These features were overlapped on both sides by features from other transitions, and were quite broad, although not as broad as the $\tilde{a}, \tilde{A}\,^{3,1}B_1$ transitions just discussed. These features were also not as asymmetric as those for the $\tilde{a}, \tilde{A}\,^{3,1}B_1$ states and hence only one Gaussian function was employed to fit them. The excitation of the $\tilde{b}^3A_1$ state has received the most attention from theorists. Our results along with the results of calculations from Pritchard *et al* [31], Gil *et al* [32] and Lee *et al* [33], and the experiment from Sophia University, are therefore plotted in figure 4.3 and the DCSs we have measured for the $\tilde{b}^3A_1$ state are tabulated in table 4.2. The present DCSs for the $\tilde{B}^1A_1$ state are also listed in table 4.2 and plotted, along with the calculated cross sections from Gil *et al* and those measured at Sophia University, in figure 4.4.

The main feature of the present DCSs, for all the states, was their rather forward peaked angular distribution and as can be seen in figures 4.1 to 4.4, the degree of this forward "peakedness" increased with incident electron energy. This behaviour is not expected for dipole forbidden transitions such as the $\tilde{a}^3B_1$ and $\tilde{b}^3A_1$ states, as it is generally accepted that the main population method for these states is electron exchange which typically does not lead to a forward peaked cross section. On the other hand, for the dipole allowed $\tilde{A}^1B_1$ and $\tilde{B}^1A_1$ states the observed forward peaking in the magnitude of the DCSs was anticipated. This assertion is clearly supported by the calculations.

Consider now, for example, the complex Kohn calculation of Gil *et al* [32] for the $\tilde{a}^3B_1$ state. As shown in figures 4.1(a) and (b) Gil *et al* find good shape agreement with our results above $\theta \approx 40°$, but did not reproduce the more forward angle behaviour seen in the present results. Contrary to this, for the $\tilde{A}^1B_1$ state, the calculated cross sections from Gil *et al* [32] were in excellent shape agreement with our experimental values. As shown in figures 4.2(a) and (b), when a scaling factor was applied to the complex Kohn DCS, excellent agreement was found between the measured and calculated values across the entire applicable (10° to

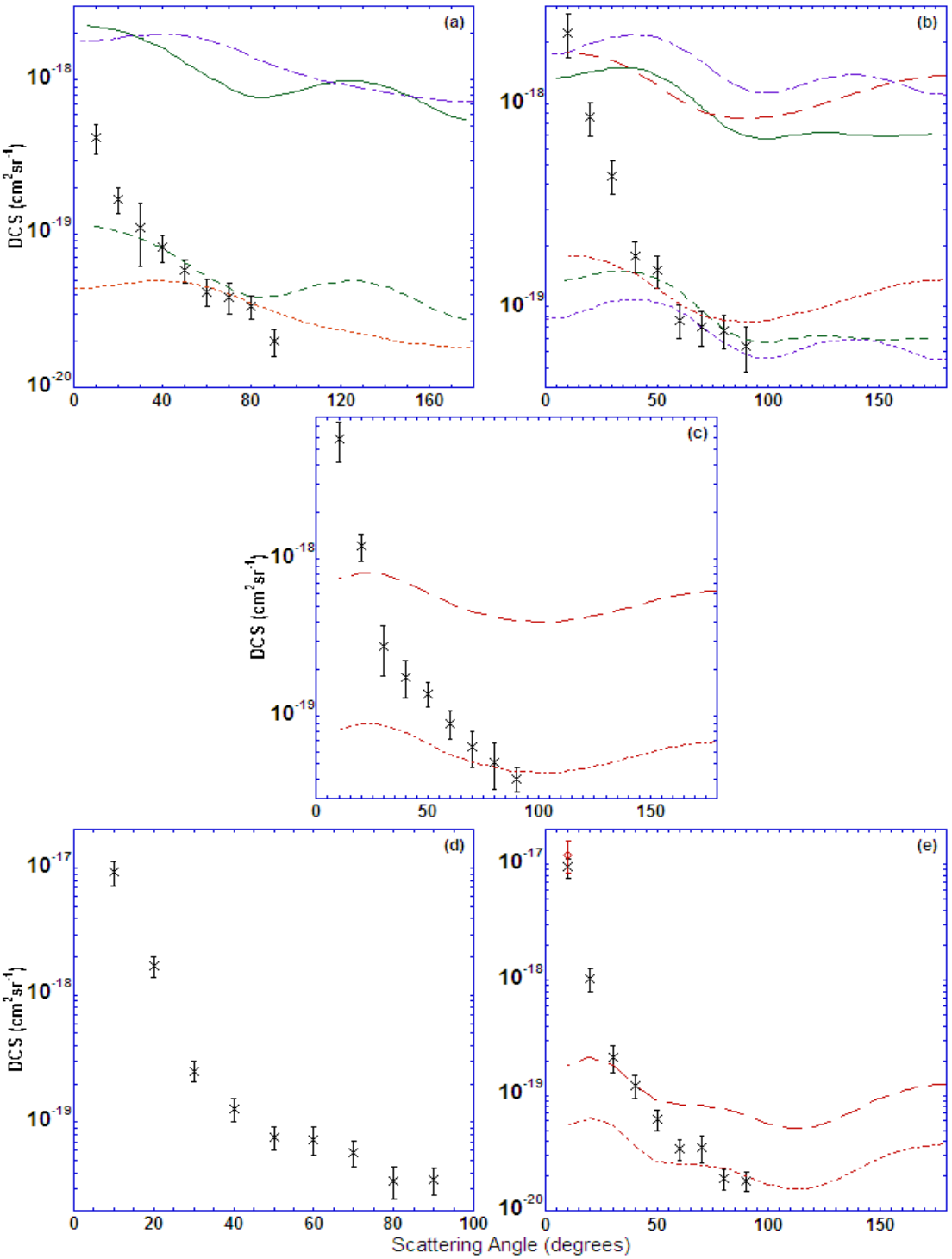

Figure 4.3: DCSs (cm^2sr^{-1}), as a function of electron scattering angle, for the $3a_1 \rightarrow 3sa_1$ $\tilde{b}^3A_1$ transition in H_2O. Labels and markers are as in figure 4.1, with Gil *et al* [32] now scaled by 0.05 and 0.1 in (a) and (b) respectively. In addition, (· – · –) is the calculation from Pritchard *et al* [31], (· · ·) Pritchard *et al* scaled by 0.03 and 0.05 in (a) and (b) respectively, (— — —) is the calculation from Lee *et al* [33], (· - · -) Lee *et al* scaled by 0.1, 0.11 and 0.3 in (a), (b) and (c) respectively.

			$\tilde{b}^3A_1$		
Angle	15eV	20eV	30eV	40eV	50eV
10°	4.20 (0.89)	22.17 (5.27)	58.10 (16.78)	92.37 (19.44)	94.59 (18.01)
20°	1.67 (0.32)	8.53 (1.60)	12.13 (2.42)	16.78 (3.02)	10.24 (2.29)
30°	1.09 (0.48)	4.40 (0.83)	2.81 (1.00)	2.53 (0.47)	2.12 (0.54)
40°	0.82 (0.16)	1.77 (0.31)	1.79 (0.47)	1.26 (0.25)	1.21 (0.27)
50°	0.58 (0.10)	1.51 (0.27)	1.39 (0.25)	0.77 (0.16)	0.62 (0.12)
60°	0.42 (0.08)	0.86 (0.16)	0.90 (0.18)	0.73 (0.19)	0.34 (0.07)
70°	0.39 (0.09)	0.79 (0.16)	0.64 (0.16)	0.58 (0.13)	0.35 (0.09)
80°	0.34 (0.06)	0.77 (0.14)	0.51 (0.17)	0.35 (0.10)	0.19 (0.04)
90°	0.20 (0.04)	0.64 (0.16)	0.40 (0.07)	0.35 (0.84)	0.18 (0.04)
			$\tilde{B}^1A_1$		
10°	3.72 (0.87)	17.13 (3.54)	40.64 (15.07)	71.85 (16.22)	72.84 (14.87)
20°	1.55 (0.29)	7.03 (1.76)	8.16 (2.24)	12.96 (2.49)	7.17 (1.82)
30°	0.60 (0.47)	3.40 (0.67)	2.22 (0.45)	2.44 (0.47)	2.07 (0.60)
40°	0.52 (0.13)	1.19 (0.29)	0.69 (0.12)	1.14 (0.22)	1.02 (0.20)
50°	0.33 (0.09)	0.79 (0.18)	0.62 (0.29)	0.76 (0.17)	0.64 (0.16)
60°	0.30 (0.06)	0.51 (0.10)	0.66 (0.13)	0.63 (0.12)	0.38 (0.07)
70°	0.30 (0.06)	0.56 (0.11)	0.60 (0.16)	0.50 (0.10)	0.25 (0.06)
80°	0.22 (0.05)	0.47 (0.09)	0.48 (0.14)	0.37 (0.09)	0.23 (0.07)
90°	0.13 (0.04)	0.50 (0.10)	0.60 (0.23)	0.43 (0.10)	0.23 (0.05)

Table 4.2: DCSs ($\times 10^{-19}$cm^2/sr) as a function of electron scattering angle for the $3a_1 \rightarrow 3sa_1$ $\tilde{b}^3A_1$ and $\tilde{B}^1A_1$ transitions in H_2O. Values in brackets are the absolute error ($\times 10^{-19}$cm^2/sr).

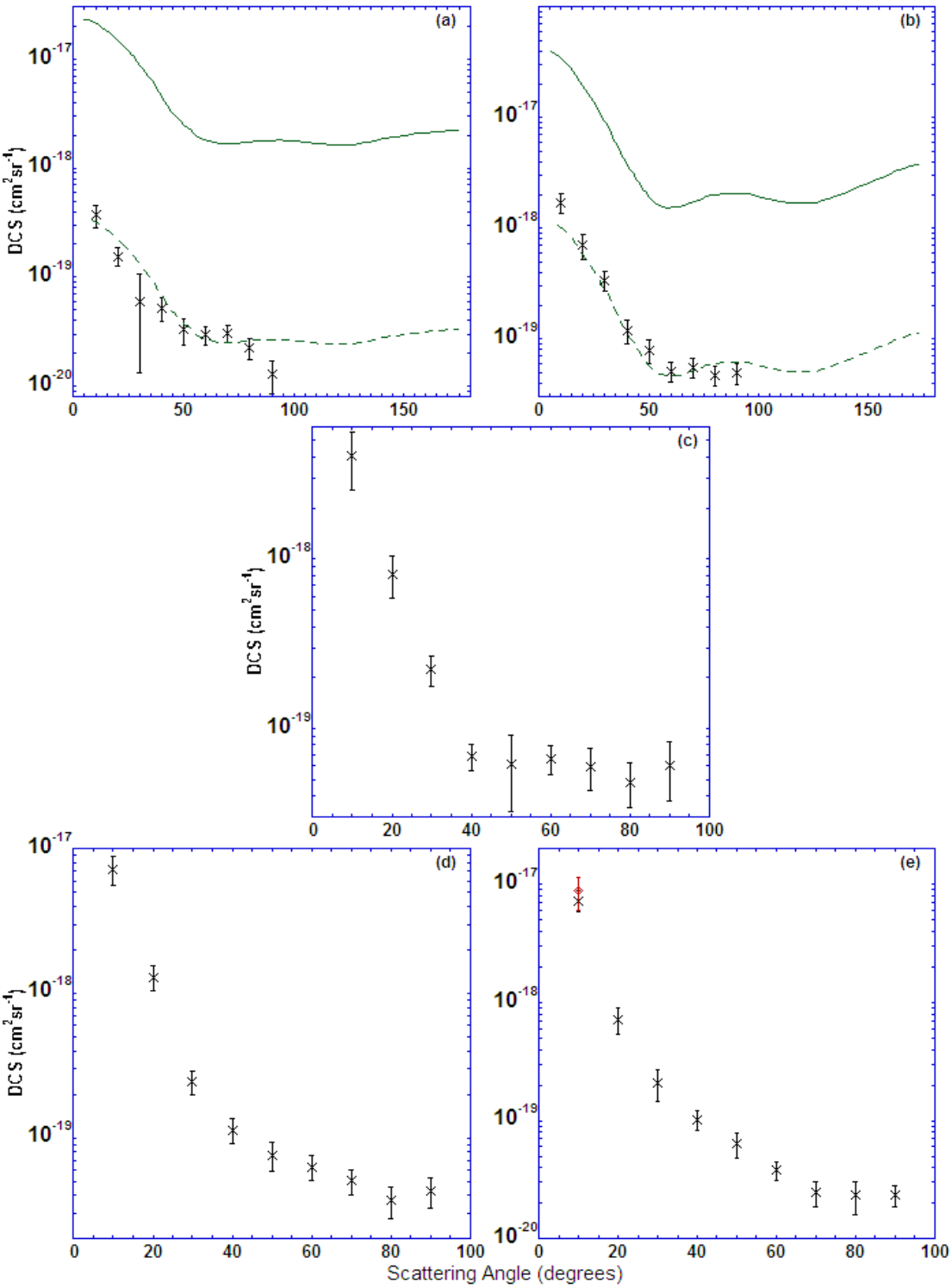

Figure 4.4: DCSs (cm^2sr^{-1}), as a function of electron scattering angle, for the $3a_1 \rightarrow 3sa_1$ $\tilde{B}^1A_1$ transition in H_2O. Labels and markers are as in figure 4.1, with Gil *et al* [32] now scaled by 0.015 and 0.03 in (a) and (b) respectively.

90°) angular range. In our spectral deconvolution process we were very careful to try and remove the possibility of any contamination from overlapping singlet transitions to the triplet intensity, however it is possible that this was not completely successful. If this scenario were true then that could, at least in part, be the cause of the observed forward peaked structure in our triplet cross sections. The positions and widths of the $\tilde{a}^3B_1$ and $\tilde{A}^1B_1$ features were fixed based on the measurements of Jureta [21], Mota *et al* [22] and other spectroscopic studies as discussed previously in Chapter 2 and section 3.2. However as we noted in section 3.2, a study by Lewis *et al* [79] showed that the spectroscopy of states with highly mixed Rydberg-valence character, as was the case here, are highly dependent on the kinematical conditions. Since we fixed the positions and widths of these two features in our deconvolution process, for all kinematics, this may have been a source of uncertainty with our DCSs. This same argument is further applicable to the $\tilde{b}^3A_1$ and $\tilde{B}^1A_1$ states. Kim [87] has also suggested that the observed forward angle triplet behaviour might be explained by molecular rotation including a dipole contribution to the scattering mechanism, or some form of configuration mixing occurring is another possibility that was suggested by Rescigno [80].

It is clear from figures 4.1 to 4.4 that all the calculations overestimate the magnitude of the cross sections when compared to the present measurements. For example, as seen in figure 4.2, when the complex-Kohn cross sections of Gil *et al* [32] for the $\tilde{A}^1B_1$ state, are scaled by a factor of about 0.2 at 16eV and 0.5 at 20eV, the agreement with our data is quite good. Rescigno [80] noted that the discrepancies in the magnitudes of the calculated and measured cross sections could be due to the use of the fixed nuclei approximation by Gil *et al*. This suggestion was based on a previous scenario in H_2, where by accounting for nuclear motion with an adiabatic nuclei approximation Trevisan and Tennyson [88] found good agreement with the experimental results of Khakoo and Segura [89] while previous fixed nuclei approaches were ineffective. Rescigno [80] also suggested that the observed discrepancy might be due to the fact that the target wave functions used were possibly too simple. As this is a state with Rydberg-

valence character the target wave functions are difficult to characterise, and the complex Kohn method is very sensitive to the accuracy of the wave functions used. All these arguments are equally applicable to the $\tilde{a}^3B_1$, $\tilde{b}^3A_1$ and $\tilde{B}^1A_1$ states.

Comparison against the independent data measured at Sophia University serves to increase our confidence in the present results. As seen in figures 4.1 to 4.4 the agreement seen between the present DCSs and those from Sophia University at 10° for all states (and 20°, 30eV for the $\tilde{a}^3B_1$ and $\tilde{A}^1B_1$ states) is good. When the angular uncertainty of ±1° in both experiments was taken into account, then the agreement between both experiments was actually very good. This angular uncertainty in the experimental results could potentially have quite significant effects at forward angles, where the cross sections were steeply sloping. In particular we note the particularly good agreement in the cross sections at 10°, 50eV for the $\tilde{b}^3A_1$ and $\tilde{B}^1A_1$ states.

As seen in figure 4.3, Pritchard *et al* [31], Gil *et al* [32] and Lee *et al* all calculated DCSs for the $\tilde{b}^3A_1$ state and hence there is more data with which we can compare our results. Figures 4.3(a) and (b), for the DCSs at 15eV and 20eV, show that the shape agreement between theory and experiments was quite good above $\theta \approx 40°$, which was also seen for the $\tilde{a}^3B_1$ state. However for the $\tilde{b}^3A_1$ state the shape agreement below a scattering angle of 40° was better than was seen previously for the $\tilde{a}^3B_1$ transition, although still none of the calculations reproduced the forward peaking found in the present study. Whereas the DCSs calculated by Gil *et al* for the $\tilde{a}^3B_1$ transition increase fairly sharply from an absolute minimum at $\theta \approx 0°$ to a maximum at 40° (at both 16eV and 20eV), the calculated DCSs for the $\tilde{b}^3A_1$ transition do not follow that angular behaviour. In fact the cross sections from Gil *et al* at 16eV and Lee *et al* at 20eV seem to have a maximum at $\theta \approx 0°$, which is at least in some qualitative agreement with the present results. The cross sections from Lee *et al* [33] at 30eV and 50eV do not have particularly good shape agreement with the measured data over any significant angular range.

In general all the theoretical cross sections extensively overestimate the strength for the excitation of the $\tilde{b}^3A_1$ state (as they also do for the $\tilde{a}^3B_1$, $\tilde{A}^1B_1$ and $\tilde{B}^1A_1$ states). The exception to this trend was at 50eV, where the cross sections calculated by Lee *et al* [33] were in good agreement with the present results for 30° and 40°. The possible reasons for the magnitude and shape discrepancies seen between theory and experiment for this transition are again the same as those given earlier, specifically the simplicity of the target wave functions used and the neglect of nuclear motion. The scaling factors that were applied to the calculation by Gil *et al* [32], were marginally larger (i.e. less scaling) than those that were applied to the cross sections from Pritchard *et al* [31] and Lee *et al.* Gil *et al* employed five target states in their calculation, while Lee *et al* and Pritchard *et al* employed only two in theirs, and in each calculation the target state wave functions were obtained by a similar method. This suggests that even more states, as well as more accurate representations of them, would be required to significantly increase the accuracy of the available calculations.

For excitation of the $\tilde{B}^1A_1$ transition (and this also applies to the $\tilde{A}^1B_1$ state) the magnitude of the scaling factor applied to the calculated data is smaller at 15eV than at 20eV. As the target description is the same at both energies, this observation suggests that the Kohn variational method provides a better description of the excitation process at the higher energy. It is also of interest to compare the scaling factors applied to the $\tilde{A}^1B_1$ and $\tilde{B}^1A_1$ states, in order to bring theory and experiment into accord. These scaling factors were much larger for the $\tilde{A}^1B_1$ state than for the $\tilde{B}^1A_1$ state, at the common energy of 20eV they were 0.5 and 0.03 respectively (note that the same argument is also applicable to the 15eV data). In this case the scattering description is essentially the same at the common energy, so that the observed difference in the scaling factors implies a more physical description of the $\tilde{A}^1B_1$ state, compared to the $\tilde{B}^1A_1$ state, in the work of Gil *et al* [32].

As a cross check for their work Gil *et al* [32] attempted to calculate EELS from their computed DCSs using equation (4.1). They then compared their calculated

EELS results to the EELS measured by Trajmar *et al* [18] at 20eV, for the scattered electron angles of 10° and 40°.

$$I = \sum_i \sigma_i(E_0, \omega) \frac{W/\pi}{(E - E_i)^2 + W^2} \tag{4.1}$$

In equation (4.1) E_i is the excitation energy of the state i, as calculated in the CI method by Kaldor [43], $\sigma_i(E_0, \omega)$ is the DCS for state i, E is the observed electron energy loss, and $2W$ is the dissociative width, which has been approximated by Gil *et al* [32] as 0.8eV for each state. E_0 and ω are the incident electron energy and scattering angle respectively. Little could be said about the agreement in terms of the absolute magnitudes of the calculated and measured spectra, as the measured spectra were not on the absolute scale. Hence Gil *et al* normalised the spectra to each other at energy loss 7.4eV, θ=10°. Consequently the shapes and relative heights in the respective spectra are still of interest. From their comparison of the measured and calculated EELS it could be seen that at θ=10° the calculated spectra cut off the area of the measured EELS where the $\tilde{a}^3\mathrm{B}_1$ transition occurs. However at θ=40° this area of the measured spectra is well reproduced. This observation correlates with the disagreement in the angular distribution found between Gil *et al* and the present results for this transition. In addition, in the area of the 40° energy loss spectra corresponding to the $\tilde{b}^3\mathrm{A}_1$ and $\tilde{B}^1\mathrm{A}_1$ transitions, there was a significant magnitude discrepancy. Recall that this was not the case in the region of the $\tilde{a}^3\mathrm{B}_1$ and $\tilde{A}^1\mathrm{B}_1$ features. As I noted earlier only the relative magnitudes are relevant, so that from these latter observations we can conclude that there is either a significant overestimation in the calculated cross sections for the $\tilde{b}, \tilde{B}\ ^{3,1}\mathrm{A}_1$ states or a significant underestimation in the calculated cross sections for the $\tilde{a}, \tilde{A}\ ^{3,1}\mathrm{B}_1$ states (or an underestimate/overestimate in both, but one more so than the other). Indeed we found the strength of all the present differential cross sections for the $\tilde{a}, \tilde{A}\ ^{3,1}\mathrm{B}_1$ and $\tilde{b}, \tilde{B}\ ^{3,1}\mathrm{A}_1$ states to be overestimated by the calculations, but the $\tilde{b}, \tilde{B}\ ^{3,1}\mathrm{A}_1$ states were significantly more so. This magnitude discrepancy between the measured and calculated spectra is in fact even greater when it is taken into account that the calculated spectra does not

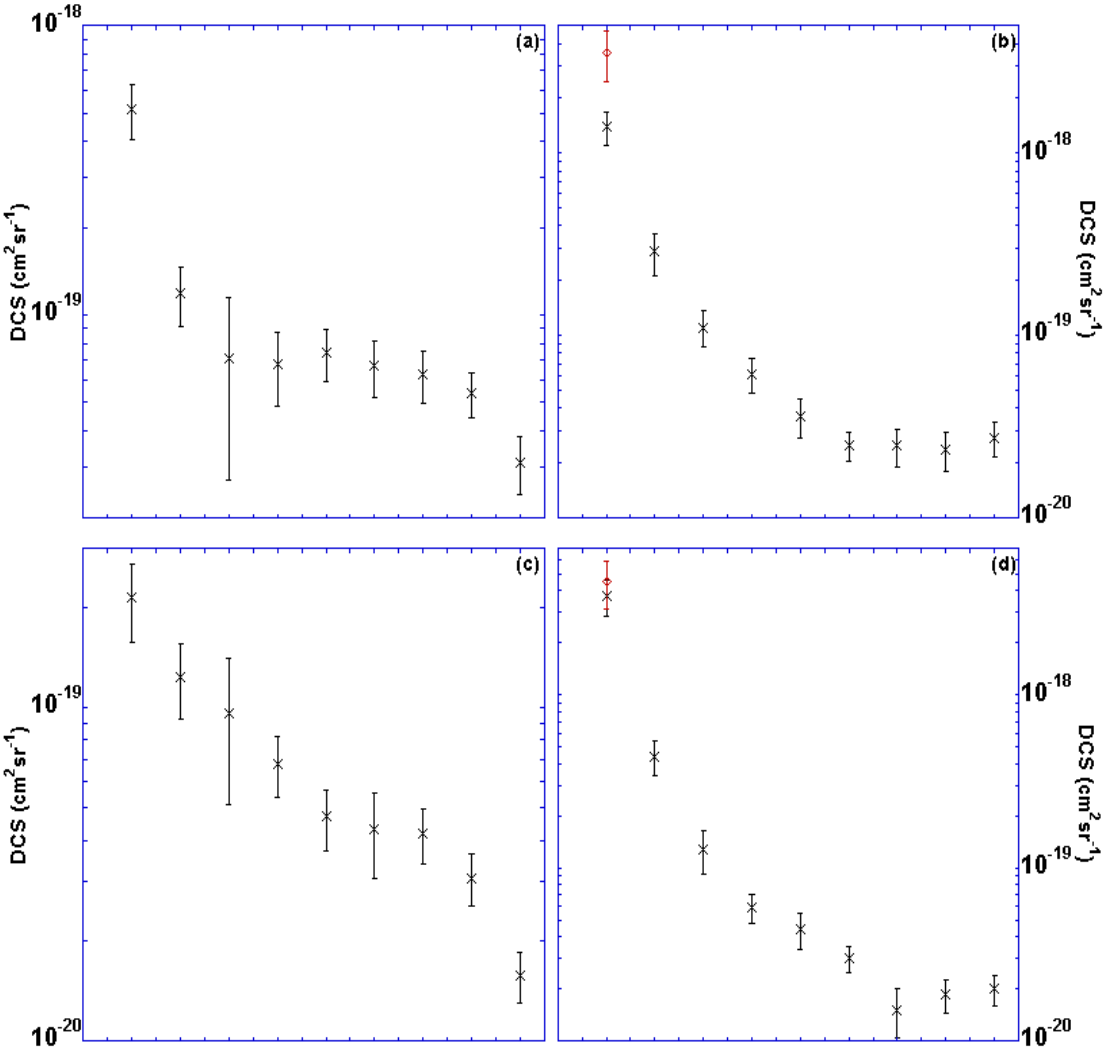

Figure 4.5: DCSs (cm^2sr^{-1}), as a function of electron scattering angle, for various transitions and energies in H_2O (a): $1b_1 \rightarrow 3pb_2$ $^3A_2$ at 15eV, (b): 50eV, (c): $1b_1 \rightarrow 3pb_2$ $^1A_2$ at 15eV, (d): 50eV. (×)Present data, (◇) Sophia University.

include the $^3A_2$ and $^1A_2$ features, which should occur in about the same energy loss region as the $\tilde{b}, \tilde{B}$ $^{3,1}A_1$ states.

The third and fourth features in the energy loss spectra measured in the present study were due to the $1b_1 \rightarrow 3pb_2$ $^3A_2$ and $^1A_2$ transitions respectively, and their corresponding DCSs are shown in figure 4.5 and table 4.3. These transitions occur at excitation energies 8.90eV and 9.20eV respectively, which locates them in the EELS between the $\tilde{A}^1B_1$ and $\tilde{b}^3A_1$ excitations. Both these transitions have less overlapping features than most of the remaining states in the EELS, which

[1] $^3A_2$					
Angle	15eV	20eV	30eV	40eV	50eV
10°	5.16 (1.11)	10.06 (2.42)	29.35 (7.64)	18.24 (4.41)	13.86 (2.85)
20°	1.19 (0.27)	3.47 (0.77)	5.62 (2.40)	4.67 (0.85)	2.88 (0.75)
30°	0.71 (0.44)	3.70 (0.69)	1.55 (0.42)	1.30 (0.24)	1.11 (0.25)
40°	0.68 (0.20)	1.98 (0.35)	1.54 (0.56)	0.78 (0.20)	0.61 (0.13)
50°	0.74 (0.15)	1.66 (0.36)	1.06 (0.20)	0.53 (0.14)	0.36 (0.09)
60°	0.67 (0.14)	1.05 (0.20)	0.68 (0.13)	0.44 (0.08)	0.25 (0.04)
70°	0.63 (0.13)	0.90 (0.17)	0.53 (0.10)	0.41 (0.09)	0.25 (0.06)
80°	0.54 (0.09)	0.87 (0.16)	0.55 (0.15)	0.37 (0.07)	0.24 (0.06)
90°	0.31 (0.07)	0.83 (0.18)	0.53 (0.10)	0.50 (0.10)	0.28 (0.06)
[1] $^1A_2$					
10°	2.14 (0.56)	10.67 (3.40)	5.63 (1.05)	40.49 (8.03)	37.31 (8.90)
20°	1.24 (0.31)	5.26 (1.05)	3.24 (2.98)	7.98 (1.46)	4.42 (1.02)
30°	0.96 (0.45)	2.69 (0.53)	0.41 (0.19)	1.48 (0.31)	1.28 (0.36)
40°	0.68 (0.14)	1.26 (0.23)	0.78 (0.14)	0.61 (0.14)	0.59 (0.11)
50°	0.47 (0.10)	0.85 (0.16)	0.59 (0.10)	0.40 (0.09)	0.44 (0.11)
60°	0.43 (0.12)	0.50 (0.12)	0.48 (0.10)	0.34 (0.11)	0.30 (0.05)
70°	0.42 (0.08)	0.46 (0.10)	0.40 (0.12)	0.31 (0.06)	0.15 (0.05)
80°	0.31 (0.05)	0.40 (0.08)	0.34 (0.13)	0.35 (0.06)	0.19 (0.04)
90°	0.16 (0.03)	0.50 (0.11)	0.52 (0.15)	0.31 (0.08)	0.20 (0.04)

Table 4.3: DCSs ($\times 10^{-19}$cm^2/sr) as a function of electron scattering angle for the $^3A_2$ and $^1A_2$ electronic states in water. Values in brackets are the absolute error ($\times 10^{-19}$cm^2/sr).

makes the unique determination of their differential cross sections somewhat less problematic. The only data against which we could compare the present DCSs were from Sophia University at 50eV, with which good agreement was found. It is worthy to note that for the $1b_1 \rightarrow 3pb_2$ $^3A_2$ transition at 15eV incident energy (figure 4.5.(a)) the differential cross section is much less forward peaked than that for the corresponding singlet transition, in fact the $^3A_2$ DCS is remarkably flat until θ=20°. This sharp forward peaking at only θ=10° may thus be indicative of some contamination from its neighbouring singlet transition in our spectral deconvolution.

4.3 Integral Cross Sections

The DCS data presented in section 4.2 were used to determine ICS values in the manner described in section 3.4. Where possible these experimental ICSs are now compared to the results of previous theoretical studies, including those from Pritchard *et al* [31], Gil *et al* [32] and Lee *et al* [33]. In addition there have also been calculations by Morgan [34], who utilised a FN R-matrix approach, and Gorfinkiel *et al* [35] who utilised an AN R-matrix approach. These R-matrix calculations ([34] and [35]) covered incident electron energies from threshold to 20eV and 15eV, respectively, and considered transitions to the $\tilde{a}^3B_1$, $\tilde{A}^1B_1$, $\tilde{b}^3A_1$, and $\tilde{B}^1A_1$ electronic states. ICSs were also calculated by Kim [36], for the $\tilde{A}^1B_1$ state, using a method known as the BE*f*-scaling approach. Agreement between the results from the various theories is actually quite poor, and as there have been no previous experimental studies on these ICSs we hope the present data will shed some light on that situation.

The overall uncertainty in our ICS values is generated through a combination of the uncertainty inherited from the present DCS data and an uncertainty in our application of the MPSA code relating to the extrapolation and integration program. We estimate the uncertainty from our numerical integration code to be better than 1%. Since the majority of our DCS results are strongly peaked in the forward angles, the main contribution to the ICSs comes from DCSs at scattered electron angles lower than 40°. Hence the contribution to the uncertainty in our ICSs from the DCSs, was determined by averaging the uncertainties in our DCSs over the range θ=10° to θ=40°. The sensitivity of the final ICS value to the extrapolation procedure was tested by making several fits with different added DCS end points at 0° and 180°, with the standard deviation of the ICS determined from these different extrapolations being included in the overall uncertainty. The typical overall uncertainty in the ICS values for most transitions and energies was between ≈25% and ≈40%. As was previously mentioned in section 3.4, the extrapolation technique (MPSA) can sometimes produce an unphysical result.

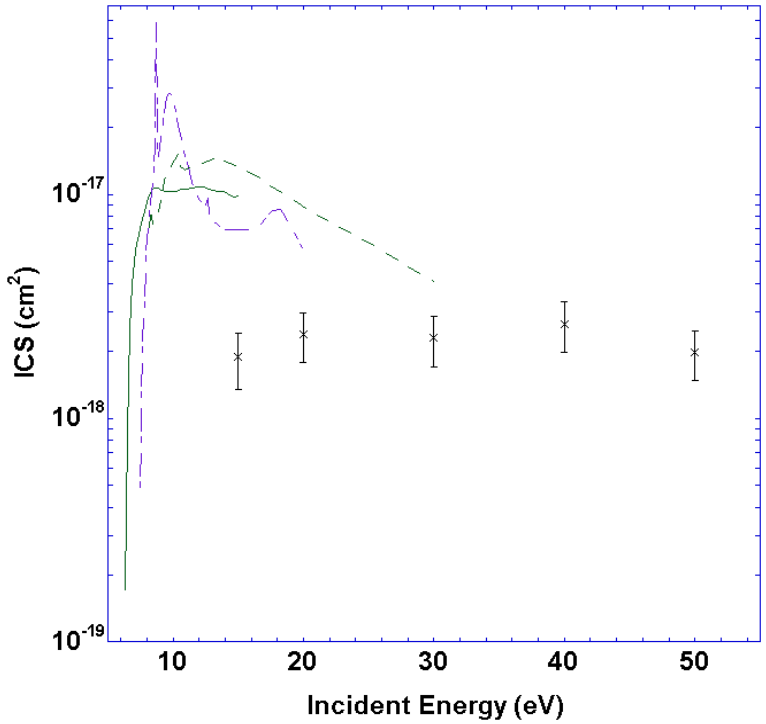

Figure 4.6: Present ICS (cm^2) for the $1b_1 \rightarrow 3sa_1$ $\tilde{a}^3B_1$ transition in H_2O. Results are from (×): present study,(– – –): Gil *et al* triplet coupled target state (TC) [32],(- — - —): Morgan [34], and (——): Gorfinkiel *et al* [35].

In order to reduce any occurrence of these unphysical results the fit could be constrained using an approach suggested by Bottema [85]. On application of this approach any oscillating behaviour in the fit was usually found to disappear.

The present ICSs for the $\tilde{a}^3B_1$ state are shown in figure 4.6 and listed in table 4.4. Also plotted in this figure are the results from the theoretical studies of Gil *et al* [32], Morgan [34] and Gorfinkiel *et al* [35]. Clearly there is a significant magnitude disagreement between all the calculations and the present results. Indeed our measured cross sections are approximately 5 times smaller than the calculated cross sections from Gil *et al* [32], Morgan [34] and Gorfinkiel *et al* [35] at incident electron energies of 15eV and 20eV.

Possible reasons for these discrepancies are similar to those already given in the previous section for our discussion of the DCS results. Rescigno [80] pointed out that the accuracy of the complex Kohn calculation from Gil *et al* [32] was very sensitive to the target wave functions used, so that it might be significantly

State	ICS ($\times 10^{-19}$ cm^2)				
	15eV	20eV	30eV	40eV	50eV
$\tilde{a}^3B_1$	20.89 (5.22)	23.71 (5.93)	22.78 (5.90)	26.40 (6.60)	19.66 (4.92)
$\tilde{A}^1B_1$	25.90 (6.48)	55.44 (13.86)	67.13 (16.78)	77.00 (19.25)	63.49 (15.87)
$^3A_2$	5.58 (2.11)	13.01 (3.64)	15.15 (5.04)	10.79 (3.02)	6.94 (1.94)
$^1A_2$	6.17 (3.08)	12.01 (3.36)	7.76 (3.41)	14.55 (4.07)	12.64 (3.54)
$\tilde{b}^3A_1$	4.87 (1.36)	14.76 (4.13)	23.92 (6.70)	32.80 (9.18)	29.27 (8.20)
$\tilde{B}^1A_1$	3.74 (1.36)	13.37 (3.74)	16.89 (4.73)	25.37 (7.10)	22.56 (6.32)

Table 4.4: Absolute ICS values ($\times 10^{-19}$ cm^2) for the first six excited electronic states of H_2O. Values in parentheses are corresponding absolute uncertainties ($\times 10^{-19}$ cm^2).

improved by the use of more states in the expansion and/or more sophisticated wave functions. Similarly, both the R-matrix calculations ([34] and [35]) might possibly benefit from an improved target state representation, although they did both use more target states (seven) than other previous calculations ([31] - [33]). However, an accurate representation of diffuse target-state wave functions is somewhat limited in the R-matrix method. This follows as representation of states with Rydberg character, like the $\tilde{a}^3B_1$, $\tilde{A}^1B_1$, $\tilde{d}^3A_1$ and $\tilde{B}^1A_1$ states (four of the seven states included in the R-matrix calculations of both Morgan [34] and Gorfinkiel *et al* [35]), would require the use of quite a large R-matrix box. This in turn might render the calculation to be practically impossible. The methods used by Morgan and Gil *et al* were carried out at the FN equilibrium geometry of the molecule and this also may effect the accuracy of their calculations. The AN R-matrix calculation from Gorfinkiel *et al* [35] also overestimates our measured values, and we cannot discount inappropriate treatment of nuclear motion as a possible source of inaccuracy in that calculation as well. As Gorfinkiel *et al* suggested, the use of a one-dimensional model in their treatment of nuclear motion (instead of a full three dimensional model), might have been insufficient to account for all possible channels of excitation/dissociation and hence could have led to an artificial increase in their calculated cross sections.

We could not compare the shape of the present cross section to that calculated by Gorfinkiel *et al* [35], as the two data sets overlap at only one point (15eV

incident electron energy). However we can compare the general trend of the energy distribution of the present study to that from Gil *et al* [32], and Morgan [34], to incident energies of 30eV and 20eV, respectively. The present $\tilde{a}^3B_1$ cross section was generally quite isotropic over the energy range measured although there is a suggestion that at 15eV it is starting to decrease towards its threshold. On the other hand the cross section from Gil *et al* clearly peaked in magnitude at ≈15eV. Morgan's cross section features a shape resonance at an incident electron energy of about 18eV, which was assigned to a $^2A_1$ symmetry, and it is also seen in the ICS for the $\tilde{b}^3A_1$ and $\tilde{B}^1A_1$ states. The present ICSs, for all these states, found no conclusive evidence in support of, or against, the existence of a resonance at 18eV. This observation might essentially be due to the size of the energy step between the present measurements and because no specific measurement was made at 18eV.

The integral cross sections we determined for the $\tilde{b}^3A_1$ state are plotted in figure 4.7 and listed in table 4.4. This figure also includes the results of available theories from Pritchard *et al* [31], Lee *et al* [33], Gil *et al* [32], Morgan [34] and Gorfinkiel *et al* [35]. For incident electron energies below 30eV all these theories overestimated our results. Specifically at 15eV the calculated cross sections were, on average, ≈30 times greater than the present results. The calculation from Lee *et al* [33] was the only one to consider incident electron energies greater than 30eV. At ≈35eV incident electron energy their cross section started to underestimate the present results and by 50eV their cross section was ≈3 times smaller than ours. Possible reasons for the magnitude discrepancies between the theories and the present experiment, are the same as those discussed previously for the $\tilde{a}^3B_1$ state, and so we do not repeat them here. However we do note that for the $\tilde{b}^3A_1$ state the observed magnitude discrepancy, certainly for electron energies of 20eV and below, was greater than that seen for the $\tilde{a}^3B_1$ transition. The observed magnitude discrepancy was also not unexpected for the complex Kohn calculation of Gil *et al*, based on the results found for their DCSs. In particular we recall that the DCSs also showed a much greater magnitude discrepancy for the $\tilde{b}^3A_1$ and $\tilde{B}^1A_1$ states compared to that for the $\tilde{a}^3B_1$ and $\tilde{A}^1B_1$ states.

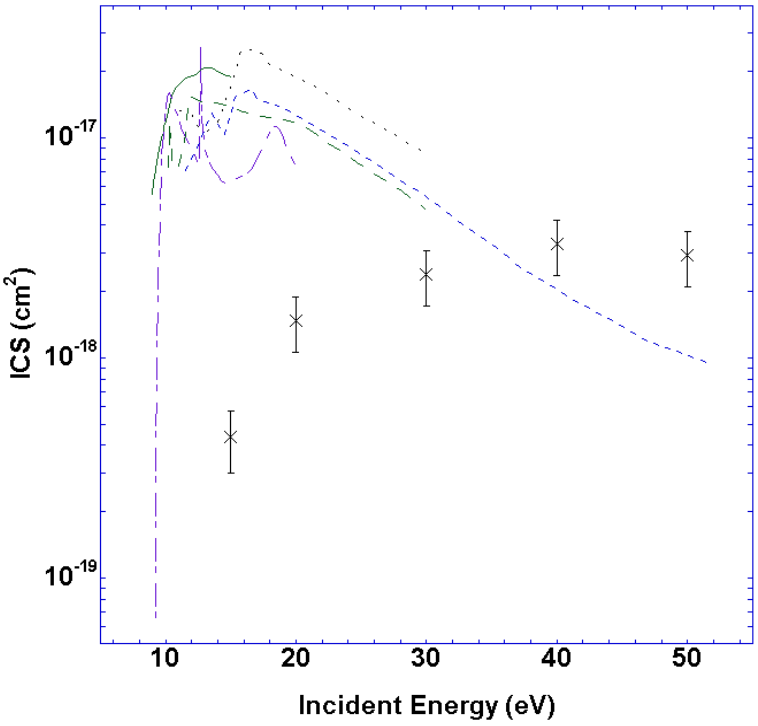

Figure 4.7: Present ICS (cm^2) for the $3a_1 \rightarrow 3sa_1$ $\tilde{b}^3A_1$ transition in H_2O. Results from the different studies are as represented in figure 4.6, with the addition of ($\cdot\ \cdot\ \cdot$): Pritchard *et al* [31], and (- - -): Lee *et al* [33].

The energy distribution of the ICSs for the $\tilde{b}^3A_1$ state was similar to that of the $\tilde{a}^3B_1$ transition, although the cross section falling off in magnitude at lower energies was more prevalent here and the distribution was less isotropic for this state compared to $\tilde{a}^3B_1$ transition. Again none of the available theories were able to reproduce the observed energy dependence of the experimental cross section. Pritchard *et al* [31] and Lee *et al* [33] found their calculated cross sections to peak at ≈16eV incident electron energy. The present measurements did not support this proposed peak in the energy distribution, as our cross sections were clearly increasing slowly (after 20eV) toward a peak at ≈40eV.

ICSs determined for the $\tilde{A}^1B_1$ state are listed in table 4.4 and plotted in figure 4.8 along with the available theory. For this transition the available theories were from Gil *et al* [32], Morgan [34], Gorfinkiel *et al* [35] and Kim [36]. It is interesting to note that for this excitation Gil *et al* [32] made two different calculations, one with their regular complex Kohn method, the same method used for

the triplet states already discussed (denoted TC), and another where they also employed a dipole-Born closure method (denoted TC-dipole-Born). Kim [36] performed a scaled plane-wave Born calculation (BEf-scaled) involving "f-scaling" and "BE-scaling". In f-scaling the Born integral cross section was scaled by the experimentally determined optical oscillator strength (OOS or f), to remove the effect of inaccurate wave functions. In "BE scaling" the Born cross section was further scaled by a function of the excitation energy, binding energy and incident electron energy. This had the effect of increasing the accuracy of the cross section at low incident energies. Needless to say when both the f-scaling and BE scaling are applied a so-called BEf-scaling result is obtained and it is this cross section that is included in the discussion that follows and in figure 4.8. The use of this BEf-scaled method for molecules is quite new but has also previously been used to calculate ICS for H_2 [90] and CO [91]. In both these previous applications the BEf-scaled result found good agreement with experimental results. Note, however, that both the BEf-scaled Born method of Kim [36] and the TC-dipole-Born closure method of Gil *et al* [32] are valid only for dipole allowed transitions.

The calculated cross sections for the $\tilde{A}^1B_1$ state all overestimate our measured values, more so at the lower energies than at the higher energies. At the incident electron energy of 15eV the calculated cross section from Gorfinkiel *et al* [35] is $\approx$10 times larger than the present result, while the calculation from Kim [36], which represents the best agreement with our results, is $\approx$3 times bigger. At higher energies, however, the magnitude agreement between the present ICS and all the calculated cross sections is much improved. At 40eV the calculation of Kim was actually within our plotted experimental uncertainty. The magnitude agreement between our data and that of the calculation from Kim is clearly the best of all the current calculations. In Thorn *et al* [36], Kim also, where possible, took the present data but replaced our 10° DCS point with the 10° data from Sophia University. While these points overlapped within their respective error bars, the Sophia DCS was always larger in magnitude. On applying his equivalent extrapolation procedure (to the MPSA), he derived new ICS for the A^1B_1 state

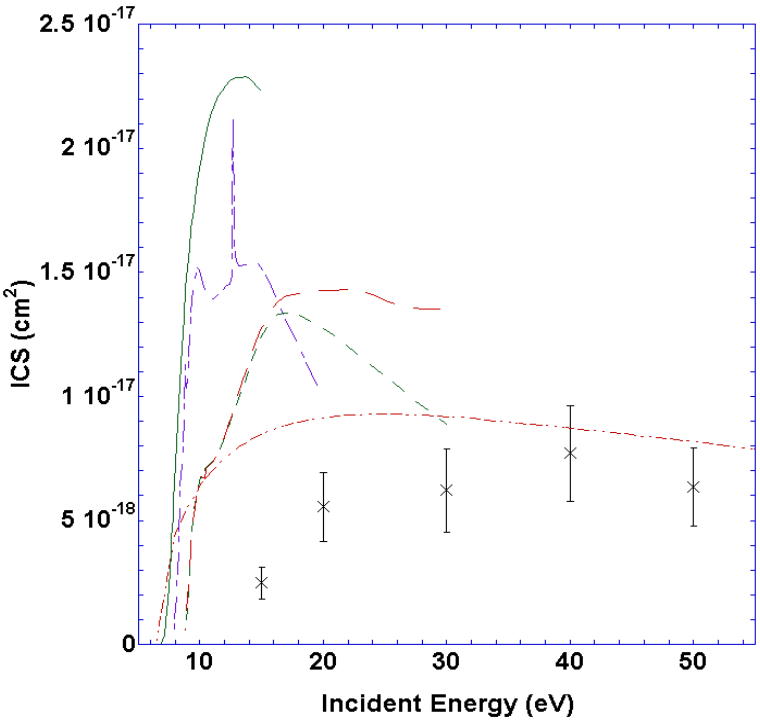

Figure 4.8: Present ICS (cm^2) for the $1b_1 \rightarrow 3sa_1$ $\tilde{A}^1B_1$ transition in H_2O. Results from the different studies are as represented in figure 4.6, with the addition of (— — —): Gil *et al* TC-dipole-Born [32], and (·· – – ·· – –): BEf-scaling of Kim [36].

that were, to within their stated uncertainty, in good agreement with the BEf-scaling result. These ICS data are tabulated in Thorn *et al* [36] and they illustrate the fundamental importance of the forward angle DCS in getting an accurate determination for the ICS. Clearly the best agreement in terms of the shape of the ICSs, was also found between the present results and those from Kim [36], as well as the TC-dipole-Born closure calculation from Gil *et al* [32]. On the other hand the cross sections from the TC calculation [32] and the FN R-matrix calculation of Morgan [34] did not reproduce the shape of the present $\tilde{A}^1B_1$ energy dependence.

Where disagreement between experiment and theory was found in the shape and magnitude of the $\tilde{A}^1B_1$ cross section, the possible reasons previously discussed for the $\tilde{a}^3B_1$ transition are also valid here. Those reasons include inadequacies in the representation of target states and failure to include nuclear motion in the calculations. We reiterate here that the calculation of Kim [36] incorporated

f-scaling to remove the effect of inaccurate wave functions, and gave superior agreement with the present results. This perhaps supports the argument that improved wave functions would benefit the other calculations.

Another possible source for the discrepancies in the magnitude of these ICSs, was our method to extrapolate our DCS data to forward angles prior to integrating to determine the ICSs. Since the DCSs for these transitions were so strongly forward peaked, the ICS values were very sensitive to the forward angle extrapolation. In studies of the elastic ICSs for H_2O Okamoto *et al* [26] and Faure *et al* [24] found that the MPSA technique was unable to fully reproduce the extent of the very strong forward peaking caused by H_2O's high dipole moment, as discussed in section 3.4. A similar situation can also occur here, as all the present experimental electronic state DCSs are strongly peaked at forward scattering angles. However, this cannot be the only source of the observed magnitude discrepancies since there were similar magnitude discrepancies found at the DCS level, in all excited states, before the MPSA technique was applied.

For the $3a_1 \rightarrow 3sa_1$ $\tilde{B}^1A_1$ transition the present ICSs are listed in table 4.4 and plotted in figure 4.9. Here there are five sets of calculated data to compare with, including the R-matrix calculations of Morgan [34] and Gorfinkiel *et al* [35] as well as three separate calculations from Gil *et al* [32]. Gil *et al* again employed the TC and TC-dipole-Born methods, that were used for the $\tilde{A}^1B_1$ transition, and also a method incorporating a singlet coupling to better determine the target state wave functions (denoted SC). Despite the very poor magnitude agreement between the calculations and our ICS results for this transition, the agreement in terms of the shapes of the energy distributions was surprisingly good. As seen in figure 4.9, this was true for most of the calculations, especially for the TC-dipole-Born data from Gil *et al*, but with the exception of the calculation from Morgan.

Gorfinkiel *et al* [35] presented some data in support of the proposition that the size of the R-matrix box, and the number of target states included in the calculation, could be responsible for the magnitude discrepancies found between

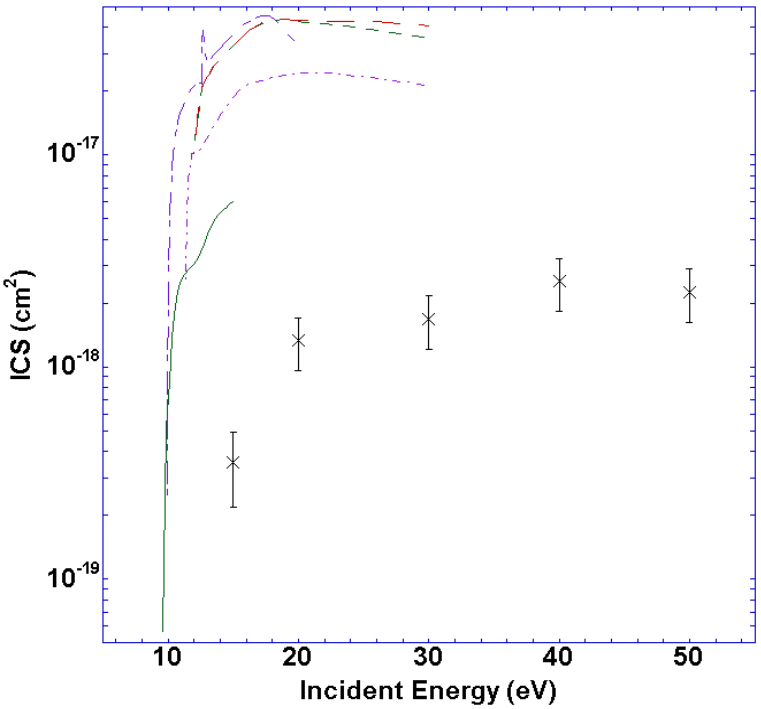

Figure 4.9: Present ICS (cm^2) for the $3a_1 \rightarrow 3sa_1$ $\tilde{B}^1A_1$ transition in H_2O. Results from the different studies are as represented in figure 4.6, with the addition of (— — —): Gil *et al* TC-dipole-Born [32] and (· - · -): Gil *et al* singlet coupled target state (SC) [32].

the R-matrix results [34] and [35] and the present study. While we have already mentioned (briefly) this line of reasoning, it is worth revisiting now in more detail. As well as the AN R-matrix calculation already discussed, Gorfinkiel *et al* also made two different FN R-matrix calculations, one which used the same target states and R-matrix box size as the AN calculations, and another which used two extra target states and an R-matrix box approximately 30% larger. They found that the results from the two FN models differed by as much as 20% in some instances. The larger FN model gave cross sections significantly lower than those from the smaller model, for the $\tilde{A}^1B_1$, $\tilde{b}^3A_1$ and $\tilde{B}^1A_1$ states, with the magnitude of the discrepancy increasing at higher incident electron energies. An even larger R-matrix box and more target states could thus potentially further increase the accuracy of the calculation, especially at the higher incident electron energies, and bring their results closer to those from the present study. Gorfinkiel *et al* also noted that they chose to limit these calculations to incident electron energies below 15eV.

Their reasoning for this was that above 12.62eV, ionisation and other excitation channels start to play a more significant role. Logically, therefore, this implies that all of the calculated cross sections would have been less reliable above 15eV. Here we propose that excitation to other channels actually becomes more significant at a lower incident electron energy, hence there is a need for the inclusion of more target states providing a better representation in all of the calculations. Spectroscopic studies have shown that there are two transitions, with $^3A_2$ and $^1A_2$ symmetry, between the $\tilde{A}^1B_1$ and $\tilde{b}^3A_1$ states in the EELS, at ≈9eV energy loss. The $^3A_2$ and $^1A_2$ states were not included by Gorfinkiel *et al* in any of their calculations, as their wavefunctions were found to be too diffuse for the R-matrix box they employed and their excitation energies were unphysical. The excitation energies that Gorfinkiel *et al* calculated for these transitions were 12.336eV for the $^3A_2$ state and 13.123eV for the $^1A_2$ state, approximately 3-4eV higher than the acceped values (Winter *et al* [42]). We assert that a better representation of these transitions and their inclusion in the calculation would have a significant effect on the cross section results they obtained. In addition there were a further 25 features fitted in our EELS below 12.06eV energy loss, some of which of course pertained to multiple transitions. The inclusion of some of these extra channels in the calculation might also significantly increase the accuracy of the R-matrix and the other calculations. Of course we appreciate that, given current computing power, such a suggestion might be easier said than put into practice. These are difficult calculations already, so that including more channels might simply not be computationally feasible at this time.

ICSs for the $1b_1 \rightarrow 3pb_2$ $^3A_2$ and $^1A_2$ transitions are plotted in figure 4.10. and tabulated in table 4.4. There have been no previous studies into the ICSs for these transitions, hence there were no other studies against which we could compare our results. Indeed we only include these states in the main body of the text, rather than placing them in appendix B, so that all of the first six excited electronic states in water are grouped together. The behaviour of these ICSs, to within the cited errors, is largely similar to what we have already seen. Namely

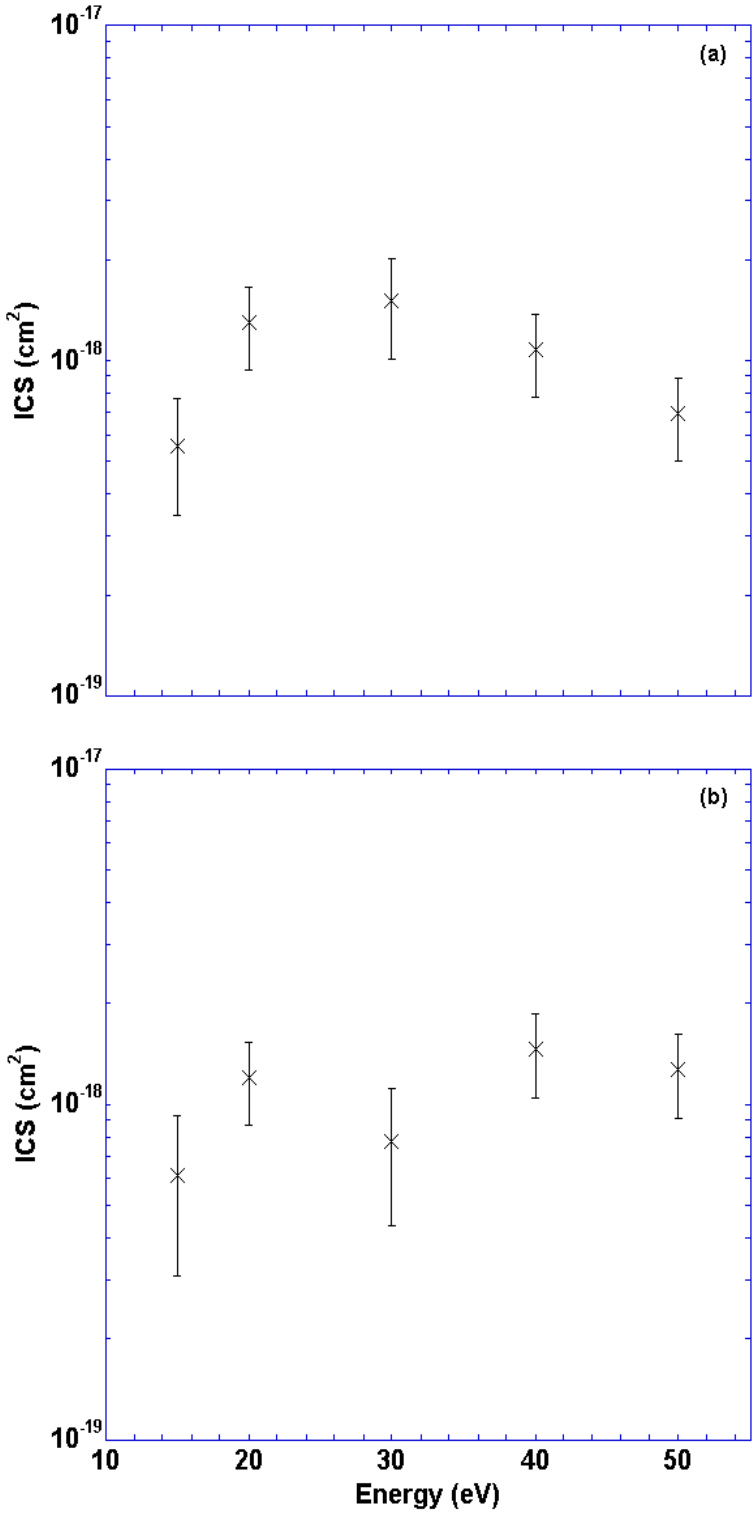

Figure 4.10: Present ICS (cm^2) of the $1b_1 \rightarrow 3pb_2$ transitions in H_2O. (a):$^3A_2$ and (b):$^1A_2$. (×) Present data. These data are plotted for completeness to provide a set of ICS for the first six excited electronic states in H_2O.

they are essentially featureless with an energy dependence which is quite typical for ICS when resonance effects are not prevalent [92].

While there have been no previous measurements of the absolute cross sections for the excited electronic states studied here, there have been other experiments that we can indirectly compare the present results against. Harb *et al* [38] measured cross sections for the production of OH from the dissociative excitation of H_2O, using laser induced fluorescence measurements. Their results are plotted in figure 4.11, along with the summation of our measured ICS for the $\tilde{a}^3B_1$, $\tilde{A}^1B_1$, $\tilde{b}^3A_1$ and $\tilde{B}^1A_1$ states, which are known to dissociate into OH ([38]). The summation of these four particular excited states was expected to somewhat underestimate the cross section from Harb *et al*, as it does not take into account that dissociation can occur through other excited states by them first losing energy to form one of these four dissociative states. However, as can be seen in figure 4.11 the present summed ICS are about an order of magnitude lower than those from Harb *et al* [38]. This amount of underestimation is larger than expected, although the shapes of the cross sections are in fact very similar. One possible explanation for this discrepancy could be due to possible inaccuracies in the old dissociative attachment data from Melton [93], which Harb *et al* [38] applied in order to normalise their cross sections to an absolute scale. Indeed Itikawa and Mason [12] have suggested the measurements from Melton [93] might suffer from some kinetic energy discrimination and they specifically called for new measurements to be made on water for this process. The data from Melton is, however, still the only currently available experimental dissociative attachment cross section on an absolute scale. Even allowing for the view of Itikawa and Mason, the extent of the magnitude discrepancy observed in figure 4.11 between the present summed ICSs, for the four relevant electronic states, and the corresponding result from Harb *et al* [38], did cause us some concern. As a consequence we sought other avenues by which we might cross check the validity of our ICSs, with one such avenue being a comparison with the grand total cross sections for electron scattering from water.

The grand total cross section (GTS), also called the total cross section, is

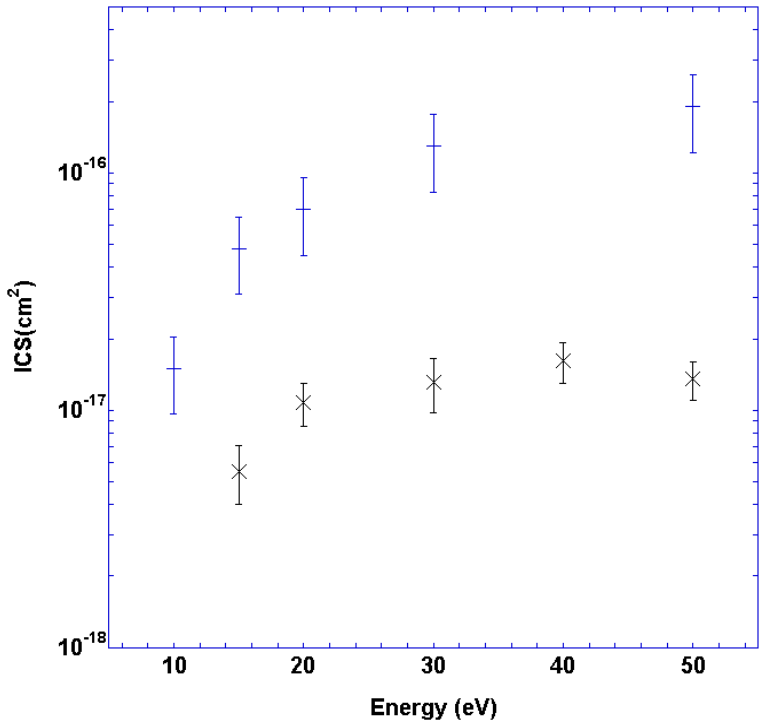

Figure 4.11: Cross sections for the production of OH from electron impact on H_2O. (×) Sum of the present ICS for the $\tilde{a}^3B_1$, $\tilde{A}^1B_1$, $\tilde{b}^3A_1$ and $\tilde{B}^1A_1$ transitions, and (-) Harb *et al* [38]. Error bars in both cases represent plus and minus one standard deviation.

the probability that some form of scattering will occur as a function of incident electron energy. In other words it represents the sum of the integral cross sections for elastic scattering, all discrete inelastic processes, all ionisation channels and all the dissociation channels. As such the sum of all our electronic excitation cross sections with those cross sections available from other workers for the other channels open in electron - H_2O collisions, should be comparable to independent measurements of the GTS. We thus made this summation by adding ICSs for elastic collisions, ionisation and vibrational excitation to the present measured ICSs for electronic excitation. The measured GTSs also include cross sections for dissociative attachment and neutral dissociation, but these were unavailable in the energy range of interest to the present study. Therefore the present integral cross section sum would be expected to somewhat underestimate the GTS value compared to the independent measurements. For the elastic cross sections we again used the values from Cho *et al* [23], while for vibrational excitation we

employed the data from Yousfi and Benabdessadok [94] who made calculations using an electron swarm parameter unfolding technique. The results from Yousfi and Benabdessadok do underestimate the values recommended by Itikawa and Mason [12], particularly above 1eV for the stretching modes and above 10eV for the bending excitation, but as they were tabulated over a larger energy range than the recommended crossed beam data [12] we preferred them in this case. Note that the range of the data set is important to us, not only for this application but also for the modelling calculations discussed later in Chapter 5. Hence for consistency we used the data of Yousfi and Benabdessadok throughout this study. In any event this choice, compared to the vibrational ICS from Itikawa and Mason, does not particularly effect the conclusions we later draw for our GTS comparison. For the ionisation cross sections we used the values from Straub *et al* [95], who employed a time-of-flight mass spectrometer to measure partial cross sections for electron-impact ionisation in H_2O from threshold to 1000eV. Note that in this case we summed their partial cross sections to get the total ionisation cross section for our "sum-of-parts" GTS values.

As can be seen from figure 4.12 the present "sum-of-parts" GTS somewhat underestimate both the GTS recommended by Itikawa and Mason [12] and that measured by Szmytkowski [37], although the error bars for each set did clearly overlap. This was expected given some channels were omitted in our sum. Further possible reasons for the slight underestimation in the present GTS included possible underestimation of the elastic integral cross section values, due to problems with the MPSA as discussed earlier, and the lack of cross section values for electronic states of vertical excitation energy greater than 12.06eV. We estimate, however, that this lack of electronic state excitation data for states of vertical excitation energy above 12.06eV would be very small, with correction for this producing a change in the sum well within the error bars. In fact we estimate the magnitude for the change in the GTS for this effect as being less than 1%. Limitations in applying the MPSA procedure to water would also effect the present estimates for the electronic-state integral cross sections. In particular they too

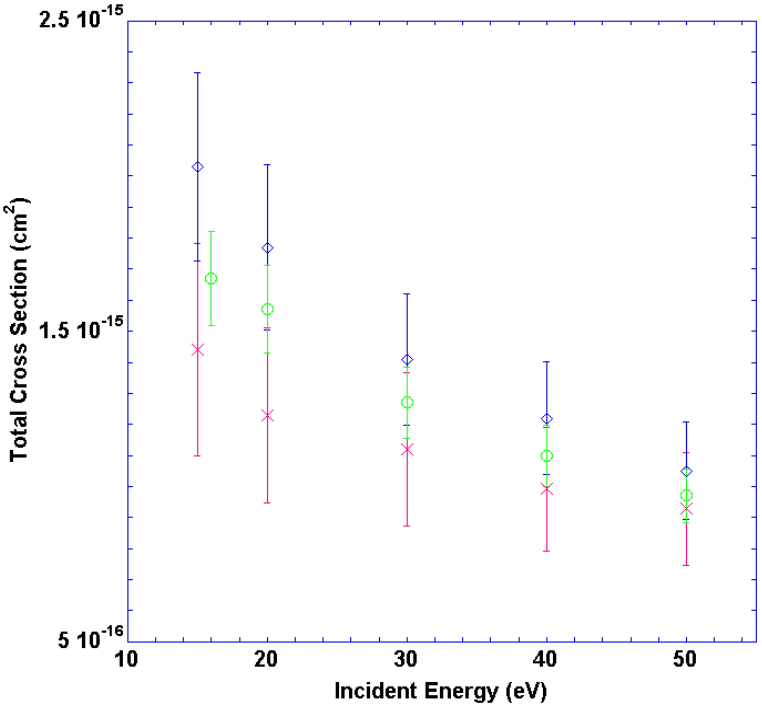

Figure 4.12: GTS (cm^2) for electron collisions with H_2O. (×) Sum of parts including the present ICS for electronic excitation and other cross sections as described in the text, (◇) GTS recommended by Itikawa and Mason [12], and (○) GTS measurement from Szmytkowski [37].

would be somewhat underestimated.

Bearing in mind the caveats we have just described, figure 4.12 indicates that the present derived "sum-of-parts" GTS is entirely consistent with the independent data ([12],[37]). This in turn gives us some confidence in the self-consistency of our electronic-state ICS. However, this is tempered by the knowledge that up to 50eV the elastic cross section component dominates the GTS. Hence the sensitivity of the derived GTS to our electronic-state ICS values might not be so strong. In light of this observation, it would be useful to have a cross check for the inelastic processes alone. Such a cross check is now described below.

We have compared our results to the "inelastic" cross sections published by Muñoz *et al* [7]. Muñoz *et al* published cross sections for the combined electron induced electronic excitation, neutral dissociation and ionisation as determined by an optical potential method. They noted that they expected their calculation to be very accurate above 50eV, but would slightly overestimate the true cross

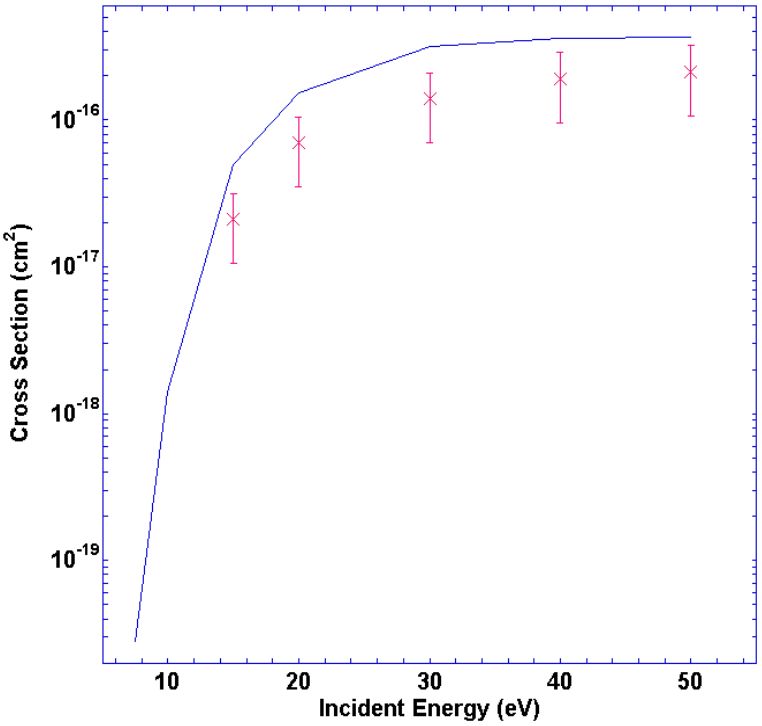

Figure 4.13: Comparison of the inelastic cross sections (cm^2). (×) Sum of all electronic state ICS from the present study and the ionisation cross sections from Straub *et al* [95], (——) corresponding inelastic cross sections from Muñoz *et al* [7].

sections at lower energies. We reiterate that this is an important cross check for the present results, as the dominant elastic ICSs are excluded in this comparison and, hence the effect of the electronic states was more significant in the overall sum. In figure 4.13, we show the result from Muñoz *et al* and the present summed electronic state ICSs and the ionisation cross sections from Straub *et al* [95]. Clearly the shape of the two cross section sets are in very good agreement, although as expected the present inelastic cross section sum is a little lower in magnitude than the independent measurements of Muñoz *et al*. Possible reasons for the underestimation in this case are the absence of neutral dissociation cross sections in our sum and the limitations in the calculation for energies below about 50eV [7]. The results of figure 4.13, however, do give us further confidence for the validity of our electronic-state ICS data base and we now use it for some computational modelling studies in the next chapter.

Chapter 5

Modelling Calculations

Earlier in this thesis we noted that the cross sections we have measured will be useful for a better understanding of such applications as radiation damage in matter [7], atmospheric phenomena [12] and even technological developments. Here we therefore give some specific, but preliminary, results illustrating the utility of the present integral cross sections for studying atmospheric behaviour. Note that many of the present integral cross sections and energy loss spectra, are also being currently employed by Garcia and colleagues [96] in their studies on low energy electron tracks in water.

In this chapter we thus discuss our calculations of electron energy transfer rates, Q_i, and excitation rates, k_i, for vibrational and electronic excitations in H_2O. In the first case the electron energy transfer rate for a particular excitation process, i, is a measure of the rate at which electrons lose energy in a collision with a molecule causing the excitation i. Collisions with neutral molecules are an important process by which electrons in the atmosphere lose energy, hence, the electron energy transfer rates are crucial for determining the electron temperature (T_e), which is in turn an important value in the study of atmospheric physics and chemistry. In the second case the excitation rate for an inelastic process i is a measure of the rate at which the particular state i is excited by secondary electrons in the environment under investigation (e.g. auroral).

These values, Q_i and k_i, were calculated as a first step towards incorporating investigations of H_2O in a statistical equilibrium model ([13]) of the ionosphere. The eventual aim of applying this statistical equilibrium model will be to determine if the atmospheric Meinel bands [17] are caused, at least in part, by electron driven processes (as described in equation (5.1)), as distinct from chemical processes (as described in equation (5.2)). To be specific:

(i) the electron-driven processes are represented as:

$$e^- + H_2O \rightarrow H_2O(\tilde{a}^3B_1, \tilde{A}^1B_1, \tilde{b}^3A_1, \tilde{B}^1A_1) \rightarrow OH(X^2\Pi, v) + H. \tag{5.1}$$

(ii) while, the chemical reactions are denoted by:

$$H + O_3 \rightarrow OH(X^2\Pi, v) + O_2. \tag{5.2}$$

$$HO_2 + O \rightarrow OH(X^2\Pi, v) + O_2.$$

It is clear from equations (5.1) and (5.2) that the Meinel bands are caused by vibrationally excited OH radicals (Meinel [16], [17]). In chapter 4 we previously alluded to the fact that the $\tilde{a}^3B_1$, $\tilde{A}^1B_1$, $\tilde{b}^3A_1$, and $\tilde{B}^1A_1$ excited states of H_2O all dissociate into OH, and hence that excitation of these states may be an intermediate step towards the production of the Meinel bands. It is also believed [38] that other higher lying excited electronic states of H_2O can also dissociate into OH, by first de-exciting into one of those four states. Such de-excitation might be through the emission of a photon or by heavy-particle quenching with a third species. In section 5.1 we discuss the methods used to calculate both the energy transfer rates and the electron impact excitation rates, while in section 5.2 the results of these calculations are discussed.

5.1 Calculation Methods

All the present calculations were made using programs written in Fortran 77 and performed on a DEC ALPHA 433MHz, 320Mbytes, computer. Electron en-

ergy transfer rates and excitation rates were respectively computed for the (010) and (100)+(001) vibrational excitations and all 25 electronic state excitations for which cross sections were determined in the present study (see Chapter 3). In this work we note that the electron energy transfer rates were calculated for electron temperatures up to 12000K, while the electron impact excitation rates were calculated for altitudes between 80 to 350km.

Our method for calculating the energy transfer rates was the same as that described by Jones *et al* [97], in that case for vibrational excitations in O_2. The electron energy transfer rate, Q_i, for excitation from the ground vibrational level of the ground electronic state to electronic or vibrational state i, is given below in equation (5.3) [98]:

$$Q_i = E_i \left(\frac{8 k_B T_e}{\pi m_e} \right)^{\frac{1}{2}} \int_0^\infty \sigma_i (x)\, x \exp(-x)\, dx, \tag{5.3}$$

where

$$x = \frac{E}{k_B T_e}$$

In equation (5.3) σ_i is the ICS for excitation from the ground vibrational level of the ground electronic state to the excited state i, k_B is Boltzman's constant, m_e is the electron mass and E_i is the vertical excitation energy for the transition of interest, as listed in table 3.1. In addition to these values we note that E_i=0.198eV for the (010) bending mode, and E_i=0.453eV for the unresolved symmetric and asymmetric stretch modes.

In calculating the energy transfer rates for the electronic excitations, we used the ICS determined in the present study. Recall that those data were presented in section 4.3. For the vibrational excitations the cross sections used were determined by Yousfi and Benabdessadok [94], who employed an electron swarm parameter unfolding technique. Those results were also discussed previously in section 4.3. In order to evaluate the integral in equation (5.3), the cross sections employed in our calculations are each linearly interpolated and extrapolated beyond the final data point (50eV for the electronic states and ≈80eV for the vibrational cross sections). They are also extrapolated to a value of 0cm^2 at their respective threshold energies.

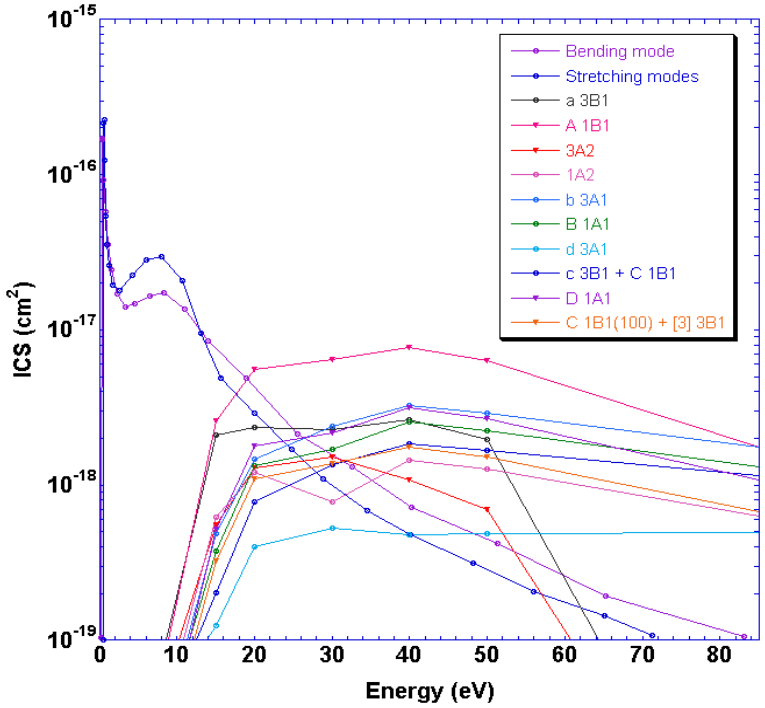

Figure 5.1: A selection of our linearly interpolated and extrapolated ICS (cm^2), as a function of electron energy (eV), as used in the present computations. The electronic state excitation cross sections are from the present study, while the vibrational excitation cross sections are from Yousfi and Benabdessadok [94]. The respective excitation processes are as labelled in the figure.

A selection of these interpolated and extrapolated cross sections are plotted in figure 5.1.

The electron impact excitation rates k_i, for the various excitations i, were computed using equation (5.4) below, which was taken from Campbell *et al* [14]:

$$k_i = \int_0^\infty F(E)\sigma_i(E)dE \tag{5.4}$$

In equation (5.4) $\sigma_i(E)$ is the integral cross section for the transition of interest, and we note that we used the same cross sections here that were employed just above in the calculations of the energy transfer rates. In this case E is the electron energy and $F(E)$ is the electron energy distribution spectrum. The electron distribution spectrum used in our current calculation was the same as that detailed by Jones *et al* [15] and Campbell *et al* [14]. As a consequence we do not repeat that detail here except to note that this electron distribution spectrum was dependent on altitude, and was a combination of the thermal electron distribution

and that for the auroral secondary electron spectrum of interest to us here. The thermal electron spectrum was assumed to be a Maxwell-Boltzmann electron distribution, with the electron temperature and density taken from the International Reference Ionosphere [99], [14]. The auroral secondary electron spectrum was determined using previous measurements from medium strength (IBC II^+) aurorae as described by Campbell *et al* [14]. However, using this method the minimum altitude of the resulting electron distribution was only 130km. Since we wanted our excitation rate calculations to be made in the altitude range 80 to 350km, the procedure described by Jones *et al* [15] was used to extrapolate this data to lower heights. This method of extrapolation involved evaluating equation (5.5), for each height, h:

$$F_h = F_{120} e^{-0.1(120-h)}, \tag{5.5}$$

where,

$$F_{120} = F_{130} + \frac{E_{120} - E_{130}}{E_{350} - E_{130}} \left(F_{350} - F_{130}\right), \tag{5.6}$$

and

$$E_{h'} = 1 - e^{-0.027(h'-60)}. \tag{5.7}$$

In equations (5.5) to (5.7), h' refers to any altitude, while F'_h is the secondary electron distribution at altitude h'. F_{130} and F_{350} were determined using the shape of the electron distributions published by Lummerzheim and Lilensten [100], at 150km and 300km respectively, and then multiplying these distributions by a factor of 27 in order to obtain spectra of the same magnitude as those estimated by Feldman and Doering [101] and measured by Lummerzheim *et al* [102] for an IBC II^+ aurora. Full details of this process can be found in Campbell *et al* [14] and references therein. Examples of the resulting secondary electron distributions are plotted in figure 5.2, for 80km, 130km and 350km altitudes.

It is apparent from equations (5.4) and (5.3), that if the secondary electron spectrum in equation (5.4) were to be replaced with the Maxwell-Boltzmann dis-

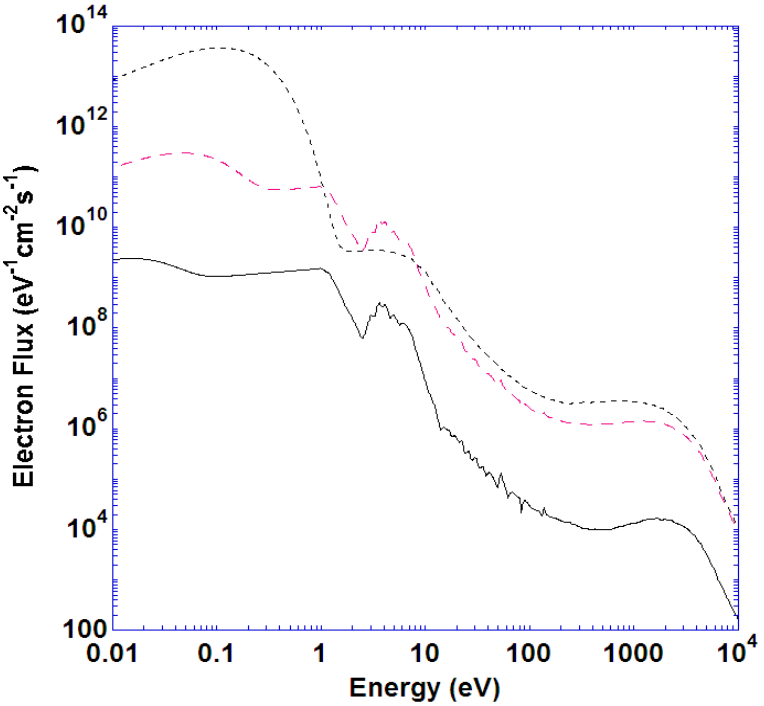

Figure 5.2: Electron flux ($eV^{-1}cm^{-2}s^{-1}$) as a function of electron energy (eV), as used in our calculation of the excitation rates. The respective altitudes for each secondary electron distribution are: (——) 80km, (– – –) 130km, (- - -) 350km.

tribution then the resulting k_i value would simply be the same as that for Q_i where the latter was divided by the vertical excitation energy for the transition in question. This feature was exploited by us as a cross check, to make sure that the two separate programs, used for the calculation of each parameter k_i and Q_i were giving consistent values.

5.2 Results of the Present Calculations

Results from our calculations of the electron energy transfer rates for vibrational and electronic state excitations in H_2O are plotted in figures 5.3 to 5.6. This is the first time such computations have been attempted for these processes, and as such there are no other data against which we can compare the present results. Nonetheless it is clear from these plots that the energy transfer rates are considerably smaller for the electronic transitions (see figures 5.3 - 5.5), compared to

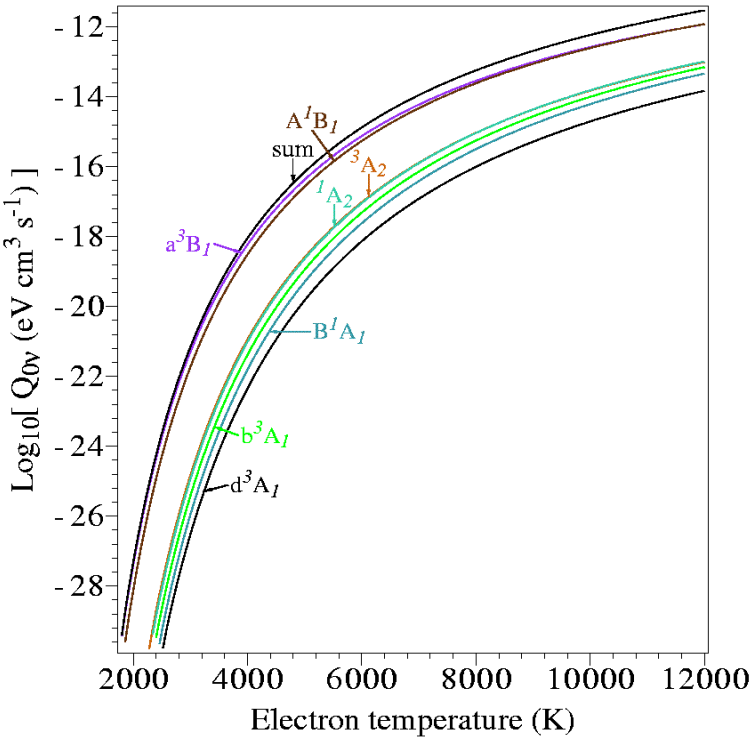

Figure 5.3: Plot of the present electron energy transfer rates ($eVcm^3s^{-1}$), as a function of electron temperature (K), for first seven excited electronic states in H_2O, as labelled on the plot. Also shown is the sum of the energy transfer rates for all 25 electronic states.

the vibrational transitions (see figures 5.6). Hence electronic excitations in H_2O represent a much smaller contribution to the electron cooling process than the vibrational excitations, when dealing with a thermal electron energy distribution.

To assist modellers who would use data such as this in their studies on climate, for example, we have fitted a power series function, via a least squares method, to each of the energy transfer rates in figures 5.3 - 5.6. That power series has the form given below in equation (5.8), and the resulting coefficients of the fitted power series are listed in table 5.1. Note that although not explicitly shown, the resulting fits using equation (5.8) to our respective energy transfer rates were all excellent. Indeed a reduced χ^2 value close to unity was achieved in each case [78].

$$log(Q_i) = A_i + B_i T_e^{1/2} + C_i T_e + D_i T_e^{3/2} + E_i T_e^2 + F_i T_e^{5/2} + G_i T_e^3 + H_i T_e^{7/2} + I_i T_e^4 \quad (5.8)$$

The electron impact excitation rates for the present electronic state excitations, as calculated using equation (5.4), are plotted in figures 5.7 and 5.8. It is clear

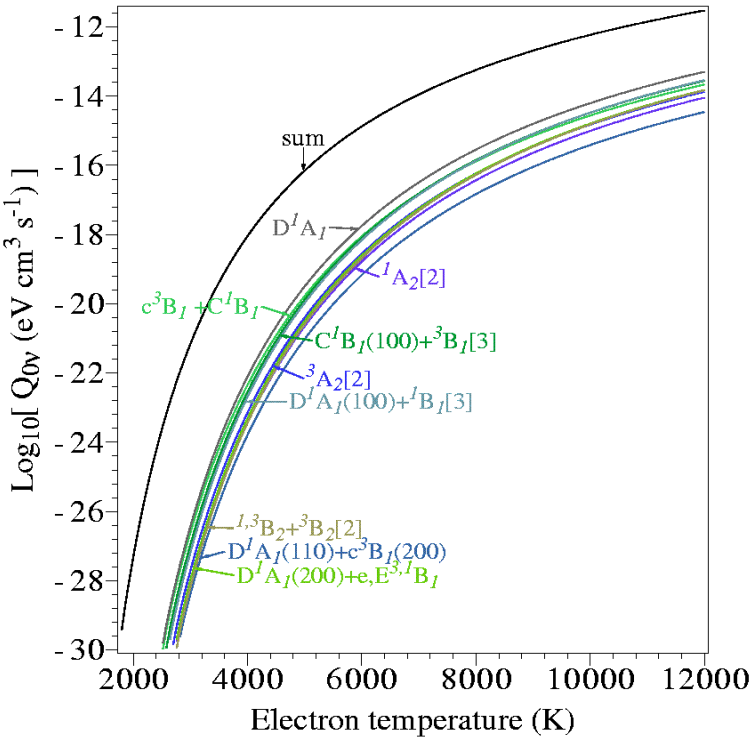

Figure 5.4: Plot of the present electron energy transfer rates ($eVcm^3s^{-1}$), as a function of electron temperature (K), for more of the excited electronic states in H_2O as labelled in the plot. Also shown is the sum of the energy transfer rates for all 25 electronic states.

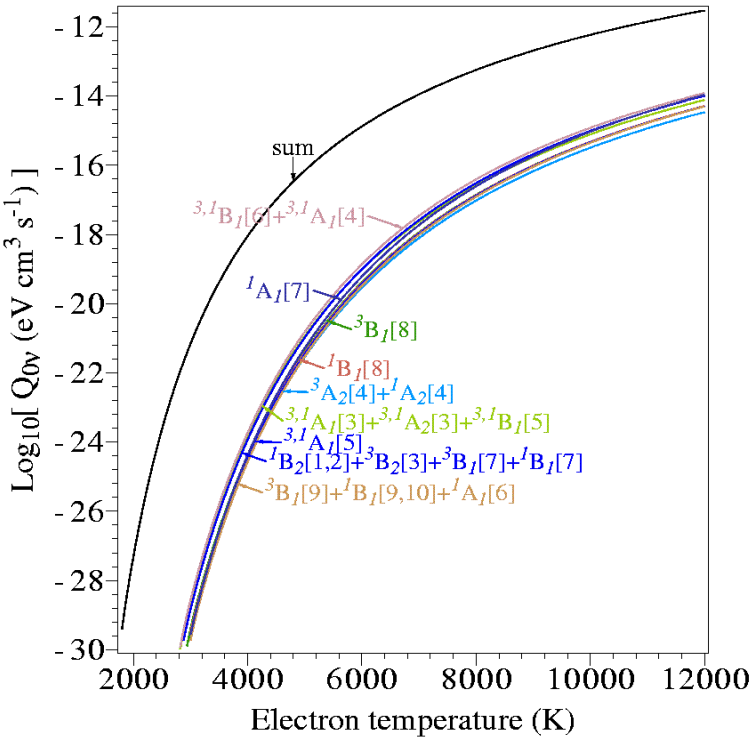

Figure 5.5: Plot of the present electron energy transfer rates ($eVcm^3s^{-1}$), as a function of electron temperature (K), for the remaining excited electronic states in H_2O as labelled in the plot. Also shown is the sum of the energy transfer rates for all 25 electronic states.

State	A_i	B_i	C_i	D_i	E_i	F_i	G_i	H_i	I_i
(010)	-37.98	3.32	-1.76×10^{-1}	5.37×10^{-3}	-1.02×10^{-4}	1.23×10^{-6}	-9.06×10^{-9}	3.75×10^{-11}	6.66×10^{-14}
(100)+(001)	-53.94	4.72	-2.28×10^{-1}	6.44×10^{-3}	-1.14×10^{-4}	1.29×10^{-6}	-9.02×10^{-9}	3.56×10^{-11}	-6.06×10^{-14}
$\tilde{a}^3B_1$	-192.48	7.40	-2.72×10^{-2}	-4.93×10^{-3}	1.50×10^{-4}	-2.12×10^{-6}	1.67×10^{-8}	-6.99×10^{-11}	1.23×10^{-13}
$\tilde{A}^1B_1$	-182.22	5.46	9.05×10^{-2}	-8.62×10^{-3}	2.18×10^{-4}	-2.91×10^{-6}	2.22×10^{-8}	-9.16×10^{-11}	1.59×10^{-13}
$^3A_2$	-217.11	6.49	1.05×10^{-1}	-9.87×10^{-3}	2.46×10^{-4}	-3.23×10^{-6}	2.42×10^{-8}	-9.82×10^{-11}	1.68×10^{-13}
$^1A_2$	-175.83	3.05	2.18×10^{-1}	-1.17×10^{-2}	2.57×10^{-4}	-3.17×10^{-6}	2.28×10^{-8}	-8.96×10^{-11}	1.50×10^{-13}
$\tilde{b}^3A_1$	-187.82	3.90	1.88×10^{-1}	-1.10×10^{-2}	2.47×10^{-4}	-3.06×10^{-6}	2.20×10^{-8}	-8.66×10^{-11}	1.44×10^{-13}
$\tilde{B}^1A_1$	-205.30	4.71	1.88×10^{-1}	-1.19×10^{-2}	2.73×10^{-4}	-3.45×10^{-6}	2.52×10^{-8}	-1.00×10^{-10}	1.69×10^{-13}
$\tilde{d}^3A_1[2]$	-185.00	1.59	3.65×10^{-1}	-1.72×10^{-2}	3.68×10^{-4}	-4.49×10^{-6}	3.21×10^{-8}	-1.26×10^{-10}	2.10×10^{-13}
$\tilde{c}^3B_1[2]+\tilde{C}^1B_1[2]$	-198.45	1.04	4.71×10^{-1}	-2.18×10^{-2}	4.71×10^{-4}	-5.80×10^{-6}	4.19×10^{-8}	-1.66×10^{-10}	2.79×10^{-13}
$\tilde{D}^1A_1[2]$	-190.37	1.68	3.75×10^{-1}	-1.77×10^{-2}	3.79×10^{-4}	-4.63×10^{-6}	3.31×10^{-8}	-1.30×10^{-10}	2.17×10^{-13}
$^1B_1[2](100)+^3B_1[3]$	-252.84	6.34	2.37×10^{-1}	-1.58×10^{-2}	3.74×10^{-4}	-4.80×10^{-6}	3.55×10^{-8}	-1.43×10^{-10}	2.43×10^{-13}
$^1B_1[3]+^1A_1[2](100)$	-235.91	6.31	1.56×10^{-1}	-1.17×10^{-2}	2.76×10^{-4}	-3.50×10^{-6}	2.55×10^{-8}	-1.01×10^{-10}	1.69×10^{-13}
$^3A_2[2]$	-255.52	6.76	1.97×10^{-1}	-1.41×10^{-2}	3.35×10^{-4}	-4.28×10^{-6}	3.15×10^{-8}	-1.26×10^{-10}	2.12×10^{-13}
$^1A_1[2](110)+^1B_1[2](200)$	-232.55	6.21	1.36×10^{-1}	-1.04×10^{-2}	2.43×10−4	-3.04×10^{-6}	2.18×10−8	-8.50×10^{-11}	1.40×10^{-13}
$^1A_2[2]$	-218.73	3.60	3.04×10^{-1}	-1.58×10^{-2}	3.46×10^{-4}	-4.23×10^{-6}	3.01×10^{-8}	-1.17×10^{-10}	1.93×10^{-13}
$\tilde{e}^3B_1[4]+\tilde{E}^1B_1[4]+^1A_1[2](200)$	-214.99	3.31	3.12×10^{-1}	-1.60×10^{-2}	3.47×10^{-4}	-4.24×10^{-6}	3.02×10^{-8}	-1.18×10^{-10}	1.94×10^{-13}
$^3B_2+^1B_2+^3B_2[2]$	-253.22	4.24	3.92×10^{-1}	-2.08×10^{-2}	4.64×10^{-4}	-5.76×10^{-6}	4.16×10^{-8}	-1.64×10^{-10}	2.74×10^{-13}
$^3A_1[3]+^1A_2[3]+^1A_1[3]+^3A_2[3]+^1B_1[5]+^3B_1[5]$	-340.25	12.15	7.66×10^{-2}	-1.36×10^{-2}	3.62×10^{-4}	-4.85×10^{-6}	3.65×10^{-8}	-1.48×10^{-10}	2.52×10^{-13}
$^1B_1[6]+^3B_1[6]+^3A_1[4]+^1A_1[4]$	-320.73	11.00	9.06×10^{-2}	-1.31×10^{-2}	3.40×10^{-4}	-4.51×10^{-6}	3.38×10^{-8}	-1.36×10^{-10}	2.31×10^{-13}
$^1B_2[2,3]+^3B_2[3]+^3B_1[7]+^1B_1[7]$	-250.50	5.83	2.29×10^{-1}	-1.43×10^{-2}	3.25×10−4	-4.02×10^{-6}	2.88×10^{-8}	-1.12×10^{-10}	1.85×10^{-13}
$^3A_2[4]+^1A_2[4]$	-211.30	2.77	3.18×10^{-1}	-1.54×10^{-2}	3.24×10^{-4}	-3.86×10^{-6}	2.68×10^{-8}	-1.02×10^{-10}	1.66×10^{-13}
$^3B_1[8]$	-255.49	3.63	4.29×10^{-1}	-2.16×10^{-2}	4.71×10^{-4}	-5.75×10^{-6}	4.09×10^{-8}	-1.59×10^{-10}	2.63×10^{-13}
$^1B_1[8]$	-206.46	2.94	2.80×10^{-1}	-1.37×10^{-2}	2.86×10^{-4}	-3.37×10^{-6}	2.32×10^{-8}	-8.75×10^{-11}	1.40×10^{-13}
$^3A_1[5]+^1A_1[5]$	-218.13	3.36	2.91×10^{-1}	-1.46×10^{-2}	3.10×10^{-4}	-3.69×10^{-6}	2.56×10^{-8}	-9.75×10^{-11}	1.57×10^{-13}
$^1A_1[6]+^3B_1[9]+^1B_1[9,10]$	-244.26	4.12	3.34×10^{-1}	-1.75×10^{-2}	3.80×10^{-4}	-4.61×10^{-6}	3.26×10^{-8}	-1.26×10^{-10}	2.06×10^{-13}
$^1A_1[7]$	-217.71	3.18	3.01×10^{-1}	-1.49×10^{-2}	3.14×10^{-4}	-3.72×10^{-6}	2.58×10^{-8}	-9.82×10^{-11}	1.58×10^{-13}

Table 5.1: Coefficients that result from the fitting of equation (5.8) to our computed electron energy transfer rates. The various vibrational and electronic state transitions are lablled in the far left column.

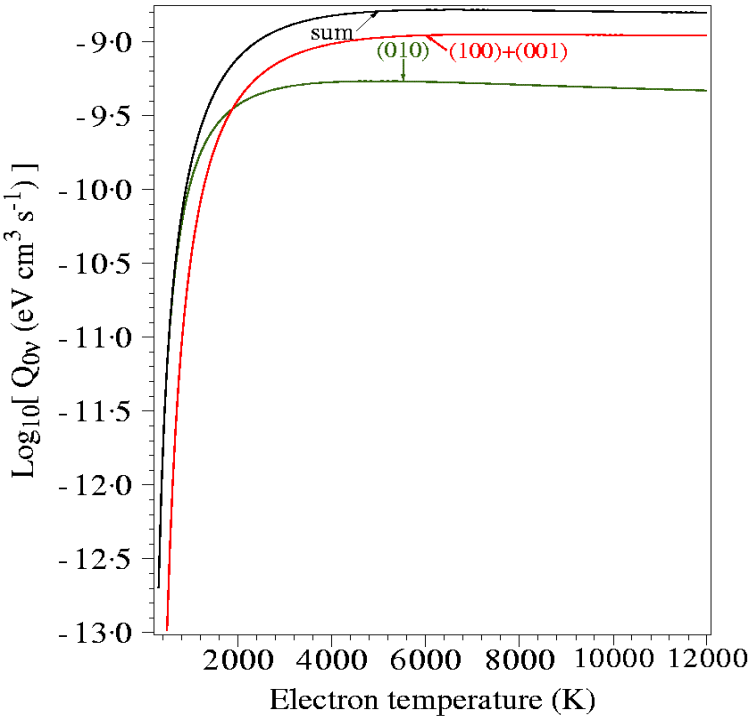

Figure 5.6: Plot of the present electron energy transfer rates ($eVcm^3s^{-1}$), as a function of electron temperature (K), for the (010) and (100)+(001) vibrational states of H_2O as labelled in the plot. Also shown is the sum of the energy transfer rates for these vibrational transitions.

from these figures that, similar to the case for the energy transfer rates, the excitation rates for the vibrational transitions were much greater than those for the electronic states. This disparity was also found to have increased at the higher altitudes. This behaviour, in this case, was essentially caused by the very large difference in the flux of electrons with energy above the excitation thresholds for the vibrational states, compared to the corresponding flux for electrons with energies above the thresholds of the electronic states. As can be seen from figure 5.2, the flux of electrons with energy great enough to excite the vibrational states was $\approx$10 times greater at 80km, and $\approx 10^4$ times greater at 350km, than the flux of electrons with energy above the excitation thresholds for the electronic states.

The excitation rates are an important parameter in the statistical equilibrium code, however this code still cannot be fully implemented. More data needs to be sourced and included in the program to complete a detailed study of the role of electron-driven processes in H_2O. This extra data includes rates for de-excitation

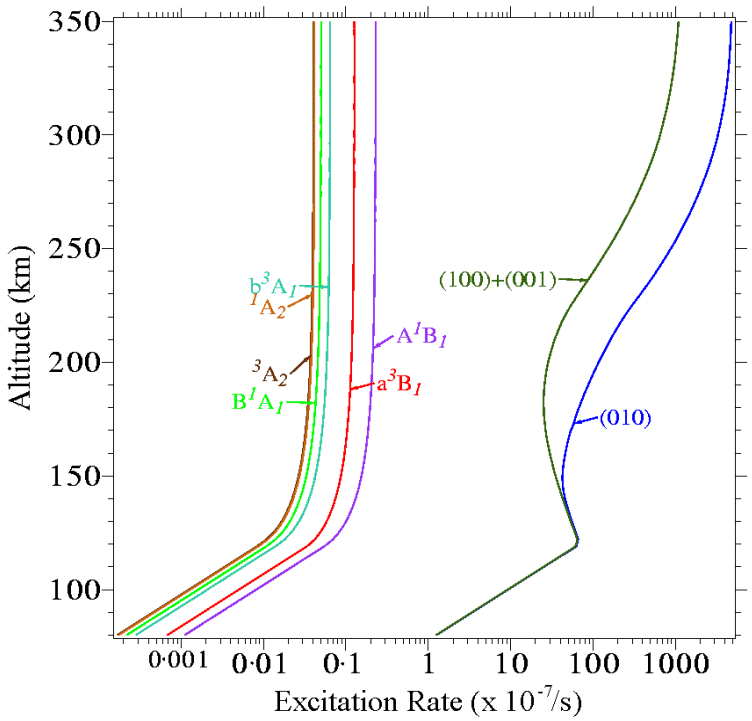

Figure 5.7: Present electron impact excitation rates ($\times 10^{-7}$ /s), as a function of altitude (km), for the vibrationally excited states and first six excited electronic states of H_2O as labelled in the plot.

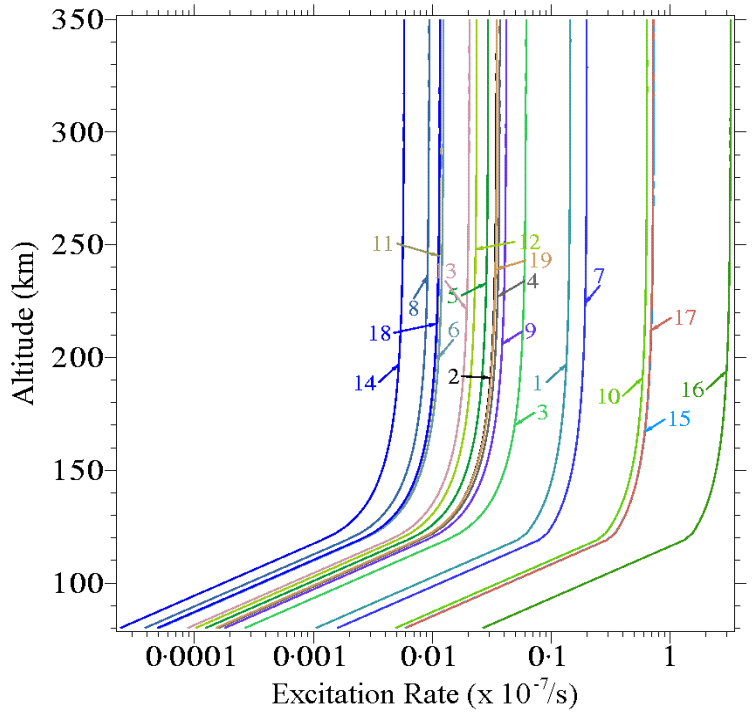

Figure 5.8: Present electron impact excitation rates ($\times 10^{-7}$ /s), as a function of altitude (km), for the remaining excited electronic states pertaining to this study. These remaining states are labelled 1 through 19, see table 3.1. Here 1 refers to the $\tilde{d}^3A_1[2]$ state, while 19 refers to the $^1A_1[7]$ state.

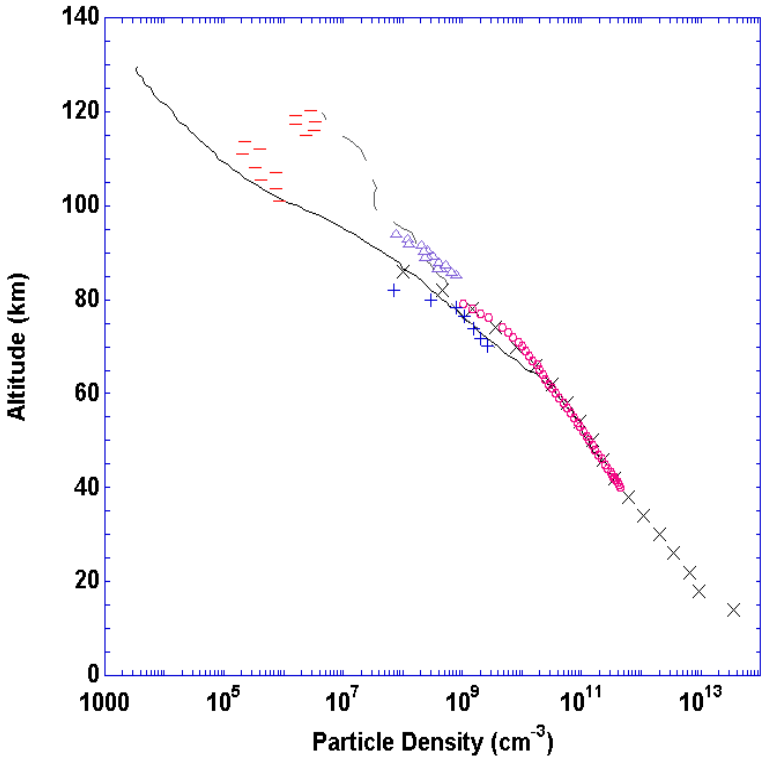

Figure 5.9: The altitude (in km) dependence for the particle densities (cm^{-3}) of atmospheric H_2O, as determined in various studies. (×): Gunson *et al* [104], (○) Edwards *et al* [105], (——) Körner and Sonnemann, (- — -) Grossmann *et al* [106], (△) Arnold and Krankowsky [107], (+) Swider and Narcisi [108], and (-) Solomon *et al* [109].

from the excited states of H_2O in the form of transition probabilities. It also includes rates for non-radiative de-excitation through collisions with other molecules and atoms (i.e. quenching rates), as well as the atmospheric density of H_2O. The atmospheric densities of H_2O, from several sources, are plotted in figure 5.9. Note that where the data plotted in figure 5.9 was originally published in units of parts per million by volume (ppmv) they were converted here to cm^{-3} using air densities from NASA's MSISE Model 1990 calculation [103]. It is apparent from figure 5.9 that below ≈80km in altitude the atmospheric H_2O densities are actually quite well established. However, at higher altitudes the situation is much less clear as there have been fewer studies and no direct measurements. We now discuss the available data in more detail.

Above an altitude of ≈85km, figure 5.9 shows the results from studies by Körner and Sonnemann [110], Grossmann *et al* [106], Arnold and Krankowsky

[107] and Solomon *et al* [109]. Körner and Sonnemann calculated H_2O densities for altitudes between ≈50km to 130km, using a coupled dynamic and chemical model at 2.5°N at the time of the summer solstice. On the other hand, Grossmann *et al* determined H_2O densities in November and December at ≈69°N and 67°N for altitudes in the range ≈70km to 120km. In that work they measured the far infrared pure rotational spectrum of water vapour, and from those spectra determined number densities by fitting to them a calculated spectrum with the number density as the only variable. Arnold and Krankowsky determined number densities for water in the altitude range 85km to 94km at ≈69°N and 68°N in May and August respectively. They measured positive ion concentrations using rocket-borne mass spectrometers, and determined the H_2O densities by applying a chemical equilibrium model which included the reactions producing the ions they detected from H_2O. In a different approach, Solomon *et al* determined the concentration of H_2O using the concentrations of Si^+ and $SiOH^+$ ions previously determined during meteor showers. These latter authors also applied a chemical equilibrium method, but in this case the chemical reaction considered was that between Si^+ and H_2O.

It is abundantly clear from figure 5.9 that the results from these various studies differ considerably. At an altitude of 120km the density from Körner and Sonnemann [110] was ≈100 times smaller than that from both Grossmann *et al* [106] and Solomon *et al* [109]. It is arguable that the disparity in the results of these different investigations is due to a real fluctuation in the density of H_2O, at the different times and locations of each study. Nonetheless, if this were the case it would represent a significant challenge to a statistical equilibrium investigation. In a recent report on the variability of H_2O concentration in the Earth's atmosphere, Hartmann [111] noted that above 120km in altitude the concentration of H_2O is believed to be very low and that the origin of H_2O at these altitudes is mainly limited to extraterrestrial sources (e.g. comets) and human space exploration activities (e.g. shuttles and rockets). Having said that, the different results of the previously noted studies could also be due to the different method

employed in each case. Hence some direct measurements are urgently needed to help to clarify this situation and extend our knowledge of the H_2O concentration to higher altitudes. To this end a satellite called AIM (Aeronomy of Ice in the Mesosphere) was launched by NASA on April 25th 2007, which is intended to study the nature of noctilucent clouds (NLCs), also known as polar mesospheric clouds (PMCs). This AIM satellite will be making direct measurements, using solar occulation, of the atmospheric density of H_2O in the polar regions, and even though its altitude range is only from 80 to 92km, it will shed more light on the nature of the magnitude and variability of atmospheric H_2O and its sources and sinks.

We therefore conclude that a full statistical equilibrium study remains somewhat problematic at this time, although the benefits of such a study, in the future when the necessary H_2O density information becomes available, are manifest. Hence that investigation remains a priority for the Flinders group.

Chapter 6

Conclusions

We have presented, in Chapter 4, differential and integral cross sections for electron impact electronic state excitations in H_2O. These cross sections were fundamentally determined from energy loss spectra, as measured with the crossed beam spectrometer described in Chapter 3.

The cross sections given in Chapter 4 represent the first experimentally determined absolute cross sections for electronic state excitations in H_2O. As such, it was hoped that they would help to resolve some of the disagreements seen between corresponding cross sections calculated with various theories. The current results however showed that all the previous calculations produced DCSs that were too large in magnitude. While the angular distributions of the DCSs calculated by Gil *et al* [32] for the $\tilde{A}^1B_1$ and $\tilde{B}^1A_1$ states were found to be qualitatively accurate, the DCSs calculated by Gil *et al* for the $\tilde{a}^3B_1$ and $\tilde{b}^3A_1$ states failed to reproduce the forward peaked structure that was seen in our results. The present ICS results were found to be in good overall agreement with the ICS calculated by Kim [36] for the $\tilde{A}^1B_1$ state. Beyond this, however, it was found that all the calculated ICSs, like the calculated DCSs, were too large in magnitude for all states where common data existed.

Potential causes for this overestimation of the cross section (DCS and ICS) magnitudes, by the calculations, were also given in Chapter 4. These causes

included possible limitations in the number and accuracy of the target wave functions included in the calculations, as well as the nuclear motion being either ignored or at best limited to a two dimensional adiabatic nuclei approximation. These same observations are also potential reasons for why the calculations failed to reproduce the forward peaked angular distributions observed in the experimentally determined triplet DCS data. It is proposed that, to remedy the observed magnitude and shape discrepancies, further calculations be made using a greater number of target states, more sophisticated target state wave functions and a full three dimensional representation of nuclear motion. Of course we appreciate that the capacity for theorists to do so might be limited, by constraints including the level of computational power currently available.

The present measured cross sections were, where possible, subjected to stringent cross checks against other experimental data, with the results of this process increasing our confidence in the validity of the present data. Amongst these cross checks were a comparison to the independently measured DCS data from Sophia University, with very good general agreement being found between that data and the present results. Other indirect self-consistency tests were made by comparing sums of the present ICS values with various other cross sections, as described in section 4.3. These comparisons included the cross sections for OH production by Harb *et al* [38], GTSs from Szmytkowski [37] and Itikawa and Mason [12] and inelastic cross sections from Muñoz *et al* [7]. The results of all these comparisons were promising, although in some cases they did suggest the possibility that the present ICS data might be a little low in magnitude. The origin of this possible underestimation in our ICS values would most likely be due to the forward angle extrapolation of the DCS data, through the use of the MPSA technique, prior to integration. Indeed the present ICS may, in some cases, be underestimated by as much as 30%, although even in that worst case scenario they would still usually be within our present error estimates. Nonetheless it is proposed that new ICS values be determined by reprocessing our DCS data, when and if a new extrapolation method better able to account for the strongly forward peaked nature of

the DCSs becomes available.

Another aim of this study was to produce data for use in modelling applications. We are thus very pleased that our ICSs have already been employed, not only in our own calculations of rates for atmospheric processes, but also in calculations of electron tracks in H_2O by Garcia *et al* [96], as well as in Monte Carlo simulations for drift velocities of electrons in water vapour by Ness *et al* [112]. This last work is briefly expanded upon here because it has further increased our confidence in the present results and we have not previously included a discussion of it in the main body of the thesis. Note that the reason it was not presented earlier is simply because it has been a very recent development. Hasegawa *et al* [113], in 2007, measured the drift velocity for electrons in water vapour for E/N from 60 to 1000Td. Drift velocities previously simulated by Ness *et al* [112], showed relatively poor agreement with these new measured values for E/N$\geq$100Td, while for E/N$\leq$40Td their calculation showed good agreement with other earlier but more limited measurements by Cheung and Elford [114]. As a consequence Ness *et al* [112] recalculated the drift velocities, using different sets of cross sections including those determined in the present study. They [112] found that inclusion of the present ICSs in their cross section data base significantly improved the agreement between their simulations and the experimental data above E/N $\approx$100Td, a result that indicated the importance of including these ICSs in order to understand the physics at the microscopic scale.

Chapter 5 also described the use of the present ICSs for electronic state excitation, and previously determined ICSs [94] for vibrational excitation, to calculate atmospherically relevant electron energy transfer rates and excitation rates for these inelastic processes. The calculation of these rates was an important first step towards including H_2O in the statistical equilibrium code of the Earth's Ionosphere. However, even more data is still needed before H_2O can be fully integrated into the statistical equilibrium code; including transition probabilities, quenching rates and atmospheric densities of H_2O at the relevant altitudes. We recommend that once this extra data is determined, or successfully located in the

existing literature, the statistical equilibrium code be updated and a full investigation of electron-driven processes in atmospheric H_2O be conducted.

We have therefore presented a comprehensive set of DCS and ICS for electron impact excitation of electronic states in H_2O. These cross sections, particularly at the ICS level, were subjected to many self-consistency tests and in the main passed them with flying colours. We thus believe the present cross sections will be very useful in the modelling of and understanding for many applied phenomena, including the role of electron-driven processes in our atmosphere.

Appendix A

Additional Differential Cross Section Plots and Tables

The DCSs for the remaining 18 features that were fitted to the EELS, but not previously discussed in Chapter 4, are plotted in figures A.1 to A.7 and tabulated in tables A.1 to A.7. With the exception of the cross check measurements made by the group at Sophia University at 10°, for some of these transitions, and the distorted wave Born calculation by Lee *et al* [33] for the $3a_1 \rightarrow 3pa_1\ ^3\mathrm{A}_1$ transition, there were no other results for us to compare against. We were however unable to make a detailed analysis and comparison with the calculation from Lee *et al* for the $3a_1 \rightarrow 3pa_1\ ^3\mathrm{A}_1$ transition, as in our EELS the feature assigned to this transition was strongly overlapped and could thus not be independently resolved.

Generally similar trends were found among the cross sections for these remaining higher energy loss transitions. In addition these trends were similar to those found previously for the $\tilde{a}^3\mathrm{B}_1$, $\tilde{A}^1\mathrm{B}_1$, $^3\mathrm{A}_2$, $^1\mathrm{A}_2$, $\tilde{b}^3\mathrm{A}_1$ and $\tilde{B}^1\mathrm{A}_1$ transitions discussed in Chapter 4. That is the cross sections for all the states, irrespective of whether they were singlets and triplets (or combinations of transitions), usually had a forward peaked angular distribution, with the degree of forward peaking increasing at the higher incident electron energies. Possible reasons for this forward peaking, where it was unexpected e.g. for the triplet features, were outlined

in Chapter 4, and therefore are not repeated again here. Note that many of these higher energy loss features were assigned to a combination of transitions so that the forward peaking in the differential cross sections for these features could well be due to the contribution from the singlet transitions to those features. For transitions above ≈11.60eV (figure A.5) the spectral assignment of the observed features becomes very problematic. Here our assignments were made based on what previous spectroscopic studies predicted the dominant transitions for each of these features (Chapter 2) would be. However it is quite likely that each of these features is actually a composite of more than one unique transition. Hence it is quite probable that the forward peaked structure in, for example, the $1b_1 \rightarrow 4da_1$ $^3B_1$ feature of figure A.5.(c) and (d) was due to unidentified overlapping features of singlet character. It is also notable that no DCS was determined at θ=10° for the $1b_1 \rightarrow 3pb_1$ $\tilde{d}^3A_1$ transition at 15eV (figure A.1.(a)). This was because this feature was too small in intensity in the measured spectra, and was also overlapped strongly by other features. Thus a unique spectral deconvolution for its DCS at that scattering angle was not possible.

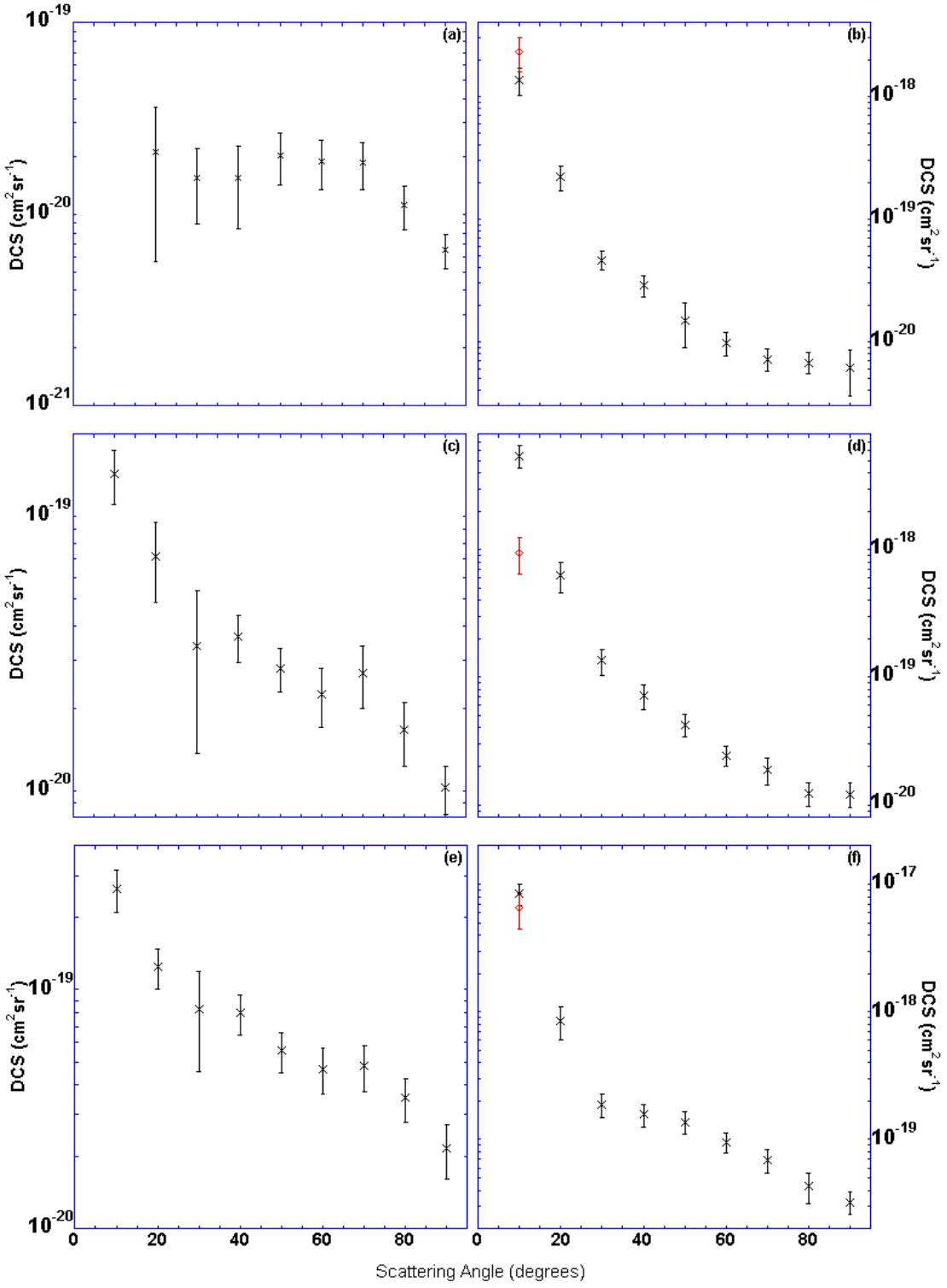

Figure A.1: DCSs (cm^2/sr), as a function of electron scattering angle (°), for various transitions and energies in H_2O (a): $1b_1 \rightarrow 3pb_1$ $\tilde{d}^3A_1$ 15eV, (b): 50eV, (c): $1b_1 \rightarrow 3pa_1$ $\tilde{c}^3B_1$ + $\tilde{C}^1B_1$ 15eV and (d): 50eV, (e): $1b_1 \rightarrow 3pb_1$ $\tilde{D}^1A_1$ 15eV, (f): 50eV. (×) Present data, (◇) Sophia data.

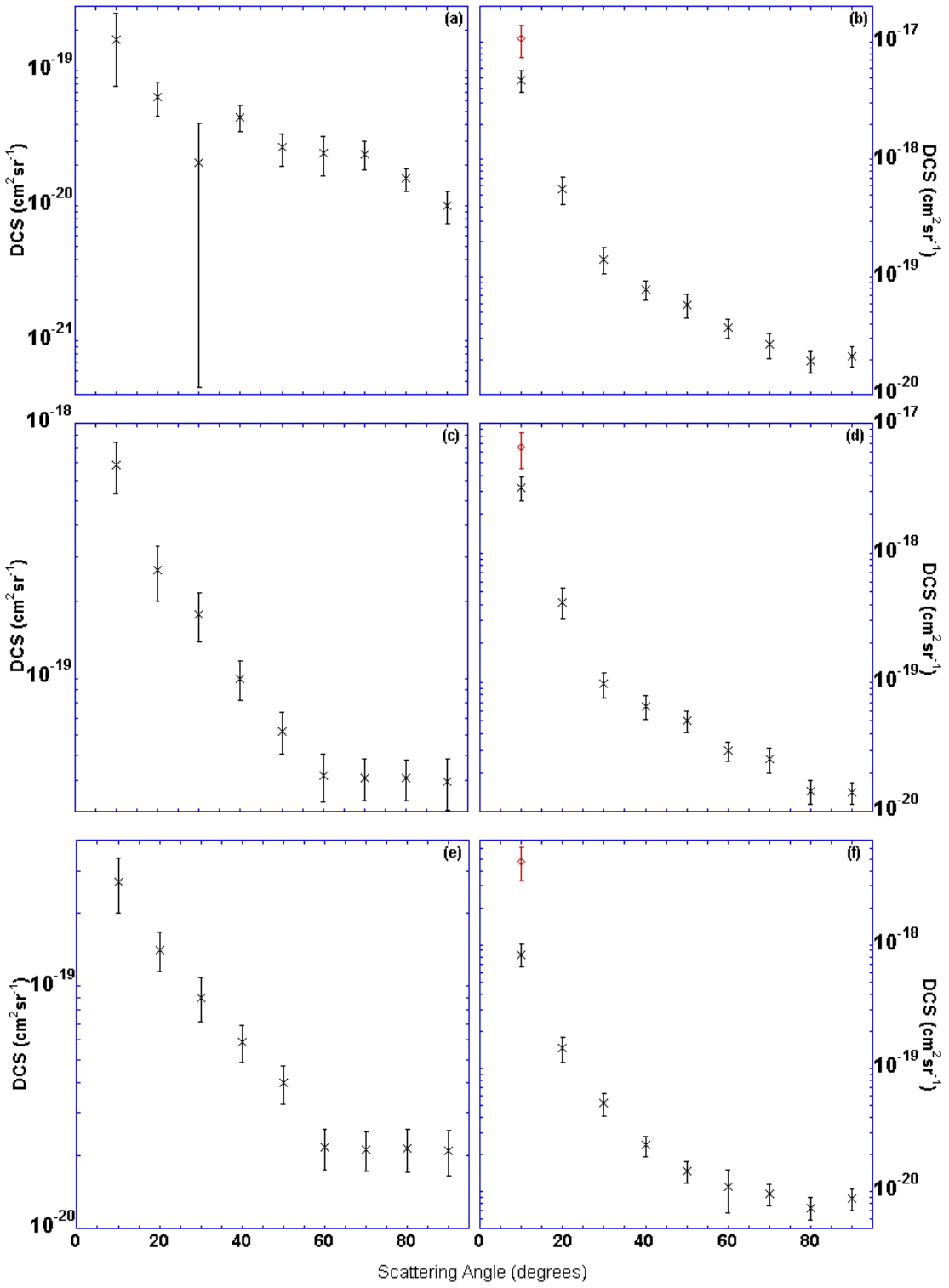

Figure A.2: DCSs (cm^2/sr), as a function of electron scattering angle (°), for various transitions and energies in H_2O (a): $1b_1 \rightarrow 3pa_1$ $\tilde{C}^1B_1(100) + 1b_1 \rightarrow 4sa_1$ $^3B_1$ 15eV, (b): 50eV, (c) $1b_1 \rightarrow 4sa_1$ $^1B_1 + 1b_1 \rightarrow 3pb_1$ $\tilde{D}^1A_1(100)$ 20eV, (d): 50eV, (e): $1b_1 \rightarrow 3db_2$ $^3A_2$ 20eV, (f): 50eV. (×) Present data, (◇) Sophia data.

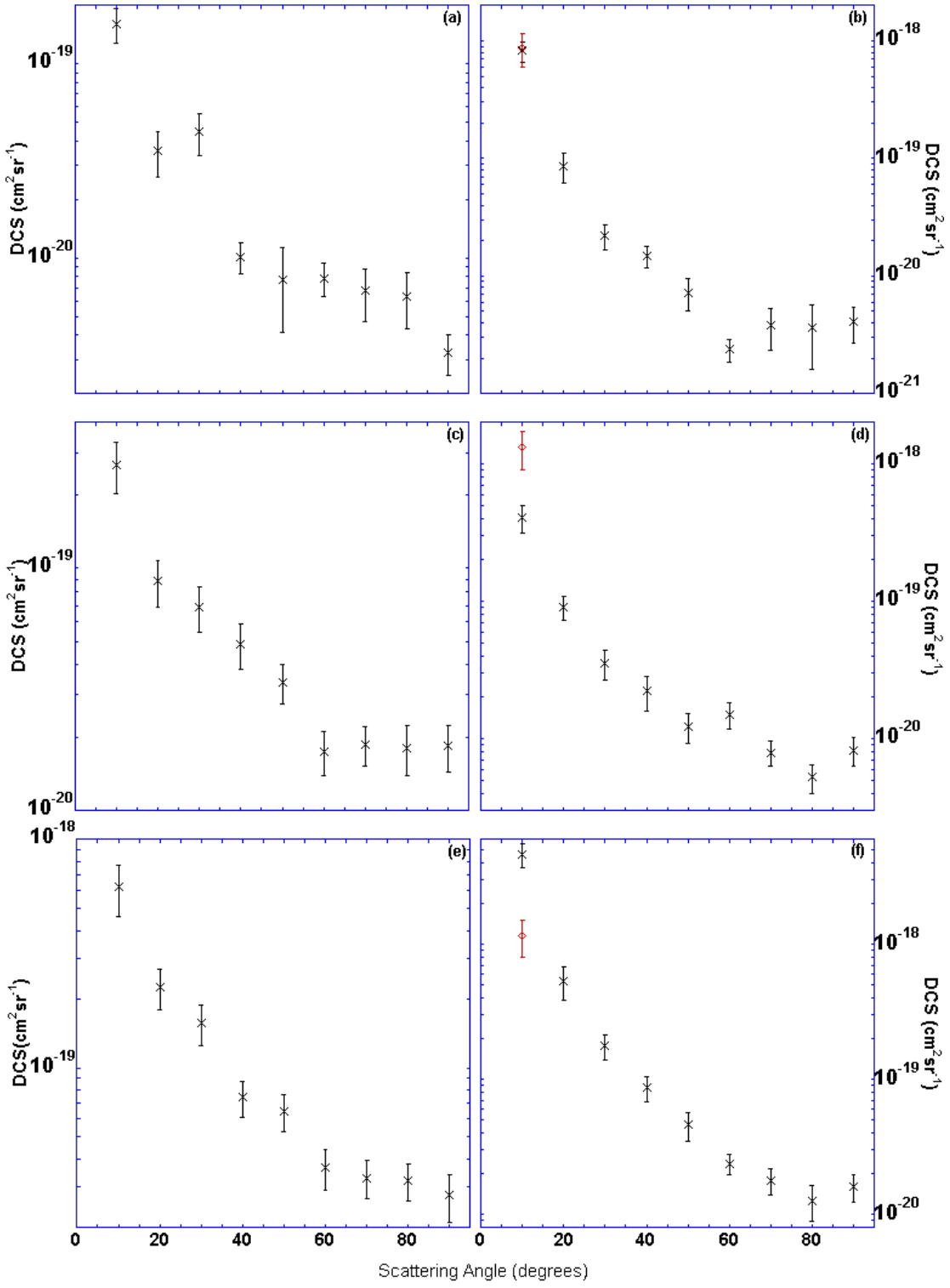

Figure A.3: DCSs (cm^2/sr), as a function of electron scattering angle (°), for various transitions and energies in H_2O (a): $1b_1 \rightarrow 3pb_1$ $\tilde{D}^1A_1(110)$ + $1b_1 \rightarrow 3pa_1$ $\tilde{C}^1B_1(200)$ 20eV, (b): 50eV, (c) $1b_1 \rightarrow 3db_2$ $^1A_2$ 20eV, (d): 50eV, (e): $1b_1 \rightarrow 3pb1$ $\tilde{D}^1A_1(200)$ + $1b_1 \rightarrow 3da_1$ $\tilde{e}^3B_1$ + $\tilde{E}^1B_1$ 20eV, (f): 50eV. (×) Present data, (◇) Sophia data.

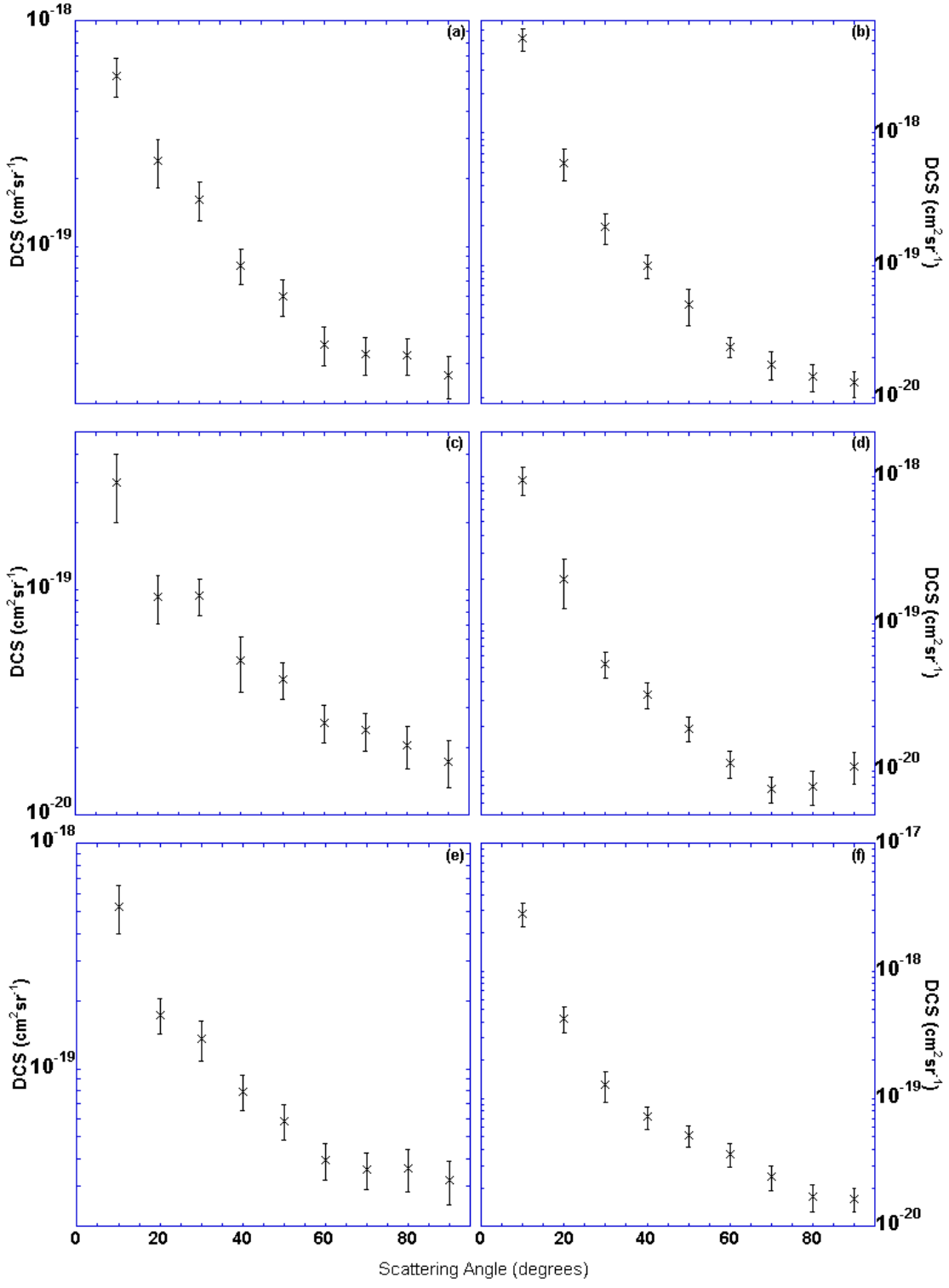

Figure A.4: DCSs (cm^2/sr), as a function of electron scattering angle (°), for various transitions and energies in H_2O (a): $1b_1 \rightarrow 3da_2$ $^3B_2$ + $^1B_2$ + $3a_1 \rightarrow 3pb_2$ $^3B_2$ 20eV, (b): 50eV, (c) : $1b_1 \rightarrow 3db_1$ $^3A_1$ + $^1A_1$ + $1b_1 \rightarrow 3da_1$ $^3B_1$ + $^1B_1$ + $1b_1 \rightarrow 4pb_2$ $^3A_2$ + $^1A_2$ 20eV, (b): 50eV, (e): $1b_1 \rightarrow 4pa_1$ $^3B_1$ + $^1B_1$ + $1b_1 \rightarrow 4pb_1$ $^3A_1$ + $^1A_1$ 20eV, (f): 50eV. (×) Present data.

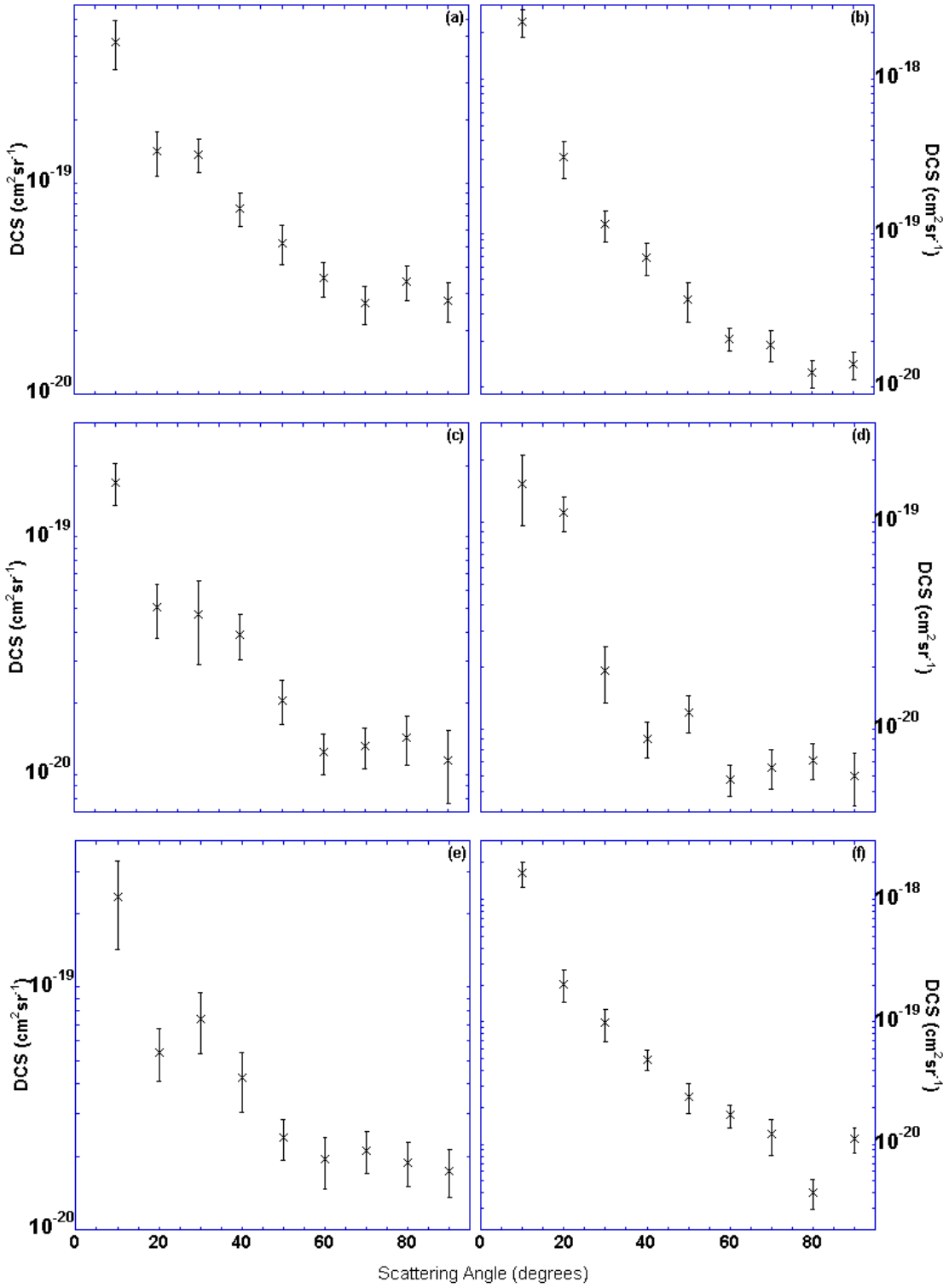

Figure A.5: DCSs (cm^2/sr), as a function of electron scattering angle (°), for various transitions and energies in H_2O (a): $1b_1 \rightarrow 3sa_1$ $^3B_2$ + $^1B_2$ + $3a_1 \rightarrow 3pb_2$ $^1B_2$ + $1b_1 \rightarrow 5sa_1$ $^3B_1$ + $^1B_1$ 20eV, (b): 50eV, (c): $1b_1 \rightarrow 4db_2$ $^3A_2$ + $^1A_2$ 20eV, (d): 50eV, (e): $1b_1 \rightarrow 4da_1$ $^3B_1$ 20eV, (f): 50eV. (×) Present data.

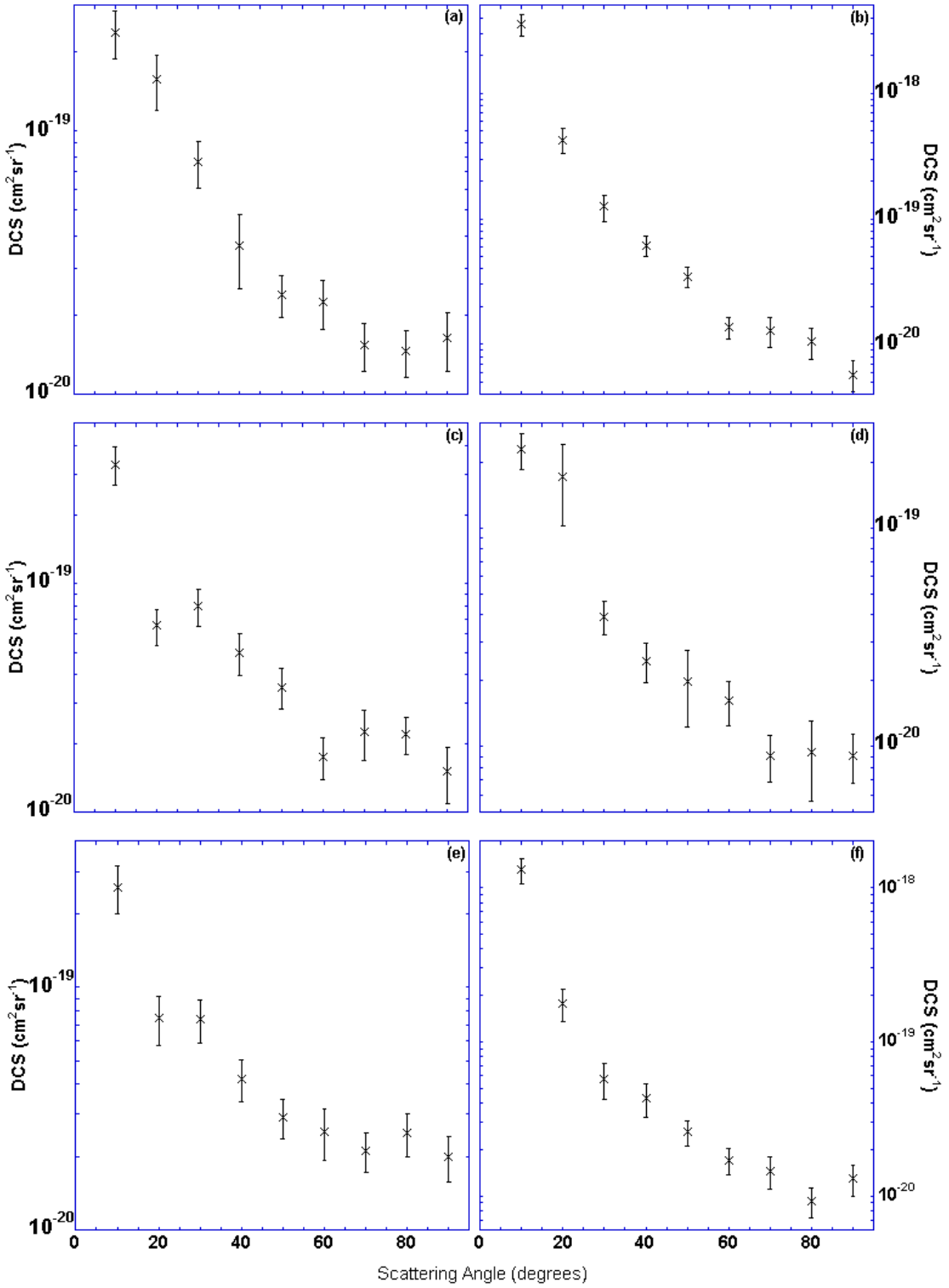

Figure A.6: DCSs (cm^2/sr), as a function of electron scattering angle (°), for various transitions and energies in H_2O (a): $1b_1 \rightarrow 4da_1$ $^1B_1$ 20eV, (b): 50eV, (c): $1b_1 \rightarrow 4db_1$ $^1A_1$ + $3a_1 \rightarrow 3pa_1$ $^3A_1$ 20eV, (d): 50eV, (e): $3a_1 \rightarrow 3pb_1$ $^3B_1$ + $1b_1 \rightarrow 5pa_1$ $^1B_1$ + $3a_1 \rightarrow 3pb_1$ $^1B_1$ + $1b_1 \rightarrow 5pb_1$ $^1A_1$ 20eV, (f): 50eV. (×) Present data.

$\tilde{d}^3A_1$					
Angle	15eV	20eV	30eV	40eV	50eV
10°	-	1.49 (0.57)	6.57 (2.88)	11.90 (2.12)	13.57 (3.32)
20°	0.21 (0.15)	-	2.29 (1.21)	2.54 (0.50)	2.19 (0.48)
30°	0.15 (0.07)	0.70 (0.15)	0.70 (0.14)	0.45 (0.08)	0.46 (0.08)
40°	0.16 (0.07)	0.60 (0.13)	1.03 (0.36)	0.33 (0.09)	0.29 (0.06)
50°	0.20 (0.06)	0.60 (0.11)	0.86 (0.18)	0.25 (0.06)	0.15 (0.06)
60°	0.19 (0.05)	0.49 (0.09)	0.34 (0.06)	0.17 (0.04)	0.10 (0.02)
70°	0.19 (0.05)	0.36 (0.07)	0.16 (0.05)	0.08 (0.02)	0.07 (0.01)
80°	0.11 (0.03)	0.27 (0.07)	0.13 (0.05)	0.09 (0.02)	0.07 (0.01)
90°	0.06 (0.01)	0.18 (0.04)	0.17 (0.06)	0.10 (0.03)	0.06 (0.02)
$\tilde{c}^3B_1 + \tilde{C}^1B_1$					
10°	1.43 (0.32)	9.13 (2.50)	29.18 (8.37)	53.62 (12.35)	54.22 (10.83)
20°	0.72 (0.23)	3.70 (0.77)	5.87 (1.33)	9.61 (1.90)	6.28 (1.72)
30°	0.34 (0.20)	1.94 (0.37)	2.00 (0.49)	1.74 (0.35)	1.35 (0.31)
40°	0.37 (0.07)	0.88 (0.17)	0.99 (0.23)	0.84 (0.22)	0.71 (0.16)
50°	0.28 (0.05)	0.67 (0.13)	0.88 (0.22)	0.55 (0.14)	0.42 (0.83)
60°	0.22 (0.05)	0.44 (0.08)	0.59 (0.11)	0.35 (0.17)	0.24 (0.04)
70°	0.27 (0.07)	0.37 (0.07)	0.42 (0.08)	0.36 (0.08)	0.19 (0.05)
80°	0.17 (0.04)	0.42 (0.09)	0.28 (0.08)	0.22 (0.05)	0.12 (0.03)
90°	0.10 (0.02)	0.32 (0.07)	0.29 (0.05)	0.27 (0.07)	0.12 (0.03)
$\tilde{D}^1A_1$					
10°	2.63 (0.53)	17.63 (3.96)	44.49 (23.00)	88.86 (19.19)	83.96 (16.35)
20°	1.25 (0.24)	7.87 (1.47)	10.42 (2.16)	13.93 (2.51)	8.50 (2.42)
30°	0.82 (0.37)	3.52 (0.65)	3.05 (0.63)	2.41 (0.45)	1.88 (0.39)
40°	0.80 (0.16)	1.70 (0.30)	1.82 (0.41)	1.50 (0.32)	1.57 (0.31)
50°	0.55 (0.10)	1.45 (0.26)	1.74 (0.30)	1.21 (0.21)	1.37 (0.27)
60°	0.47 (0.10)	0.98 (0.18)	1.31 (0.24)	1.24 (0.21)	0.95 (0.17)
70°	0.48 (0.10)	0.91 (0.17)	1.01 (0.25)	1.00 (0.22)	0.69 (0.15)
80°	0.35 (0.07)	0.90 (0.17)	0.67 (0.15)	0.70 (0.19)	0.43 (0.12)
90°	0.22 (0.06)	0.93 (0.20)	0.65 (0.12)	0.59 (0.12)	0.32 (0.06)

Table A.1: DCSs ($\times 10^{-19}$cm^2/sr) as a function of electron scattering angle (°). Values in brackets are the absolute error ($\times 10^{-19}$cm^2/sr).

$\tilde{C}^1B_1(100)+[3]^3B_1$					
Angle	15eV	20eV	30eV	40eV	50eV
10°	1.71 (0.95)	9.72 (2.52)	27.73 (9.27)	44.09 (8.95)	46.95 (9.90)
20°	0.65 (0.18)	4.06 (0.76)	5.91 (1.18)	8.99 (1.66)	5.62 (1.44)
30°	0.21 (0.20)	2.55 (0.48)	1.64 (0.61)	1.57 (0.29)	1.43 (0.36)
40°	0.45 (0.10)	1.19 (0.21)	1.17 (0.33)	0.86 (0.18)	0.78 (0.15)
50°	0.27 (0.07)	0.85 (0.16)	0.90 (0.16)	0.58 (0.10)	0.59 (0.14)
60°	0.25 (0.08)	0.53 (0.98)	0.67 (0.12)	0.60 (0.13)	0.37 (0.07)
70°	0.24 (0.06)	0.54 (0.10)	0.51 (0.11)	0.47 (0.10)	0.27 (0.06)
80°	0.16 (0.03)	0.55 (0.10)	0.37 (0.08)	0.33 (0.07)	0.19 (0.04)
90°	0.10 (0.03)	0.47 (0.11)	0.37 (0.07)	0.37 (0.07)	0.21 (0.04)
$[3]^1B_1$ + $[2]^1A_1(100)$					
10°		6.90 (1.59)	20.58 (5.90)	30.91 (6.29)	31.89 (6.50)
20°		2.65 (0.65)	4.10 (0.87)	6.34 (1.20)	4.18 (1.13)
30°		1.78 (0.39)	1.51 (0.32)	1.23 (0.23)	0.97 (0.21)
40°		0.99 (0.18)	0.88 (0.28)	0.65 (0.14)	0.66 (0.13)
50°		0.62 (0.11)	0.68 (0.12)	0.47 (0.08)	0.50 (0.10)
60°		0.42 (0.09)	0.52 (0.10)	0.48 (0.11)	0.30 (0.05)
70°		0.41 (0.08)	0.42 (0.09)	0.41 (0.09)	0.25 (0.06)
80°		0.41 (0.07)	0.38 (0.13)	0.26 (0.07)	0.14 (0.03)
90°		0.39 (0.09)	0.33 (0.08)	0.28 (0.06)	0.14 (0.03)
$[2]^3A_2$					
10°		2.70 (0.68)	5.79 (1.88)	9.55 (2.13)	8.37 (1.79)
20°		1.42 (0.26)	1.63 (0.33)	2.23 (0.45)	1.46 (0.34)
30°		0.90 (0.19)	0.52 (0.19)	0.65 (0.14)	0.52 (0.11)
40°		0.59 (0.11)	0.55 (0.24)	0.32 (0.08)	0.24 (0.04)
50°		0.40 (0.07)	0.31 (0.05)	0.19 (0.03)	0.15 (0.03)
60°		0.22 (0.04)	0.21 (0.04)	0.25 (0.15)	0.11 (0.07)
70°		0.21 (0.04)	0.20 (0.05)	0.16 (0.03)	0.27 (0.06)
80°		0.21 (0.04)	0.16 (0.04)	0.12 (0.04)	0.19 (0.04)
90°		0.21 (0.04)	0.19 (0.03)	0.16 (0.04)	0.21 (0.04)

Table A.2: DCSs ($\times 10^{-19}$cm^2/sr) as a function of electron scattering angle (°). Values in brackets are the absolute error ($\times 10^{-19}$cm^2/sr).

$[2]^1A_1(110) + [2]^1B_1(200)$				
Angle	20eV	30eV	40eV	50eV
10°	1.60 (0.32)	3.97 (1.28)	6.02 (1.41)	8.24 (1.64)
20°	0.36 (0.09)	0.81 (0.18)	1.56 (0.37)	0.86 (0.25)
30°	0.45 (0.11)	0.36 (0.07)	0.23 (0.04)	0.22 (0.05)
40°	0.10 (0.02)	0.17 (0.10)	0.12 (0.03)	0.15 (0.03)
50°	0.08 (0.04)	0.13 (0.03)	0.09 (0.04)	0.07 (0.02)
60°	0.08 (0.02)	0.10 (0.02)	0.12 (0.03)	0.02 (0.01)
70°	0.07 (0.02)	0.05 (0.01)	0.04 (0.01)	0.04 (0.01)
80°	0.06 (0.02)	0.04 (0.02)	0.05 (0.01)	0.04 (0.02)
90°	0.03 (0.01)	0.05 (0.01)	0.04 (0.01)	0.04 (0.01)
$[2]^1A_2$				
10°	2.67 (0.63)	4.20 (1.71)	4.76 (1.48)	4.07 (0.93)
20°	0.89 (0.19)	1.18 (0.25)	1.51 (0.27)	0.91 (0.18)
30°	0.69 (0.15)	0.56 (0.26)	0.53 (0.10)	0.36 (0.09)
40°	0.49 (0.10)	0.45 (0.13)	0.23 (0.05)	0.22 (0.06)
50°	0.34 (0.06)	0.28 (0.05)	0.17 (0.03)	0.12 (0.03)
60°	0.18 (0.04)	0.19 (0.03)	0.14 (0.04)	0.15 (0.03)
70°	0.19 (0.04)	0.17 (0.03)	0.15 (0.03)	0.08 (0.02)
80°	0.18 (0.04)	0.16 (0.03)	0.12 (0.02)	0.05 (0.01)
90°	0.18 (0.04)	0.18 (0.04)	0.15 (0.03)	0.08 (0.02)
$\tilde{e}^3B_1 + \tilde{E}^1B_1 + [2]^1A_1(200)$				
10°	6.19 (1.57)	22.51 (7.65)	41.09 (8.20)	46.19 (9.10)
20°	2.26 (0.46)	4.46 (0.93)	8.45 (1.53)	5.34 (1.47)
30°	1.57 (0.32)	1.77 (0.35)	1.82 (0.35)	1.77 (0.38)
40°	0.74 (0.13)	1.06 (0.27)	0.92 (0.19)	0.86 (0.18)
50°	0.65 (0.12)	0.76 (0.13)	0.51 (0.10)	0.46 (0.11)
60°	0.37 (0.07)	0.48 (0.09)	0.43 (0.09)	0.24 (0.04)
70°	0.33 (0.06)	0.34 (0.08)	0.28 (0.06)	0.18 (0.04)
80°	0.32 (0.06)	0.28 (0.09)	0.23 (0.05)	0.13 (0.04)
90°	0.28 (0.07)	0.23 (0.05)	0.22 (0.05)	0.16 (0.04)

Table A.3: DCSs ($\times 10^{-19}$cm^2/sr) as a function of electron scattering angle (°). Values in brackets are the absolute error ($\times 10^{-19}$cm^2/sr).

$[1,2]^3B_2 + {}^1B_2$				
Angle	20eV	30eV	40eV	50eV
10°	5.71 (1.14)	24.17 (8.53)	42.78 (8.20)	51.46 (10.13)
20°	2.41 (0.59)	4.97 (1.01)	8.96 (1.64)	5.95 (1.57)
30°	1.61 (0.31)	1.84 (0.37)	2.01 (0.37)	1.95 (0.50)
40°	0.82 (0.15)	1.11 (0.28)	1.02 (0.21)	0.99 (0.19)
50°	0.60 (0.11)	0.86 (0.16)	0.59 (0.11)	0.50 (0.15)
60°	0.37 (0.07)	0.53 (0.10)	0.42 (0.07)	0.24 (0.04)
70°	0.33 (0.06)	0.33 (0.07)	0.32 (0.07)	0.18 (0.04)
80°	0.33 (0.06)	0.27 (0.08)	0.22 (0.06)	0.14 (0.03)
90°	0.27 (0.06)	0.23 (0.04)	0.23 (0.05)	0.13 (0.03)
$[3]^3A_1 + [3]^3A_2 + [3]^1A_1 + [3]^1A_2 + [5]^3B_1 + [5]^1B_1$				
10°	3.00 (1.00)	7.21 (2.73)	9.79 (2.40)	9.54 (2.16)
20°	0.93 (0.22)	1.93 (0.41)	2.97 (0.54)	2.00 (0.74)
30°	0.94 (0.18)	0.74 (0.27)	0.75 (0.14)	0.53 (0.11)
40°	0.48 (0.13)	0.70 (0.25)	0.42 (0.08)	0.33 (0.07)
50°	0.40 (0.07)	0.42 (0.07)	0.24 (0.05)	0.19 (0.04)
60°	0.26 (0.05)	0.30 (0.06)	0.19 (0.03)	0.11 (0.02)
70°	0.24 (0.05)	0.20 (0.04)	0.16 (0.03)	0.08 (0.02)
80°	0.20 (0.04)	0.17 (0.04)	0.14 (0.03)	0.08 (0.02)
90°	0.17 (0.04)	0.17 (0.03)	0.17 (0.04)	0.11 (0.03)
$[6]^3B_1 + [6]^1B_1 + [4]^3A_1 + [4]^1A_1$				
10°	5.24 (1.27)	15.78 (5.00)	26.75 (6.71)	28.29 (5.84)
20°	1.74 (0.32)	3.16 (0.63)	5.86 (1.06)	4.27 (1.00)
30°	1.36 (0.27)	1.37 (0.28)	1.31 (0.24)	1.29 (0.35)
40°	0.80 (0.14)	0.92 (0.28)	0.71 (0.15)	0.72 (0.14)
50°	0.59 (0.11)	0.69 (0.13)	0.49 (0.09)	0.52 (0.10)
60°	0.39 (0.07)	0.50 (0.10)	0.47 (0.09)	0.37 (0.08)
70°	0.36 (0.67)	0.37 (0.07)	0.33 (0.07)	0.24 (0.05)
80°	0.36 (0.08)	0.25 (0.06)	0.25 (0.06)	0.17 (0.04)
90°	0.32 (0.07)	0.25 (0.05)	0.26 (0.05)	0.16 (0.03)

Table A.4: DCSs ($\times 10^{-19}$cm^2/sr) as a function of electron scattering angle (°). Values in brackets are the absolute error ($\times 10^{-19}$cm^2/sr).

$[2,3]^1B_2 + [3]^3B_2 + [7]^3B_1 + [7]^1B_1$				
Angle	20eV	30eV	40eV	50eV
10°	4.72 (1.25)	14.92 (5.90)	20.65 (4.19)	23.45 (4.83)
20°	1.42 (0.33)	3.58 (0.71)	6.16 (1.17)	3.10 (0.82)
30°	1.38 (0.26)	1.37 (0.56)	1.52 (0.28)	1.14 (0.25)
40°	0.76 (0.14)	1.18 (0.45)	0.85 (0.19)	0.69 (0.16)
50°	0.52 (0.11)	0.78 (0.13)	0.56 (0.10)	0.37 (0.11)
60°	0.36 (0.07)	0.57 (0.10)	0.45 (0.08)	0.21 (0.04)
70°	0.27 (0.06)	0.40 (0.10)	0.39 (0.08)	0.19 (0.04)
80°	0.34 (0.06)	0.33 (0.11)	0.29 (0.07)	0.12 (0.03)
90°	0.28 (0.06)	0.29 (0.06)	0.36 (0.07)	0.14 (0.03)
$[4]^3A_2 + [4]^1A_2$				
10°	1.70 (0.34)	1.41 (0.36)	0.58 (0.25)	1.54 (0.57)
20°	0.50 (0.13)	0.51 (0.15)	0.81 (0.45)	1.11 (0.21)
30°	0.47 (0.18)	0.78 (0.15)	0.32 (0.09)	0.19 (0.06)
40°	0.39 (0.08)	0.53 (0.37)	0.12 (0.04)	0.09 (0.02)
50°	0.21 (0.04)	0.15 (0.05)	0.07 (0.05)	0.12 (0.02)
60°	0.12 (0.02)	0.11 (0.05)	0.10 (0.04)	0.06 (0.01)
70°	0.13 (0.03)	0.14 (0.03)	0.08 (0.02)	0.07 (0.01)
80°	0.14 (0.03)	0.09 (0.03)	0.12 (0.02)	0.07 (0.01)
90°	0.12 (0.04)	0.10 (0.02)	0.15 (0.03)	0.06 (0.02)
$[8]^3B_1$				
10°	2.37 (0.94)	7.07 (3.70)	16.66 (3.36)	16.36 (3.74)
20°	0.54 (0.13)	1.83 (0.36)	2.72 (0.72)	2.04 (0.60)
30°	0.74 (0.21)	0.35 (0.09)	0.59 (0.14)	0.98 (0.29)
40°	0.42 (0.12)	0.24 (0.14)	0.36 (0.07)	0.50 (0.09)
50°	0.24 (0.05)	0.26 (0.05)	0.25 (0.07)	0.25 (0.07)
60°	0.19 (0.05)	0.17 (0.10)	0.17 (0.05)	0.17 (0.04)
70°	0.21 (0.04)	0.09 (0.05)	0.12 (0.03)	0.12 (0.04)
80°	0.19 (0.04)	0.18 (0.07)	0.08 (0.01)	0.04 (0.01)
90°	0.18 (0.04)	0.16 (0.04)	0.07 (0.02)	0.11 (0.03)

Table A.5: DCSs ($\times 10^{-19}$cm^2/sr) as a function of electron scattering angle (°). Values in brackets are the absolute error ($\times 10^{-19}$cm^2/sr).

$[8]^1B_1$				
Angle	20eV	30eV	40eV	50eV
10°	2.37 (0.48)	16.39 (6.35)	27.28 (6.48)	35.83 (6.98)
20°	1.58 (0.37)	2.78 (0.58)	7.18 (1.30)	4.26 (0.95)
30°	0.76 (0.16)	1.46 (0.30)	1.51 (0.29)	1.25 (0.29)
40°	0.37 (0.12)	0.78 (0.20)	0.79 (0.16)	0.62 (0.12)
50°	0.24 (0.04)	0.65 (0.13)	0.42 (0.08)	0.35 (0.06)
60°	0.22 (0.05)	0.45 (0.14)	0.33 (0.06)	0.14 (0.03)
70°	0.15 (0.03)	0.28 (0.06)	0.34 (0.09)	0.13 (0.03)
80°	0.15 (0.03)	0.16 (0.04)	0.17 (0.05)	0.11 (0.03)
90°	0.16 (0.04)	0.11 (0.02)	0.19 (0.04)	0.06 (0.02)
$[5]^3A_1$ + $[5]^1A_1$				
10°	3.31 (0.63)	2.84 (1.80)	1.92 (0.75)	2.28 (0.43)
20°	0.65 (0.12)	1.09 (0.31)	0.20 (0.05)	1.71 (0.69)
30°	0.79 (0.15)	0.44 (0.23)	0.19 (0.04)	0.39 (0.07)
40°	0.50 (0.10)	0.34 (0.08)	0.18 (0.05)	0.25 (0.05)
50°	0.35 (0.07)	0.17 (0.06)	0.12 (0.03)	0.20 (0.08)
60°	0.18 (0.04)	0.11 (0.09)	0.13 (0.02)	0.16 (0.04)
70°	0.22 (0.06)	0.10 (0.02)	0.07 (0.02)	0.09 (0.02)
80°	0.22 (0.04)	0.15 (0.04)	0.09 (0.02)	0.09 (0.04)
90°	0.15 (0.04)	0.16 (0.03)	0.13 (0.04)	0.09 (0.02)
$[6]^1A_1$ + $[9]^3B_1$ + $[9,10]^1B_1$				
10°	2.59 (0.58)	5.73 (2.89)	13.38 (2.96)	13.05 (2.48)
20°	0.75 (0.17)	1.32 (0.28)	2.85 (0.52)	1.78 (0.42)
30°	0.74 (0.15)	0.80 (0.24)	0.64 (0.14)	0.57 (0.15)
40°	0.42 (0.08)	0.47 (0.14)	0.47 (0.14)	0.43 (0.11)
50°	0.29 (0.05)	0.41 (0.07)	0.31 (0.06)	0.26 (0.05)
60°	0.25 (0.06)	0.28 (0.08)	0.24 (0.05)	0.17 (0.03)
70°	0.21 (0.04)	0.21 (0.09)	0.27 (0.08)	0.14 (0.03)
80°	0.25 (0.05)	0.14 (0.04)	0.19 (0.04)	0.09 (0.02)
90°	0.20 (0.04)	0.23 (0.08)	0.25 (0.12)	0.13 (0.03)

Table A.6: DCSs ($\times 10^{-19}$cm^2/sr) as a function of electron scattering angle (°). Values in brackets are the absolute error ($\times 10^{-19}$cm^2/sr).

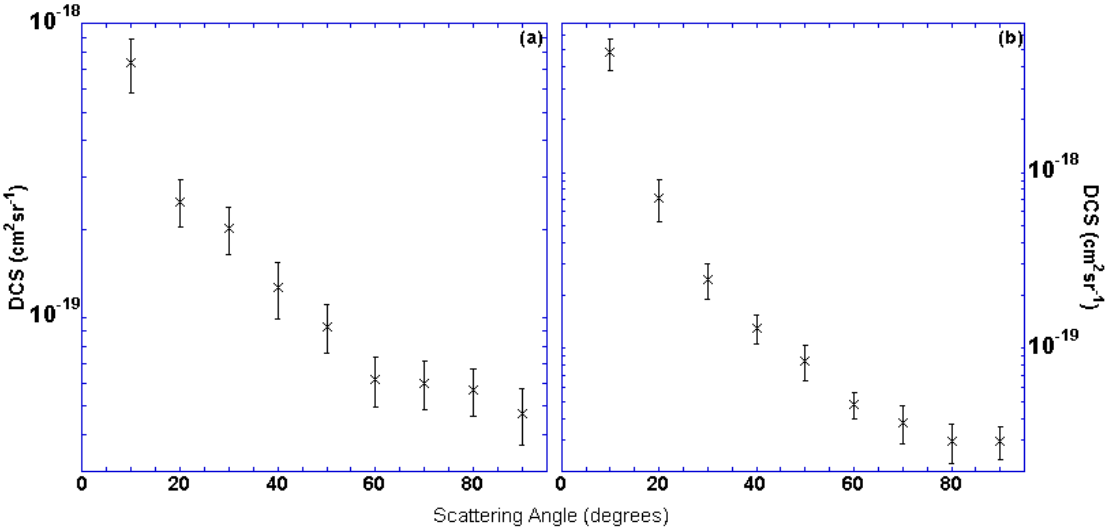

Figure A.7: DCSs (cm^2/sr), as a function of electron scattering angle (°), for the $3a_1 \rightarrow 3pa_1$ $^1A_1$ transition in H_2O at (a): 20eV and (b): 50eV. (×) Present data.

	$[7]^1A_1$			
Angle	20eV	30eV	40eV	50eV
10°	7.37 (1.53)	31.03 (14.17)	42.51 (9.51)	47.98 (9.70)
20°	2.48 (0.46)	6.51 (1.29)	12.46 (2.25)	7.17 (1.95)
30°	2.01 (0.37)	2.46 (1.02)	3.10 (0.58)	2.47 (0.57)
40°	1.27 (0.28)	2.11 (0.64)	1.36 (0.27)	1.30 (0.25)
50°	0.93 (0.18)	1.63 (0.29)	1.14 (0.20)	0.85 (0.20)
60°	0.61 (0.12)	1.10 (0.20)	0.92 (0.17)	0.48 (0.08)
70°	0.60 (0.11)	0.77 (0.17)	0.71 (0.17)	0.38 (0.09)
80°	0.57 (0.10)	0.64 (0.22)	0.38 (0.07)	0.30 (0.07)
90°	0.47 (0.10)	0.63 (0.12)	0.56 (0.14)	0.30 (0.06)

Table A.7: DCSs ($\times 10^{-19}$$cm^2$/sr) as a function of electron scattering angle (°). Values in brackets are the absolute error ($\times 10^{-19}$$cm^2$/sr).

Appendix B

Additional Integral Cross Section Plots and Table

ICSs for the remaining electronic-state transitions in water are plotted in figures B.1 to B.4 and tabulated in table B.1. There was no other data against which we could directly compare these results, thus limiting our discussion of them. Most of the ICS profiles followed a similar shape to those of the $\tilde{a}^3\mathrm{B}_1$, $\tilde{A}^1\mathrm{B}_1$, $\tilde{b}^3\mathrm{A}_1$, and $\tilde{B}^1\mathrm{A}_1$ cross sections discussed earlier. That is the general trend in the integral cross section profile was a rapid increase from threshold up to a plateau, thereafter slowly monotonically decreasing with increasing energy. None of our integral cross sections show any clear evidence for resonances, which is not unexpected given the size of the energy increments between each measurement.

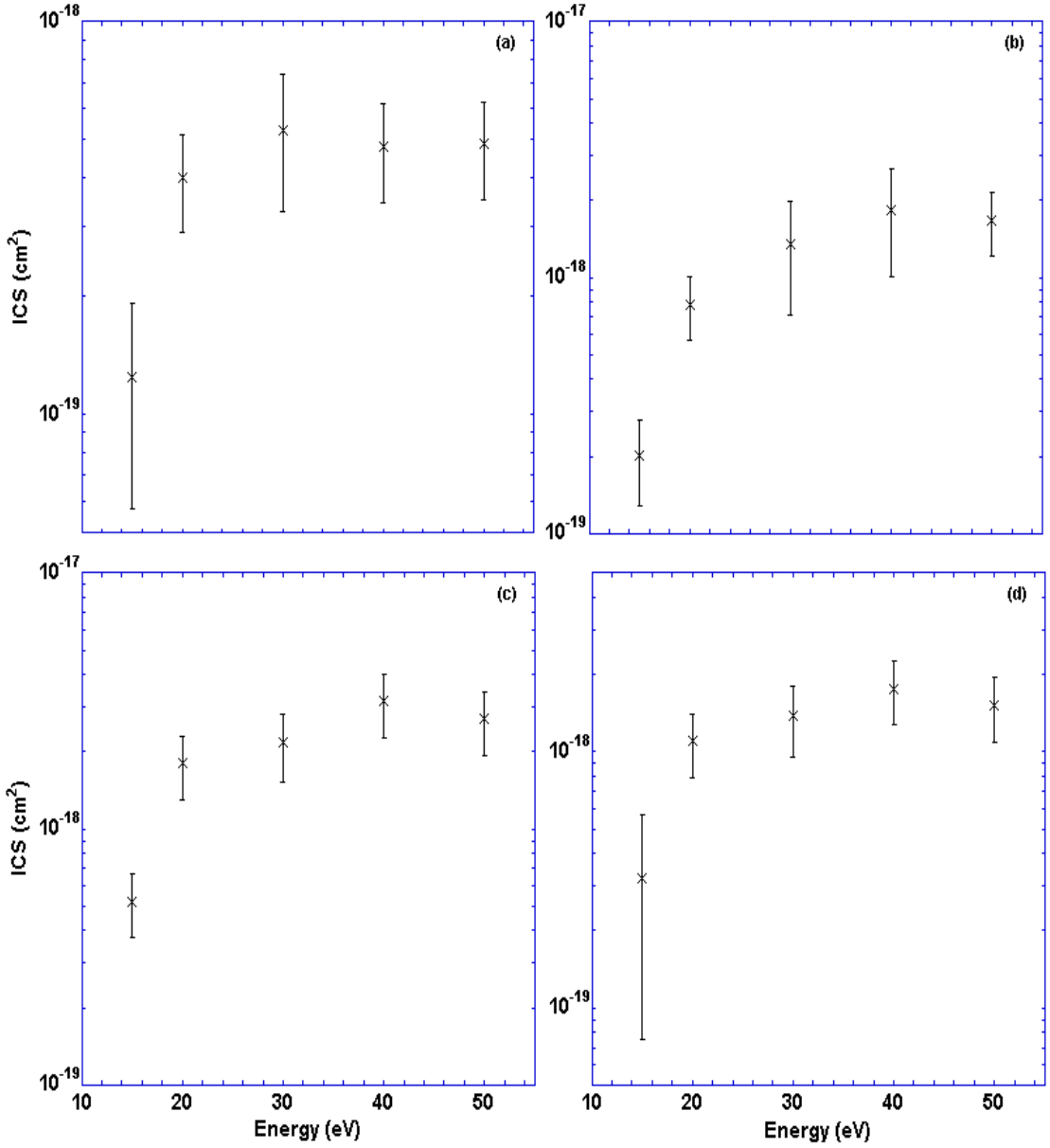

Figure B.1: Present ICSs (cm^2) of several further transitions in H_2O. (a): $1b_1 \rightarrow 3pb_1$ $\tilde{d}^3A_1$ (b): $1b_1 \rightarrow 3pa_1$ $\tilde{c}^3B_1$ + $\tilde{C}^1B_1$, (c): $1b_1 \rightarrow 3pb_1$ $\tilde{D}^1A_1$, (d): $1b_1 \rightarrow 3pa_1$ $\tilde{C}^1B_1(100)$ + $1b_1 \rightarrow 4sa_1$ $^3B_1$. (×) Present data

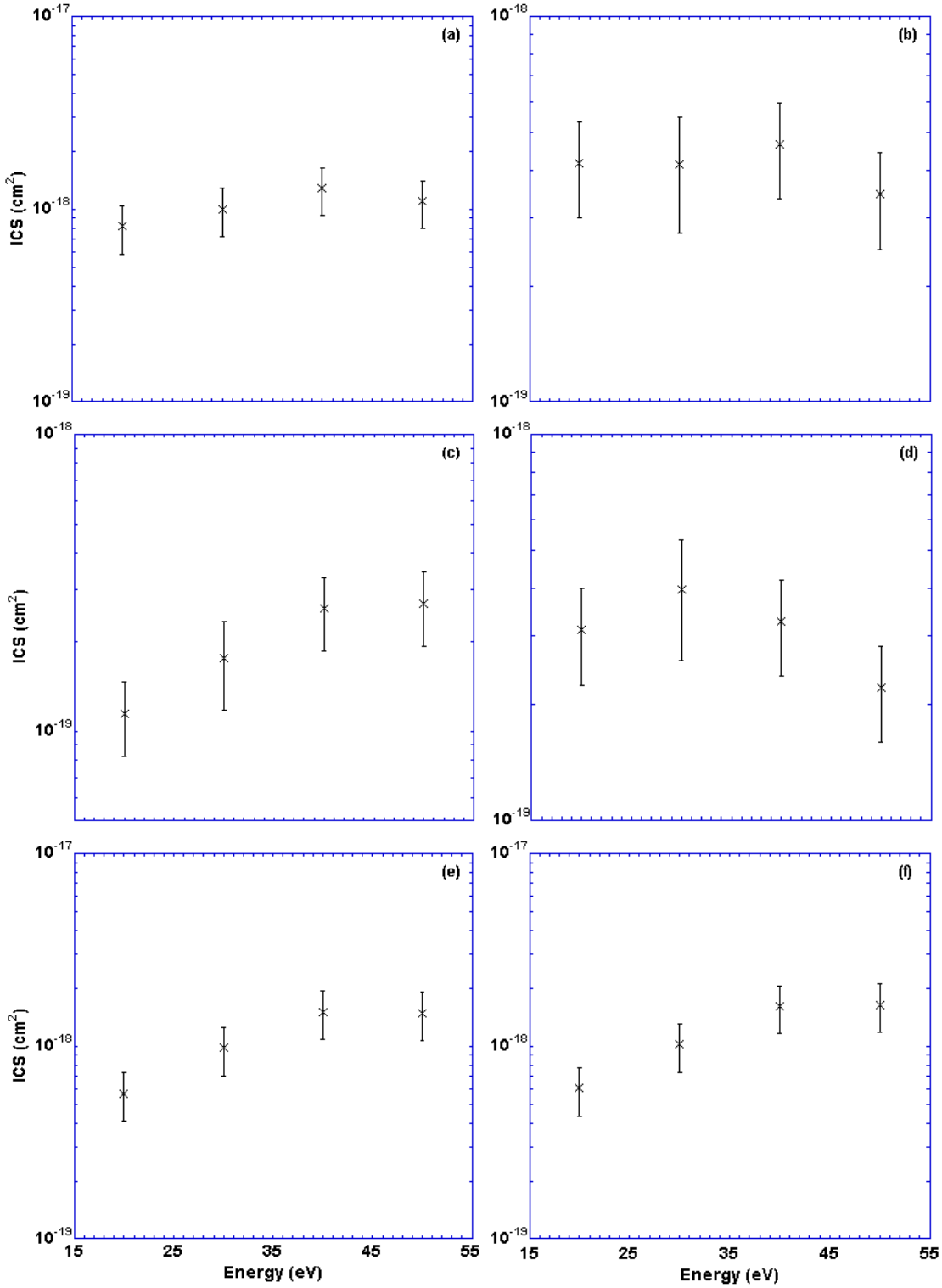

Figure B.2: Present ICSs (cm^2) of several further transitions in H_2O. (a): $1b_1 \rightarrow 4sa_1$ $^1B_1$ + $1b_1 \rightarrow 3pb_1$ $\tilde{D}^1A_1(100)$, (b): $1b_1 \rightarrow 3db_2$ $^3A_2$, (c): $1b_1 \rightarrow 3pb_1$ $\tilde{D}^1A_1(110)$ + $1b_1 \rightarrow 3pa_1$ $\tilde{C}^1B_1(200)$, (d): $1b_1 \rightarrow 3db_2$ $^1A_2$, (e): $1b_1 \rightarrow 3da_1$ $\tilde{e}^3B_1$ + $\tilde{E}^1A_1$ + $1b_1 \rightarrow 3pb_1$ $\tilde{D}^1A_1(200)$, (f): $3a_1 \rightarrow 3pb_2$ $^3B_2$ + $1b_1 \rightarrow 3da_2$ $^{3,1}B_2$. (×) Present data.

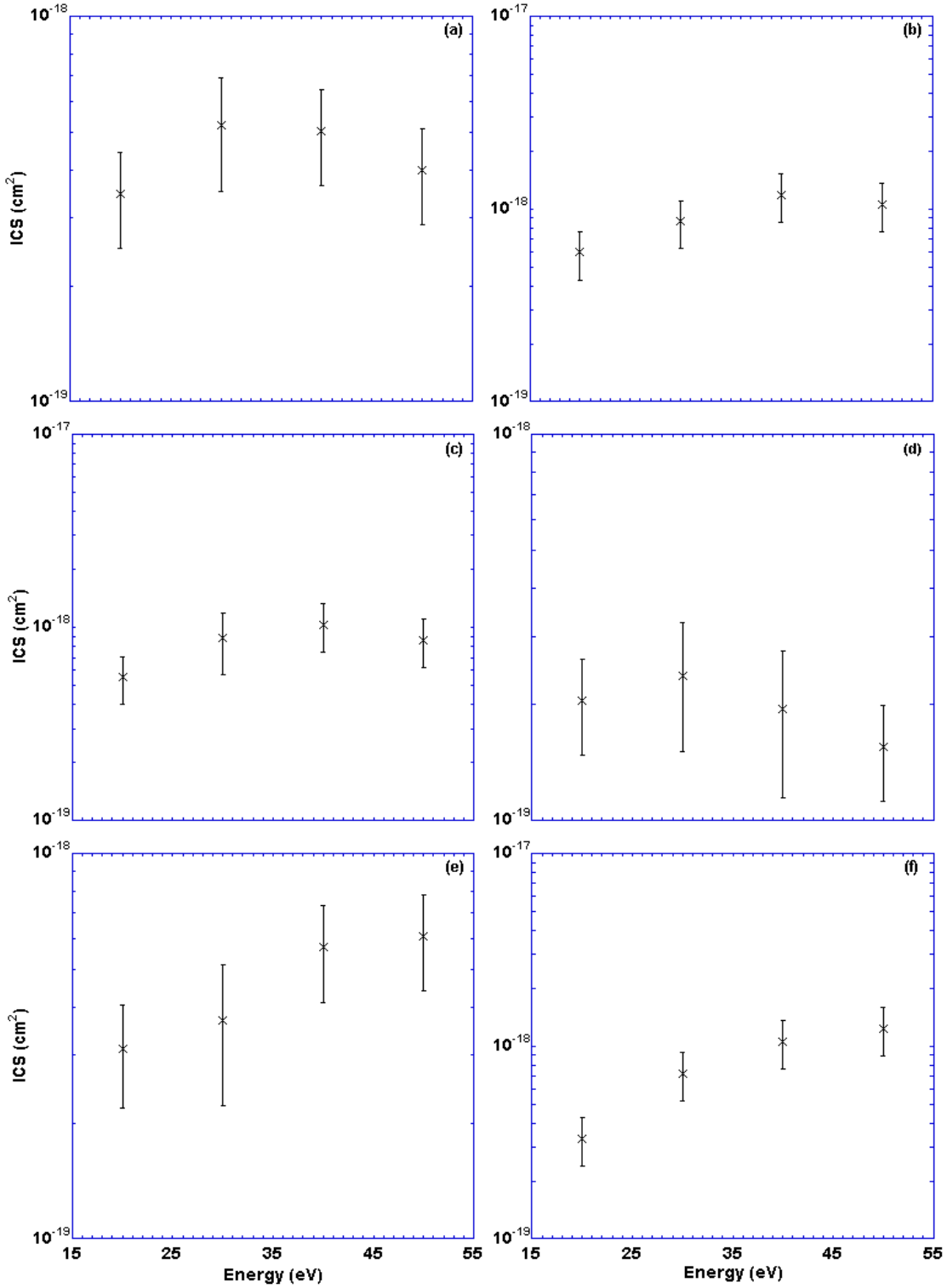

Figure B.3: Present ICSs (cm^2) of several further transitions in H_2O. (a): $1b_1 \rightarrow 3db_1$ $^{3,1}A_1$ + $1b_1 \rightarrow 3da_1$ $^{3,1}B_1$ + $1b_1 \rightarrow 4pb_2$ $^{3,1}A_2$, (b): $1b_1 \rightarrow 4pa_1$ $^{3,1}B_1$ + $1b_1 \rightarrow 4pb_1$ $^{3,1}A_1$, (c): $1b_1 \rightarrow 3sa_1$ $^{3,1}B_2$ + $3a_1 \rightarrow 3pb_2$ $^{1}B_2$ + $1b_1 \rightarrow 5sa_1$ $^{3,1}B_1$, (d): $1b_1 \rightarrow 4db_2$ $^{3,1}A_2$,(e): $1b_1 \rightarrow 4da_1$ $^{3}B_1$, (f): $1b_1 \rightarrow 4da_1$ $^{1}B_1$. (×) Present data.

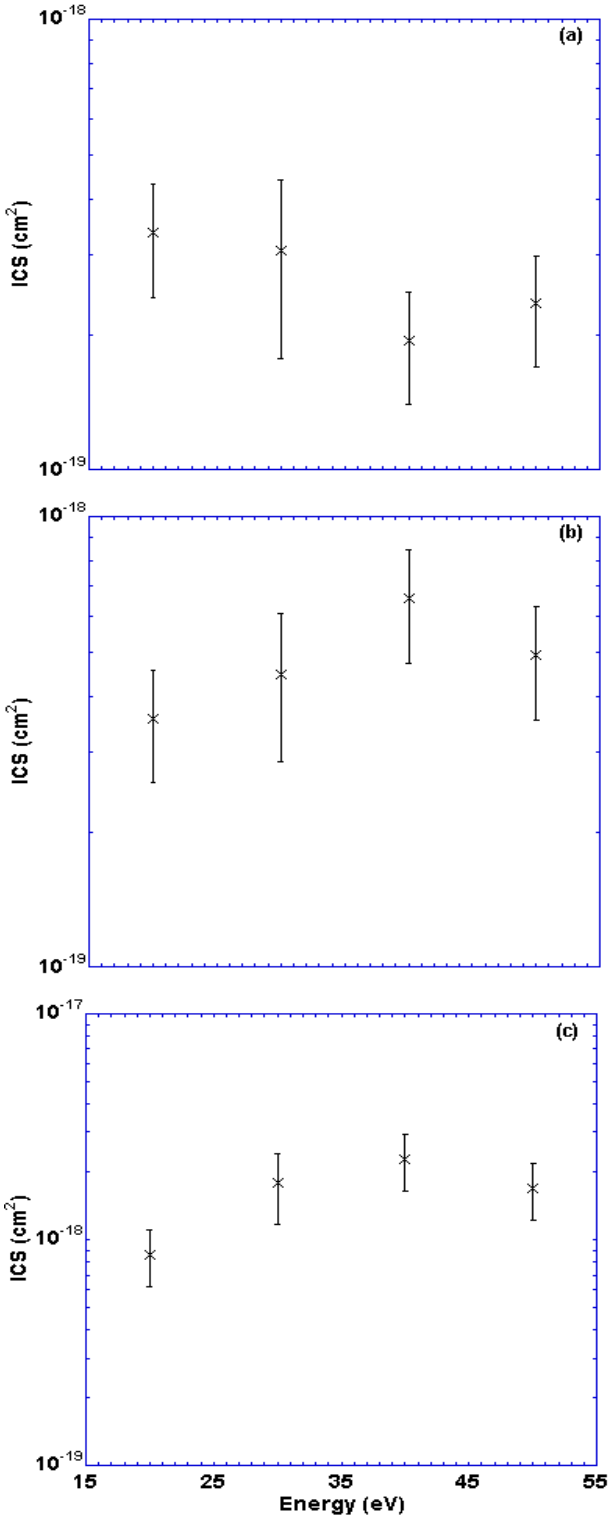

Figure B.4: Present ICSs (cm^2) of several further transitions in H_2O (a): $1b_1 \rightarrow 4db_1$ $^1A_1$ + $3a_1 \rightarrow 3pa_1$ $^3A_1$, (b): $3a_1 \rightarrow 3pb_1$ $^3B_1$ + $1b_1 \rightarrow 5pa_1$ $^1B_1$ + $3a_1 \rightarrow 3pb_1$ $^1B_1$ + $1b_1 \rightarrow 5pb_1$ $^1A_1$, (c): $3a_1 \rightarrow 3pa_1$ $^1A_1$. (×) Present data.

State	ICS ($\times 10^{-19}$ cm^2)				
	15eV	20eV	30eV	40eV	50eV
$\tilde{d}^3A_1[2]$	1.25 (0.67)	4.02 (1.12)	5.30 (2.03)	4.81 (1.35)	4.87 (1.36)
$\tilde{c}^3B_1[2]+\tilde{C}^1B_1[2]$	2.02 (0.74)	7.85 (2.20)	13.46 (6.37)	18.40 (8.32)	16.78 (4.70)
$\tilde{D}^1A_1[2]$	5.21 (1.46)	17.99 (5.04)	21.68 (6.38)	31.58 (8.84)	26.83 (7.51)
$^1B_1[2](100)+^3B_1[3]$	3.23 (2.48)	11.00 (3.08)	13.78 (4.18)	17.69 (4.95)	15.19 (4.25)
$^1B_1[3]+^1A_1[2](100)$		8.13 (2.28)	10.03 (2.81)	12.82 (3.59)	11.00 (3.08)
$^3A_2[2]$		4.16 (1.16)	4.12 (1.38)	4.65 (1.30)	3.45 (0.97)
$^1A_1[2](110)+^1B_1[2](200)$		1.14 (0.32)	1.77 (0.58)	2.59 (0.72)	2.69 (0.75)
$^1A_2[2]$		3.11 (0.87)	3.97 (1.38)	3.28 (0.92)	2.21 (0.62)
$\tilde{e}^3B_1[4]+\tilde{E}^1B_1[4]+^1A_1[2](200)$		5.67 (1.59)	9.76 (2.73)	15.12 (4.23)	14.87 (4.16)
$^3B_2+^1B_2+^3B_2[2]$		6.04 (1.69)	10.20 (2.86)	16.13 (4.52)	16.40 (4.56)
$^3A_1[3]+^1A_2[3]+^1A_1[3]+^3A_2[3]+^1B_1[5]+^3B_1[5]$		3.47 (0.97)	5.22 (1.72)	5.04 (1.41)	4.00 (1.12)
$^1B_1[6]+^3B_1[6]+^3A_1[4]+^1A_1[4]$		5.96 (1.67)	8.62 (2.41)	11.86 (3.32)	10.58 (2.96)
$^1B_2[2,3]+^3B_2[3]+^3B_1[7]+^1B_1[7]$		5.53 (1.55)	8.80 (3.06)	10.38 (2.91)	8.64 (2.42)
$^3A_2[4]+^1A_2[4]$		2.05 (0.57)	2.38 (0.87)	1.95 (0.80)	1.56 (0.44)
$^3B_1[8]$		3.12 (0.93)	3.68 (1.47)	5.71 (1.60)	6.10 (1.71)
$^1B_1[8]$		3.32 (0.93)	7.23 (2.02)	10.56 (2.96)	12.39 (3.47)
$^3A_1[5]+^1A_1[5]$		3.36 (0.94)	3.08 (1.32)	1.93 (0.54)	2.34 (0.65)
$^1A_1[6]+^3B_1[9]+^1B_1[9,10]$		3.57 (1.00)	4.48 (1.61)	6.59 (1.85)	4.92 (1.38)
$^1A_1[7]$		8.59 (2.41)	18.00 (6.23)	22.82 (6.39)	16.95 (4.75)

Table B.1: Absolute ICS values ($\times 10^{-19}$ cm^2) for the remaining excited electronic states of H_2O. Values in parentheses are the corresponding absolute uncertainties in the data ($\times 10^{-19}$ cm^2).

Bibliography

[1] Cernicharo, J. and Crovisier, J. *Space Science Reviews* **119**, 29 (2005).

[2] Sonnabend, G., Wirtz, D., Schieder, R., and Bernath, P. F. *Solar Physics* **233**, 205 (2006).

[3] Stalder, K. R. and Woloszko, J. *Contributions to Plasma Physics* **47**, 64 (2007).

[4] Taylor, F. W. *Reports on the Progress in Physics* **65**, 1 (2002).

[5] Tas, M. A., van Velduizen, E. M., and Rutgers, W. R. *Journal of Physics D: Applied Physics* **30**, 1636 (1997).

[6] Uehara, S., Nikjoo, H., and Goodhead, D. T. *Radiation Research* **152**, 202 (1999).

[7] Muñoz, A., Oller, J. C., Blanco, F., Gorfinkiel, J. D., Limão-Vieira, P., and García, G. *Physical Review A* **76**, 052707 (2007).

[8] Bray, I., Fursa, D. V., Kheifets, A. S., and Stelbovics, A. T. *Journal of Physics B: Atomic, Molecular and Optical Physics* **35**, R117 (2002).

[9] Buckman, S. J. and Sullivan, J. P. *Nuclear Instruments and Methods in Physics Research B* **247**, 5 (2006).

[10] Dyke, T. R. and Muenter, J. S. *The Journal of Chemical Physics* **59**, 3125 (1973).

[11] Karwasz, G. P., Brusa, R. S., and Zecca, A. *Rivista Del Nuovo Cimento* **24**, 1 (2001).

[12] Itikawa, Y. and Mason, N. J. *Journal of Physical and Chemical Reference Data* **34**, 1 (2005).

[13] Cartwright, D. C., Brunger, M. J., Campbell, L., Mojarrabi, B., and Teubner, P. J. O. *Journal of Geophysical Research* **105**, 20857 (2000).

[14] Campbell, L., Cartwright, D. C., Brunger, M. J., and Teubner, P. J. O. *Journal of Geophysical Research* **111**, A09317 (2006).

[15] Jones, D. B., Campbell, L., Bottema, M. J., Teubner, P. J. O., Cartwright, D. C., Newell, W. R., and Brunger, M. J. *Planetary and Space Science* **54**, 45 (2006).

[16] Meinel, A. B. *Astrophysical Journal* **111**, 555 (1950).

[17] Meinel, A. B. *Astrophysical Journal* **112**, 120 (1950).

[18] Trajmar, S., Williams, W., and Kuppermann, A. *The Journal of Chemical Physics* **58**, 2521 (1973).

[19] Goddard, W. A. and Hunt, W. J. *Chemical Physics Letters* **24**, 464 (1974).

[20] Chutjian, A., Hall, R. I., and Trajmar, S. *The Journal of Chemical Physics* **63**, 892 (1975).

[21] Jureta, J. J. *The European Physics Journal D* **32**, 319 (2005).

[22] Mota, R., Parafita, R., Giuliani, A., Hubin-Franskin, M.-J., Lourenco, J. M. C., Garcia, G., Hoffmann, S. V., Mason, N. J., Ribeiro, P. A., Raposo, M., and Limão-Vieira, P. *Chemical Physics Letters* **416**, 152 (2005).

[23] Cho, H., Park, Y. S., Tanaka, H., and Buckman, S. J. *Journal of Physics B: Atomic, Molecular and Optical Physics* **37**, 625 (2004).

[24] Faure, A., Gorfinkiel, J. D., and Tennyson, J. *Journal of Physics B: Atomic, Molecular and Optical Physics* **37**, 801 (2004).

[25] Varella, M. T. D. N., Bettega, M. H. F., Lima, M. A. P., and Ferreira, L. G. *The Journal of Chemical Physics* **111**, 6396 (1999).

[26] Okamoto, Y., Onda, K., and Itikawa, Y. *Journal of Physics B: Atomic, Molecular and Optical Physics* **26**, 745 (1993).

[27] Shyn, T. W. and Cho, S. Y. *Physical Review A* **36**, 5138 (1987).

[28] Johnstone, M. W. and Newell, W. R. *Journal of Physics B: Atomic, Molecular and Optical Physics* **24**, 3633 (1991).

[29] Danjo, A. and Nishimura, H. *Journal of the Physical Society of Japan* **54**, 1224 (1985).

[30] Hoshino, M., Kato, H., Makochekanwa, C., Buckman, S. J., Brunger, M. J., Cho, H., Kimura, M., Kato, D., Murakami, I., Kato, T., and Tanaka, H. NIFS - DATA - 101. Research Report in NIFS-Data Series (Toki, Japan, 2008).

[31] Pritchard, H. P., McKoy, B. V., and Lima, M. A. P. *Physical Review A* **41**, 546 (1990).

[32] Gil, T. J., Rescigno, T. N., McCurdy, C. W., and Lengsfield, B. H. *Physical Review A* **49**, 2642 (1994).

[33] Lee, M.-T., Michelin, S. E., Kroin, T., Machado, L. E., and Brescansin, L. M. *Journal of Physics B: Atomic, Molecular and Optical Physics* **28**, 1859 (1995).

[34] Morgan, L. A. *Journal of Physics B: Atomic, Molecular and Optical Physics* **31**, 5003 (1998).

[35] Gorfinkiel, J. D., Morgan, L. A., and Tennyson, J. *Journal of Physics B: Atomic, Molecular and Optical Physics* **35**, 543 (2002).

[36] Thorn, P. A., Brunger, M. J., Teubner, P. J. O., Diakomichalis, N., Maddern, T., Bolorizadeh, M. A., Newell, W. R., Kato, H., Hoshino, M., Tanaka, H., Cho, H., and Kim, Y.-K. *The Journal of Chemical Physics* **126**, 064306 (2007).

[37] Szmytkowski, C. *Chemical Physics Letters* **136**, 363 (1987).

[38] Harb, T., Kedzierski, W., and McConkey, J. W. *The Journal of Chemical Physics* **115**, 5507 (2001).

[39] Herzberg, G. *Electronic Spectra and Electronic Structure of Polyatomic Molecules*, volume 3 of *Molecular Spectra and Molecular Structure*. Krieger Publishing Company, Florida, 2nd edition, (1966).

[40] Diercksen, G. H. F., Kraemer, W. P., Rescigno, T. N., Bender, C. F., McKoy, B. V., Langhoff, S. R., and Langhoff, P. W. *The Journal of Chemical Physics* **76**, 1043 (1982).

[41] Claydon, C. R., Segal, G. A., and Taylor, H. S. *The Journal of Chemical Physics* **54**, 3799 (1971).

[42] Winter, N. W., Goddard, W. A., and Bobrowicz, F. W. *The Journal of Chemical Physics* **62**, 4325 (1975).

[43] Kaldor, U. *The Journal of Chemical Physics* **87**, 467 (1987).

[44] Warken, M. *The Journal of Chemical Physics* **103**, 5554 (1995).

[45] Christiansen, O., Koch, H., Jorgensen, P., and Olsen, J. *Chemical Physics Letters* **256**, 185 (1996).

[46] Larsen, H., Hald, K., Olsen, J., and Jorgensen, P. *The Journal of Chemical Physics* **115**, 3015 (2001).

[47] Cai, Z.-L., Tozer, D. J., and Reimers, J. R. *The Journal of Chemical Physics* **113**, 7084 (2000).

[48] Trofimov, A. B., Stelter, G., and Schirmer, J. *The Journal of Chemical Physics* **117**, 6402 (2002).

[49] Skerbele, A., Meyer, V. D., and Lassettre, E. N. *The Journal of Chemical Physics* **43**, 817 (1965).

[50] Knoop, F. W. E., Brongersma, H. H., and Oosterhoff, L. J. *Chemical Physics Letters* **13**, 20 (1972).

[51] Chan, W. F., Cooper, G., and Brion, C. E. *Chemical Physics* **178**, 387 (1993).

[52] Gurtler, P., Saile, V., and Koch, E. E. *Chemical Physics Letters* **51**, 386 (1977).

[53] Lassettre, E. N. and Francis, S. W. *The Journal of Chemical Physics* **40**, 1208 (1964).

[54] Skerbele, A. and Lassettre, E. N. *The Journal of Chemical Physics* **42**, 395 (1965).

[55] Lassettre, E. N., Skerbele, A., Dillon, M. A., and Ross, K. J. *The Journal of Chemical Physics* **48**, 5066 (1968).

[56] Skerbele, A., Dillon, M. A., and Lassettre, E. N. *The Journal of Chemical Physics* **49**, 5042 (1968).

[57] Compton, R. N., Huebner, R. H., Reinhardt, P. W., and Christophorou, L. G. *The Journal of Chemical Physics* **48**, 901 (1968).

[58] Johns, J. W. C. *Canadian Journal of Physics* **41**, 209 (1963).

[59] Price, W. C. *The Journal of Chemical Physics* **4**, 147 (1936).

[60] Bell, S. *Journal of Molecular Spectroscopy* **16**, 205 (1965).

[61] Watanabe, K. and Zelikoff, M. *Journal of the Optical Society of America* **43**, 753 (1953).

[62] Wilkinson, P. G. and Johnston, H. L. *The Journal of Chemical Physics* **18**, 190 (1950).

[63] Yeager, D., McKoy, B. V., and Segal, G. A. *The Journal of Chemical Physics* **61**, 755 (1974).

[64] Watanabe, K. and Jursa, A. S. *The Journal of Chemical Physics* **41**, 1650 (1964).

[65] van Harrevelt, R. and van Hemert, M. C. *The Journal of Chemical Physics* **112**, 5777 (2000).

[66] Nickel, J. C., Zetner, P. W., Shen, G., and Trajmar, S. *Journal of Physics E* **22**, 730 (1989).

[67] Campbell, L., Brunger, M. J., Nolan, A. M., Kelly, L. J., Wedding, A. B., Harrison, J., Teubner, P. J. O., Cartwright, D. C., and McLaughlin, B. *Journal of Physics B: Atomic, Molecular and Optical Physics* **34**, 1185 (2001).

[68] Brunger, M. J. and Teubner, P. J. O. *Physical Review A* **41**, 1413 (1990).

[69] Green, M. A. *Elastic and Inelastic Scattering from Oxygen and Carbon Dioxide.* PhD thesis, School of Chemistry, Physics and Earth Sciences, Flinders University, (2002).

[70] Thorn, P. A. *Electron Scattering from H_2O.* Honours thesis, School of Chemistry, Physics and Earth Sciences, Flinders University, (2003).

[71] Read, F. H., Comer, J., Imhof, R. E., Brunt, J. N. H., and Harting, E. *Journal of Electron Spectroscopy and Related Phenomena* **4**, 293 (1974).

[72] Brunt, J. N. H., Read, F. H., and King, G. C. *Journal of Physics E* **10**, 134 (1977).

[73] Mojarrabi, B. *Electron Scattering from Nitric Oxide.* PhD thesis, School of Chemistry, Physics and Earth Sciences, Flinders University, (1997).

[74] Brunger, M. J. *Electron Scattering From Atoms and Molecules.* PhD thesis, School of Chemistry, Physics and Earth Sciences, Flinders University, (1989).

[75] Pichou, F., Huetz, A., Joyer, G., Landau, M., and Mazeau, J. *Journal of Physics B: Atomic and Molecular Physics* **8**, L236 (1975).

[76] Allan, M. *Journal of Physics B: Atomic, Molecular and Optical Physics* **38**, 3655 (2005).

[77] Brunt, J. N. H., King, G. C., and Read, F. H. *Journal of Physics B: Atomic and Molecular Physics* **10**, 1289 (1977).

[78] Bevington, P. R. *Data Reduction and Error Analysis for the Physical Sciences.* McGraw-Hill, (1969).

[79] Lewis, B. R., England, J. P., Gibson, S. T., Brunger, M. J., and Allan, M. *Physical Review A* **63**, 022707 (2001).

[80] Rescigno, T. *Private Communication.* (2006).

[81] Chergui, M. and Schwenier, N. *Chemical Physics Letters* **219**, 237 (1994).

[82] Horsley, J. A. and Fink, W. H. *The Journal of Chemical Physics* **50**, 750 (1969).

[83] Wannier, G. H. *Physical Review* **90**, 817 (1953).

[84] Merz, R. and Linder, F. *Journal of Physics B: Atomic, Molecular and Optical Physics* **31**, 4663 (1998).

[85] Bottema, M. *Private Communication.* (2003).

[86] Baluja, K. L., Zhang, R., Franz, J., and Tennyson, J. *Journal of Physics B: Atomic, Molecular and Optical Physics* **40**, 3515 (2007).

[87] Kim, Y.-K. *Private Communication.* (2006).

[88] Trevisan, C. S. and Tennyson, J. *Journal of Physics B: Atomic, Molecular and Optical Physics* **34**, 2935 (2001).

[89] Khakoo, M. A. and Segura, J. *Journal of Physics B: Atomic, Molecular and Optical Physics* **27**, 2355 (1994).

[90] Kim, Y.-K. *The Journal of Chemical Physics* **126**, 064305 (2007).

[91] Kato, H., Kawahara, H., Hoshino, M., Tanaka, H., Brunger, M. J., and Kim, Y.-K. *The Journal of Chemical Physics* **126**, 064307 (2007).

[92] Mott, N. F. and Massey, H. S. W. *The Theory of Atomic Collisions*. Oxford University Press, third edition, (1965).

[93] Melton, C. E. *The Journal of Chemical Physics* **57**, 4218 (1972).

[94] Yousfi, M. and Benadbessadok, M. D. *Journal of Applied Physics* **80**, 6619 (1996).

[95] Straub, H. C., Lindsay, B. G., Smith, K. A., and Stebbings, R. F. *The Journal of Chemical Physics* **108**, 109 (1998).

[96] Roldan, A. M., Blanco, F., Garcia, G., Thorn, P., Brunger, M. J., Sullivan, J., and Buckman, S. J. In *Isolated Biomolecules and Biomolecular Interactions*, (2008).

[97] Jones, D. B., Campbell, L., Bottema, M. J., and Brunger, M. J. *New Journal of Physics* **5**, 114 (2003).

[98] Pavlov, A. V. *Annales Geophysicae* **16**, 176 (1998).

[99] *http://ccmc.gsfc.nasa.gov/modelweb/models/iri.html*.

[100] Lummerzheim, D. and Lilensten, J. *Annales Geophysicae* **12**, 1039 (1994).

[101] Feldman, P. D. and Doering, J. P. *Journal of Geophysical Research* **80**, 2808 (1975).

[102] Lummerzheim, D., Rees, M. H., and Anderson, H. R. *Planetary and Space Science* **37**, 109 (1989).

[103] *http://ccmc.gsfc.nasa.gov/modelweb/models/msis.html.*

[104] Gunson, M. R., Farmer, C. B., Norton, R. H., Zander, R., Rinsland, C. P., Shaw, J. H., and Gao, B.-C. *Journal of Geophysical Research* **95**, 13867 (1990).

[105] Edwards, D. P., Zaragoza, G., Riese, M., and López-Puertas, M. *Journal of Geophysical Research* **105**, 29003 (2000).

[106] Grossmann, K. U., Frings, W. G., Offermann, D., Andre, L., Kopp, E., and Krankowsky, D. *Journal of Atmospheric and Terrestrial Physics* **47**, 291 (1985).

[107] Arnold, F. and Krankowsky, D. *Nature* **268**, 218 (1977).

[108] Swider, W. and Narcisi, R. S. *Journal of Geophysical Research* **80**, 655 (1975).

[109] Solomon, S., Ferguson, E. E., Fahey, D. W., and Crutzen, P. J. *Planetary and Space Science* **30**, 1117 (1982).

[110] Körner, U. and Sonnemann, G. R. *Journal of Geophysical Research* **106**, 9639 (2001).

[111] Hartmann, G. K. *Physics and Chemistry of the Earth* **25**, 189 (2000).

[112] Ness, K., White, R., and Robson, P. In *The 15th Australian Gaseous Electronics Meeting*, (2008).

[113] Hasegawa, H., Date, H., and Shimozuma, M. *Journal of Physics D: Applied Physics* **40**, 2495 (2007).

[114] Cheung, B. and Elford, M. T. *Australian Journal of Physics* **43**, 755 (1990).